

NUCLEAR TRANSPARENCY AND SINGLE PARTICLE
SPECTRAL FUNCTIONS FROM QUASIELASTIC

$A(e, e'p)$ REACTIONS UP TO

$$Q^2 = 8.1 \text{ GeV}^2$$

BY

DAVID WAYNE McKEE, B.S.

A dissertation submitted to the Graduate School

in partial fulfillment of the requirements

for the degree

Doctor of Philosophy

Major subject: Physics

New Mexico State University

Las Cruces, New Mexico

May 2003

“Nuclear Transparency and Single Particle Spectral Functions from Quasielastic $A(e, e'p)$ Reactions up to $Q^2 = 8.1 \text{ GeV}^2$,” a dissertation prepared by David Wayne McKee in partial fulfillment of the requirements of the degree, Doctor of Philosophy, has been approved and accepted by the following:

Linda Lacey
Dean of the Graduate School

Stephen Pate
Chair of the Examining Committee

Date

Committee in charge:

Dr. Stephen F. Pate

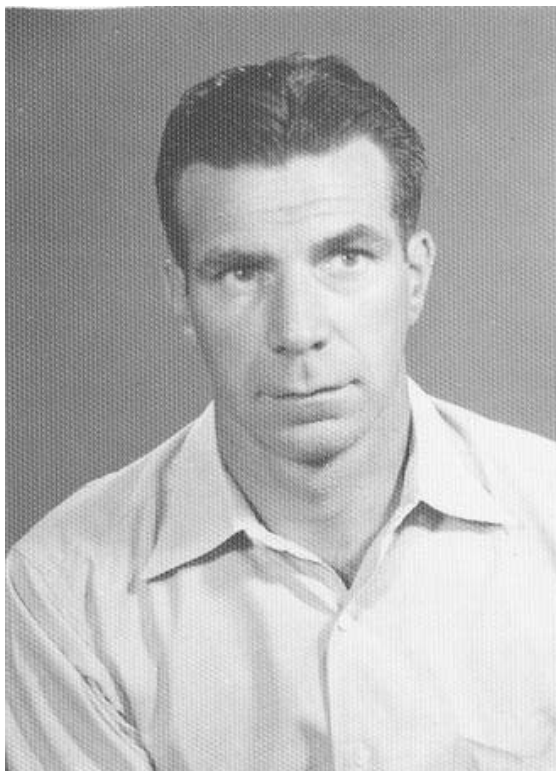
Dr. Gary S. Kyle

Dr. Heinz Nakotte

Dr. Igor Vasiliev

DEDICATION

Dedicated to the living memory of Wayne Clifford McKee (1911–1999), in the fondest hope that you would have been proud.



ACKNOWLEDGMENTS

It is not easy to write down in one place the names of all those who have made this work possible.

First and foremost, I acknowledge Melissa's patience and support. She hasn't complained about the long nights, about the weeks when, even if I come home, she only sees me bathed in the light of a monitor, or about stopping off in the middle of a date to check on my protons.

My parents have always been supportive of my intellectual ramblings, and uncertain plans for the future. They made college an easy experience because all I had to do was go to college, and didn't panic when I left college with no clear plan for the future. They provided the financial help to smooth over the rough spots in a poor graduate student's cash flow.

Melissa's parents provided considerable financial support, plenty of good advice, and took us on several much needed vacations. A little down-time does wonders for my productivity.

I have benefited from the knowledge, wisdom, and clarity of many students, physicists, and technicians here at Jefferson Lab, at New Mexico State University, and in the Hampton Roads area.

The whole NMSU nuclear physics group seems to have lent their skills to my cause at one time or another. George Burleson encouraged me to give nuclear physics a try, Gary Kyle offered me the chance to do so at Fermi Lab for a summer. Vassilli Papvassiliou and my advisor, Steve Pate, have guided me through the endless complexities of the subject. I don't know that I'll ever

have Bill Gibbs' deep understanding of computational methods, but the bits I've learned have helped in this work more than once already.

The NMSU Physics Department secretaries have been consistently helpful. Jan Bailey in particular has always looked out for the interests of the students, and repeatedly made my life easier.

The staff, postdocs and other graduate students with whom I've worked at Jefferson Lab have been endlessly helpful. I'm certain I'll forget somebody, and I promise that it is not by intention. Dave Mack provided days of patient guidance on physics, detectors, the lab computer systems, and how to make this program or that script actually work (and he sometimes describes graduate students as "the future doctor ... " which really helps, somehow). Steve Wood got me up and running in Linux. Jochen Volmer and Dave Gaskell were both thesis students on projects I apprenticed on while waiting for my own experiment to start. They gave me real work to do, trusted me to do it, helped in the rough spots, and used the results. It felt good, guys. John Arrington was, when I started here, the old man of Hall C grad students, and possesses an astoundingly complete understanding of the workings of the detectors, data acquisition, and software. His thesis is the closest thing I've seen to a manual for Hall C. Not to forget Elaine Schulte, Steve Avery, Joe Mitchell, Ketevi Assamagan, Hamlet Mkrtchyan, and Chris Armstrong.

The lab technical staff were always there. Whatever the problem, no matter how big, no matter how small, no matter what hour, Bill Vulcan, Paul Brindza, Steve Lassiter, Mike Fowler, and Joe Beaufait could make it better. They helped by phone when they should have been asleep, and if that didn't fix it, came in to make it right.

A special thanks to Dr. Dirk Walecka, who generously opened his class at William and Mary College to all comers from JLAB, and intervened with the university administration to get us parking permits and the like.

Dr. Khim Maung of Hampton University agreed to do the actual teaching for a field theory class that I was nominally taking at NMSU. A interesting, and pleasant opportunity to stretch my mind around some abstract ideas amidst the mundane work of data analysis.

My time at Jefferson Lab has been made that much easier by my regular workout with the Viet Vo Dao Club. Paul Gueye has given his time, knowledge, and instructional talents generously. To all the people who have studied with me: thank you. This means Mark, Kathy, Iaona, Sandy, Aamer, Surik, Lulin, and all the rest of you. Guy Ron has not only joined during his stays here, but lent us his knowledge as well. All of this is made possible by the space SURA has made available for us to hold our classes.

My salary during this extended and arduous process was paid from grant monies supplied by the Department of Energy. Your tax dollars at work, so thanks everyone.

This document was prepared in \LaTeX , mostly on the computer on my desk which belongs to NMSU and runs Linux. But one of the beauties of \LaTeX is its portability, and I have worked on this document on my old Apple Powerbook, and at least two PC laptops running Linux. Many thanks to Leslie Lamport, Donald E. Knuth, Linus Torvalds, Richard Stallman, and the un-named throngs of the Free Software/Open Source communities.



EDUCATION



- Dec. 1993 B.S. in Physics, University of California at Santa Barbara, Santa Barbara, CA.
- Jan. 1996–present Graduate Assistant, New Mexico State University, Las Cruces, NM.
- May–June 1998 Hampton University Graduate School at Thomas Jefferson National Accelerator, Newport News, VA.
- May–June 2000 CTEQ Summer School on QCD Analysis and Phenomenology, Lake Geneva, WI.

PUBLICATIONS

- D. Gaskell *et al.*, “Measurement of longitudinal and transverse cross sections in the He-3(e,e-prime pi +)3H reaction at W=1.6 GeV,” Phys. Rev. C **65**, 011001 (2002).
- D. Gaskell *et al.*, “Longitudinal Electroproduction Of Charged Pions From H-1, H-2, He-3,” Phys. Rev. Lett. **87**, 202301 (2001).
- E. C. Schulte *et al.*, “Measurement Of The High Energy Two-Body Deuteron Photodisintegration Differential Cross Section,” Phys. Rev. Lett. **87**, 102302 (2001).
- K. Garrow *et al.*, “Nuclear transparency from quasielastic A(e,e’p) reactions up to $Q^{*2} = 8.1-(\text{GeV}/c)^{*2}$,” Phys. Rev. C **66**, 044613 (2002).
- J. Volmer *et al.*, “New results for the charged pion electromagnetic form-factor,” Phys. Rev. Lett. **86**, 1713 (2001).

ABSTRACT

NUCLEAR TRANSPARENCY AND SINGLE PARTICLE
SPECTRAL FUNCTIONS FROM QUASIELASTIC

$A(e, e'p)$ REACTIONS UP TO

$$Q^2 = 8.1 \text{ GeV}^2$$

BY

DAVID WAYNE McKEE, B.S.

Doctor of Philosophy

New Mexico State University

Las Cruces, New Mexico, 2003

Dr. Stephen F. Pate, Chair

High statistics elastic and quasielastic scattering measurements were performed on hydrogen, deuterium, carbon, and iron at squared momentum transfers up to 8.1 GeV^2 . Both the nuclear transparency and the single particle spectral functions were extracted by means of comparison with a Plane-Wave Impulse Approximation calculation. Our data provide no evidence of the onset of color transparency within our kinematic range.

CONTENTS

LIST OF TABLES	xvii
LIST OF FIGURES	xix
1 INTRODUCTION AND THEORY	1
1.1 Basic Concepts	1
1.2 Motivation	4
1.2.1 Back-of-the-Envelope Calculation	5
1.2.1.1 Selection of a Small State	5
1.2.1.2 Fock State and the Natural Proton	5
1.2.1.3 Evolution to Natural State	6
1.2.1.4 Reduction of Final State Interactions	7
1.2.2 Theoretical Foundation	9
1.2.3 Why Here, Why This Way?	10
1.3 Kinematics	11
1.4 Nuclear and Color Transparency	14
1.4.1 Nuclear Transparency	14
1.4.2 Color Transparency	15

1.5	Existing Data	16
1.6	PWIA and Other Approximations	19
1.6.1	PWIA	19
1.6.2	DWIA	22
1.6.3	Glauber approximation	26
2	EXPERIMENTAL EQUIPMENT	29
2.1	Accelerator and Beam	29
2.2	Layout and Nomenclature of Hall C	31
2.3	Beamline Instrumentation	32
2.3.1	Beam Position Monitors	32
2.3.2	Superharp and the Beam Profile	33
2.3.3	Beam Current Monitors and Charge Measurement	33
2.3.4	Fast Raster	34
2.4	Targets	36
2.4.1	Scattering Chamber	37
2.4.2	Solid Targets	39
2.4.3	Cryo-targets	39
2.5	High Momentum Spectrometer	41
2.5.1	Geometry	41
2.5.2	Detector Stack	41
2.6	Short Orbit Spectrometer	46

2.6.1	Geometry	46
2.6.2	Detector Stack	48
2.7	Data Acquisition	48
2.7.1	Readout Electronics and Triggering	48
2.7.1.1	Hardware Trigger	50
2.7.1.2	Trigger Supervisor and 8LM	53
2.7.2	Retiming	56
2.7.3	DAQ	56
3	ANALYSIS ENGINE AND CORRECTIONS	57
3.1	Analysis Engine	57
3.1.1	Coordinate Systems and Naming Conventions	58
3.1.2	Algorithm	59
3.1.3	Controlling Replay	60
3.1.4	Kinematic Offsets	61
3.2	Trigger and Tracking Efficiencies	63
3.2.1	Trigger Efficiency	63
3.2.2	Tracking Efficiency	65
3.2.3	Error	67
3.3	Dead Time	67
3.3.1	Computer Dead Time	68
3.3.2	Electronic Dead Time	68

3.3.3	Dead Time Corrections	70
3.4	Particle Identification	70
3.5	Dependence of Cryo-target Density on Beam Current .	71
3.6	Proton Absorption	72
3.6.1	Basic Measurement	73
3.6.2	Previous Work	73
3.6.3	Issues and Definitions	73
3.6.3.1	What's in the Ntuples?	74
3.6.3.2	Prescales	74
3.6.3.3	Efficiencies	74
3.6.3.4	Definitions	75
3.6.4	Background	76
3.6.4.1	Dummy subtraction	76
3.6.4.2	Background Mismatch	77
3.6.4.3	Pure LH2	80
3.6.5	Theoretical Calculation	80
3.6.5.1	A Simple Model	81
3.6.5.2	What is λ ?	81
3.6.5.3	How Far to Go?	82
3.6.5.4	Results	82
3.6.6	Target Corrections	84

3.6.7	Momentum Dependence	86
4	MONTE CARLO	87
4.1	SIMC—The Hall C Monte Carlo	87
4.1.1	Summary	88
4.1.2	Running SIMC	89
4.2	Model Spectral Functions	90
4.2.1	Optical Model	90
4.2.2	Theory file	92
4.3	Radiative Corrections	93
4.3.1	Internal Bremsstrahlung and Vertex Corrections	97
4.3.2	External Bremsstrahlung	99
4.3.3	Monte Carlo Weight Generation	101
4.4	Other Features, Physics, and Corrections	102
4.4.1	Offshell Cross-section	102
4.4.2	Coulomb Correction	102
4.4.3	Spectrometer Models	103
4.4.4	Energy Loss and Multiple Scattering	104
4.4.5	Correlation Correction	104
4.5	SOS Extended Target Acceptance	105
5	PHYSICS ANALYSIS	106
5.1	Extraction of the Transparency	106

5.1.1	Analysis Cuts	106
5.1.2	Yield Corrections	108
5.2	Relationship Between the Cross-Sections	109
5.2.1	Physical Process	110
5.2.2	Finite Detectors	110
5.2.3	Finite Resolution and Averaging	111
5.2.4	Defining the Experimental Spectral Function	113
5.3	Extraction of the Spectral Function	114
5.3.1	Calculation of the Spectral Function	115
5.4	Deradiation of the Data	116
5.4.1	An Ideal Experiment	118
5.4.2	Mapping Out the Radiation and Other Effects	118
5.4.3	Sum Over Kinematics	121
5.5	Spectral Function Integration and Nuclear Transparencies From Spectral Functions	122
5.6	Error Analysis	125
5.6.1	Melted Target	125
5.6.2	Statistics	127
5.6.3	Systematic Errors	127
5.6.4	Model Dependence	128
6	RESULTS AND CONCLUSIONS	130

6.1	Transparency Results	130
6.1.1	A-Dependence	134
6.1.2	Q^2 -Dependence	134
6.2	Deradiated Spectral Functions	138
6.3	Future Work and Conclusions	145
A	SOLID TARGET THICKNESS	148
A.1	Equipment Used	148
A.2	Areal Densities	149
A.2.1	Area	150
A.2.2	Mass	151
A.2.3	Results	151
A.3	Error Analysis	153
A.4	Systematic Studies	154
A.4.1	Accuracy of Instruments	154
A.4.2	Point-to-point Variation	156
B	TOOL CHAINS AND CORRECT PROCEDURE	158
B.1	Where the Information Is	159
B.2	Tools	160
B.2.1	Doing the Work	160
B.2.2	Bookkeeping and Consistency	161
B.2.3	Procedure	162

B.3 Tests	164
BIBLIOGRAPHY	166

LIST OF TABLES

1.1	Summary of E94-139 kinematics.	14
2.1	Summary of the properties of the e94-139 targets.	37
2.2	Nominal specification for the Hall C spectrometers	44
2.3	8LM trigger logic	55
3.1	Summary of e94-139 kinematic offsets.	62
3.2	Average hodoscope plane efficiencies.	64
3.3	Summary of cryo-target density dependence measurements taken during the experimental run.	72
3.4	(Effective) Thickness of materials in HMS through the rear ho- doscopes.	83
3.5	Individual target proton absorption corrections.	84
5.1	Analysis cuts.	107
5.2	Correction applied to raw data and Monte Carlo yields.	108
5.3	Actual number of good events taken.	128
6.1	Measured nuclear transparencies for D, C, and Fe.	131
6.2	Results of the fits to the A-dependence.	131
6.3	Statistical comparisons of $^{12}\text{C}(\text{e},\text{e}'\text{p})$ data with various model cal- culations.	135

A.1	Positions of the corners of each target.	151
A.2	Measured areal densities of solid targets.	152
A.3	Comparison of measured solid target densities with standard values.	152
A.4	Comparison of nominal weight values with measurements by the analytical balance.	155
A.5	Point-to-point thickness variation of solid targets.	156

LIST OF FIGURES

1.1	Feynmann diagrams for elastic and quasi-elastic scattering. . . .	3
1.2	Reaction and kinematic quantities of the quasi-elastic scattering studied in e94-139.	12
1.3	Scattering angles in e94-139.	12
1.4	A typical missing energy spectrum for carbon collected during e94- 139.	17
1.5	Previous CT data for carbon.	18
1.6	Conceptual diagram for the Distorted Wave Impulse Approxima- tion.	23
2.1	Overhead schematic of CEBAF.	30
2.2	Overhead schematic of Hall C and the Hall C beamline, indicating the position of beamline instrumentation.	31
2.3	A histogram showing the distribution of the beam due to the fast raster in square (or bedpost) mode.	35
2.4	Sketch of the solid target ladder.	38
2.5	Sketch of the cryo-target ladder.	40
2.6	Sketch of the overall geometry of the HMS.	42
2.7	Exploded view of the HMS detector stack.	43
2.8	Particle velocity (β) spectrum in the HMS.	45

2.9	Sketch of the overall geometry of the SOS.	47
2.10	Exploded view of the SOS detector stack.	49
2.11	Schematic of the single arm trigger used in e94-139.	51
2.12	Schematic of the 8LM and trigger supervisor used in e94-139.	54
3.1	Comparison of the y'_{target} spectra between liquid hydrogen and the dummy target.	78
3.2	Direct comparison of invariant mass spectra between the LH2 and dummy targets.	78
3.3	Residual invariant mass spectra after dummy subtraction.	79
3.4	Energy loss by massive particles in various materials.	85
4.1	An abbreviated view of the carbon theory file (c12.theory) used in this analysis.	93
4.2	A comparison between data and Monte Carlo.	94
4.3	Example of a diagram contributing to the external Bremsstrahlung cross-section.	95
4.4	Diagrams contributing to the internal Bremsstrahlung cross-section.	95
4.5	Diagrams for first order corrections to the hard scattering vertex.	96
5.1	The missing energy dependence of the raw spectral function extracted from our data on carbon at $Q^2 = 3.3 \text{ GeV}^2$	117
5.2	A comparison of $\frac{S_{bin}^{MC,norad}}{S_{bin}^{MC,rad}}$ with $\frac{N_{bin}^{MC,norad}}{N_{bin}^{MC,rad}}$ for ^{12}C at $Q^2 = 3.3 \text{ GeV}^2$	120
5.3	The missing energy dependence of the deradiated spectral function extracted from our data on carbon at $Q^2 = 3.3 \text{ GeV}^2$	124
5.4	A photograph of the melted iron target.	126

6.1	Experimental (e,e'p) coincidence yields and transparency as function of proton angle.	132
6.2	Nuclear Transparency as a function of A at $Q^2 = 3.3, 6.1$, and 8.1 (GeV/c) ²	133
6.3	Transparency for (e,e'p) quasielastic scattering from D, C, Fe, and Au.	136
6.4	Nuclear Transparency for ¹² C(e,e'p) quasielastic scattering. . . .	137
6.5	An example deradiated spectral function.	139
6.6	Deradiated carbon spectral function versus missing energy. . . .	140
6.7	Deradiated carbon spectral function versus missing momentum. . .	141
6.8	Deradiated iron spectral function versus missing energy.	143
6.9	Deradiated iron spectral function versus missing momentum. . . .	144
B.1	A comparison of the deradiated spectral function arising from Monte Carlo output with radiation enabled, with the (raw) spectral function extracted from Monte Carlo output with radiation disabled.	165

1. INTRODUCTION AND THEORY

This work concerns itself with experiment e94-139 [1, 2] carried out at the Continuous Electron Beam Accelerator Facility (CEBAF) located at Thomas Jefferson National Accelerator Facility (Jefferson Lab) in Newport News, Virginia. The experiment is a continuation of an earlier experiment (e91-013, chaired by Don Geesaman [3, 4]).

Both experiments studied the propagation of protons through nuclei as a means of understanding the strong nuclear interaction. In particular the experiments attempted to verify the existence of a phenomenon first proposed by Mueller and Brodsky in 1982: Color Transparency [5, 6].

1.1 Basic Concepts

The strong nuclear force is well described at nuclear energy scales by simple theories with hadrons as the relevant degrees of freedom, and only a few parameters. It manifests as an attractive force between nucleons with a range of a few femtometers (fm), and a repulsive hard core. These properties allow us to treat the nuclear interaction geometrically (i.e. as a contact interaction between hard spheres) in semi-classical models [7, 8].

At higher energy scales, however, an increasing number of corrections are needed until one must invoke the full power of QCD with quark-gluon degrees

of freedom to explain the observed behavior. The transition between these two behavioral regimes has the potential to teach us much about the nature of the strong force. Dr. J. D. Walecka writes:

Now it is self-evident that *the appropriate set of degrees of freedom depends on the distance scale at which we probe the system* [7].¹

Electrons interact with nuclei by the exchange of a (virtual) photon which couples to the charged currents in the nucleus. Some four-momentum, \mathbf{q} , is transferred from the electron to the nuclear target by this exchange. We define the squared momentum transfer as $Q^2 = -\mathbf{q}^2$ which is a positive quantity for space-like virtual photons (as in this experiment), and use this as the figure of merit in this work. High (compared to m_p^2)² Q^2 scattering is said to be “hard.”

In e94-139 we studied semi-exclusive, quasi-elastic scattering of a proton out of a nucleus. By this we mean that both the scattered electron and the ejected proton are detected, but the remnant nucleus is not (the semi-exclusive part), and that the electron interacts in elastic kinematics with a single proton from the nucleus *as though it were a free particle*³ (the quasi-elastic part), as depicted in Fig. 1.1. Ideally, the nucleus is a spectator to this reaction, and is modified only to the extent that it loses a proton. In fact, it may interact with the electron as it traverses the nucleus, or with the affected proton after the scattering. These interactions are called initial- and final-state interactions depending on when they occur relative the scattering.

Keeping in mind the importance of distance scales noted above, we ask how we can scatter a single nucleon out of the nucleus. We would need to probe

¹Emphasis in the original.

²The natural energy scale of nuclear interactions is the proton mass, $m_p = 0.938$ GeV.

³Conservation of energy and momentum must still be obeyed, so the proton’s Fermi momentum is still considered, and the scattered particle loses some energy to its binding.

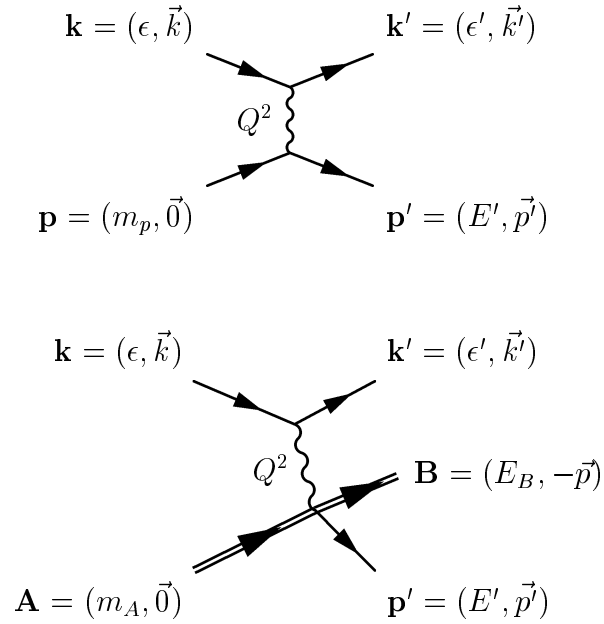


FIG. 1.1: Feynmann diagrams for elastic (top panel) and quasi-elastic (bottom panel) scattering.

a length scale below the size of the nucleus (a few fm) to interact incoherently with the nucleus, but not so much below the size of the nucleon (about a fm) that we cannot interact coherently with a proton. These distance scales are found at Q^2 s on order of .005 and .15 GeV^2 respectively.⁴ This has been done with great success, and provides a good picture of the nuclear shell structure [7].

So what happens if we go to harder scales than that? Generally, we excite the resonant states of the nucleons, eject pions and other mesons, and eventually reach the “Deep Inelastic Scattering” regime where the nucleon is being smashed to create a plethora of assorted hadrons [9]. But *sometimes*, we still scatter a

⁴Energy scales are inversely related to distance scales with the constant of proportionality $\hbar c = .197 \text{ GeV fm}$.

whole proton. This is an increasingly unusual event as we go up in Q^2 , but one with a distinctive experimental signature because it occurs in elastic kinematics.

We have:

$$Q^2 = 4\epsilon\epsilon' \sin^2\left(\frac{\Theta}{2}\right), \quad (1.1)$$

where ϵ , and ϵ' are the initial and final energies of the electron, and Θ is the angle through which it is scattered. Conservation of momentum also fixes the final direction and energy of the proton (to within the nuclear Fermi motion).

If the length scale is too small for nucleons to be the correct degrees of freedom, we may ask “How can we scatter a proton coherently?” One may speculate that this occurs by projecting out a small radius component of the proton wave function, and scattering this “small” proton. Further, since the strong interaction can be treated geometrically, we might be able to detect this effect by noticing a reduction in the final-state interaction between the nucleus and the scattered proton.

1.2 Motivation

The color transparency (CT) hypothesis is, roughly, that the cross-section for final state interactions (FSI) of quasi-elastically scattered nucleons is reduced as the momentum transfer increases. The mechanism suggested for the behavior is the selection of hadron states of small transverse size, which are assumed to be color neutral (not carrying any net strong charges) outside the small radius. This (optimistically named) “point-like configuration” propagates through the parent nucleus with much reduced cross-section for further interactions, and consequently, has a better chance of escaping the nucleus undisturbed.

1.2.1 Back-of-the-Envelope Calculation

We make a naive calculation assuming a proton is quasi-elastically scattered out of a nucleus by a virtual photon.⁵

1.2.1.1 Selection of a Small State

At momentum-transfers much larger than the hadron mass, the only scale available to us *is* the momentum-transfer, $Q = \sqrt{-q^2}$. We'll compute this model at Q^2 of 5 GeV² which is roughly in the middle of the range used in e94-139. This represents a spatial extent of $l = \frac{\hbar c}{Q} \approx .09$ fm, which is much smaller than the natural diameter of a proton (around 1 fm [7]).⁶

None-the-less, a proton can be scattered coherently by such a photon. It is not unreasonable to assume that such an event selects a state of the proton that is confined to a region of the characteristic size, l .

1.2.1.2 Fock State and the Natural Proton

We are interested in how a high momentum-transfer photon can interact with one parton, and scatter the entire proton coherently. To shed some light on the subject, we write the proton wave-function as a super-position of Fock states⁷, $|p\rangle = |qqq\rangle + |qqq\bar{q}\bar{q}\rangle + |qqqg\rangle + \dots$, and call the number of partons⁸ in

⁵This model bears no relationship that I'm aware of to the theoretical literature. Rather it consists of scale arguments applied to a "little billiard balls" picture of the scattering process. None-the-less, it seems to provide a meaningful cartoon of the process.

⁶The "size" of a proton depends on how it is measured. Nucleon-nucleon interaction have a hard-core of about .4-.5 fm radius, but the RMS radius proton charge distribution is approximately 1.5 fm.

⁷That is: states which are characterized by a fixed and definite number (and type) of particles. In the simplified notation used here, q represents a quark, \bar{q} an anti-quark, and g a gluon. A Fock state describing a proton must have three more quarks than anti-quarks, and may have zero or more gluons.

⁸Any constituent of the proton, i.e. a quark or gluon.

the state n . If the photon scatters a single parton, affecting the whole proton will require an additional $n - 1$ interactions each of momentum-transfer on order of Q .

Each interaction implies a factor of $\alpha^2 Q^{-4}$ in the cross-section for that particular channel,⁹ strongly suppressing the contribution of high-multiplicity Fock states. We are led to conclude that the low-multiplicity Fock states dominate the scattering cross-section. Both the low-parton multiplicity of the scattered state, and the scale of the additional exchanges suggest a small physical extent.

1.2.1.3 Evolution to Natural State

It is difficult to model how the “small” state will evolve back to a proton eigenstate, but relativity puts a lower limit on the time required. Initially, the probability density of the scattered proton is confined to a spatial region of the “small” size. The probability fluid cannot flow faster than the speed of light, so, we assume that the expansion proceeds at c . We get a minimum proper time¹⁰ for the evolution to be complete of $\tau = \frac{0.5*(1.0-0.09) \text{ fm}}{c} = 1.5 * 10^{-24} \text{ s}$. In this time the proton travels distance (in the rest frame of the nucleus) of $d = \gamma\tau\beta c$ (here γ is the relativistic time dilation parameters, and βc is the proton’s velocity). At $Q^2 = 5 \text{ GeV}^2$, quasi-elastic scattering fixes the proton energy at $E = \frac{Q^2}{2m_p} = 2.7 \text{ GeV}$ so we find $\beta = .94$ and $\gamma = 2.9$. Finally we get $d = 1.1 \text{ fm}$, or a substantial fraction of a nuclear radius. This suggests that the FSIs might, indeed, be suppressed at this scale.

⁹Each vertex in a scattering diagram contributes a factor of $\sqrt{\alpha}Q^{-1}$ to the matrix element for that channel. Here, α is the appropriate coupling constant. Each additional scattering means two new vertices, and the cross-section is proportional to the square of the matrix element.

¹⁰That is the time measured in the proton’s frame of reference.

1.2.1.4 Reduction of Final State Interactions

We can model the reduction of the cross-section for FSIs in a simplistic way by assuming that the nucleon-nucleon interaction is a collision between hard spheres. We write the radius of a “normal” nucleon as r_N , and the radius of the scattered proton at proper time τ as

$$r(\tau) = \begin{cases} \frac{\hbar c}{2Q} + c\tau & : \tau < \tau_{\text{crit}} = \frac{r_N}{c} - \frac{\hbar}{2Q} \\ r_N & : \tau \geq \tau_{\text{crit}} \end{cases}$$

If the nucleon must traverse the nucleus for length l to escape, its path defines a volume,¹¹

$$V(l) = \pi \int_0^l dl' (r_N + r(\frac{l'}{c\beta\gamma}))^2, \quad (1.2)$$

which must be clear of other nucleons if there are to be no FSIs. For some appropriately chosen “average” propagation length, \bar{l} , and nuclear volume,¹² V_A , the nuclear transparency is given by

$$T_A = 1 - (A - 1) \frac{V(\bar{l})}{V_A}, \quad (1.3)$$

where we have assumed that the nucleons are uniformly distributed in the nucleus (known to be false), that the ejected proton’s momentum is much higher than the Fermi momenta of the nucleons (quite a good approximation at our kinematics), and that $V(\bar{l}) \ll V_A$ which will be justified as we proceed.¹³

¹¹For a contact interaction, the size of both participating particles must be considered. This puts an unrealistic upper limit on the reduction of FSIs that is available in this model. Thanks to Dave Mack for input on this picture of the FSIs [10].

¹²We use the empirical function $R_A = (1.07 \text{ fm})A^{1/3}$ for the nuclear radius [7].

¹³This is roughly equivalent to saying that the mean free path for propagation through the nuclear medium is $l_{1/2}$ such that $V(l_{1/2}) = \frac{1}{2} \frac{V_A}{A-1}$

We need an estimate of \bar{l} . At low Q^2 (below the threshold for CT), $r(t) = r_N$, and we find

$$V_{low}(l) = 4\pi r_N^2 l. \quad (1.4)$$

Noting that for carbon at low Q^2 , $T \approx .6$ (see Fig. 1.5) we can work back from Eqs. (1.3) and (1.4) to find that the average propagation length in carbon is:

$$\begin{aligned} \bar{l}_C &= \frac{(1 - T_C) \frac{4}{3} \pi R_C^3}{4\pi r_N^2 (A_C - 1)} \\ &\approx \frac{(.4)(2.4 \text{ fm})^3}{33(.5 \text{ fm})^2} \\ &\approx .7 \text{ fm}, \end{aligned} \quad (1.5)$$

which is of the right order of magnitude.¹⁴

We can complete the integral in Eq. (1.2) to find

$$V_{CT}(l) = \begin{cases} \pi l \left[\left(r_N + \frac{\hbar c}{2Q} \right)^2 + \left(r_N + \frac{\hbar c}{2Q} \right) \frac{l}{\gamma\beta} + \frac{l^2}{3\gamma\beta} \right] & : l < l_{\text{crit}} = c\beta\gamma\tau_{\text{crit}} \\ V_{CT}(l_m) + 4\pi r_N^2 (l - l_m) & : l \geq l_{\text{crit}}. \end{cases} \quad (1.6)$$

Our value for \bar{l} is less than l_{crit} , so we calculate the transparency in carbon with our model:

$$\begin{aligned} T_C(5 \text{ GeV}^2) &= 1 - \frac{(A_C - 1)}{V_C} V_{CT}(Q^2 = 5 \text{ GeV}^2) \\ &= 1 - \frac{33(.7 \text{ fm})}{4(2.4 \text{ fm})^3} \left[(.545 \text{ fm})^2 + (.545 \text{ fm}) \frac{(.7 \text{ fm})}{2.7} + \frac{(.7 \text{ fm})^2}{19.3} \right] \\ &= 1 - .19 \\ &= .81, \end{aligned} \quad (1.7)$$

¹⁴An integral of the escape path over a uniform sphere comes to $\frac{3}{4}R_A$, or 1.8 fm for carbon, suggesting that this model is reasonable, but not as consistent as we might hope.

a very substantial increase in the nuclear transparency. While this model is very naive, it does suggest that the effect could be present. So this merits a closer look.

1.2.2 Theoretical Foundation

The simplest model of quasi-elastic knockout available is the first order Born approximation with plane-wave electron states (also known as the plane-wave impulse approximation) which will be discussed in detail later. By construction, it neglects the possibility of the final-state interactions (FSIs) that are responsible for nuclear transparencies less than unity (nuclear opacity?). More comprehensive models are needed if we are to have a baseline for understanding the experimental results.

The theoretical literature provides a rich selection of models to fill this need. Distorted Wave Impulse Approximation (DWIA) models add final state interaction to the proton through optical potentials, Coulomb corrections can be applied to the electron wave-functions, relativistic treatments of the proton have been done, and coupling of the electron to nuclear models more complicated than A valence nucleons can be added. A particularly interesting class of calculations is those that follow the prescription of Glauber [8]. These are done in the so-called “high-energy approximation” and have had some success modeling the existing data.

With a model of the final state interactions in hand, we introduce color transparency as a modification of the interaction cross-section of the ejected nucleon with the remnant nucleus [11, 12]. The need to introduce this modification

by hand is not a failing of the underlining theory (QCD), but a consequence of how the scattered proton is treated in these models.

1.2.3 Why Here, Why This Way?

The basic hypothesis of CT can be studied in a number of reactions. Both $A(e, e'p)$ and $A(p, 2p)$ experiments¹⁵ can probe the propagation of protons through the nuclear medium. $A(e, e'\rho)$ and other meson-production reactions investigate a similar problem. So what makes $A(e, e'p)$ a good reaction to use, and what makes Hall C a good facility to make the measurement?

The electron-nucleon interaction is weak, so electron scattering can probe the whole volume of the nucleus. Conversely, hadronic scattering tends to sample only the surface of the nucleus. (An incident proton is, after all, subject to the same strong interaction that we expect to weaken by scattering a “small” proton.) Further QED provides a precise understanding of the electron-photon vertex, allowing us to more easily extract a clean signal for color transparency.

The standard hardware and software in Hall C is well suited to making this measurement. Indeed e91-013 has already probed the region between Q^2 values of 0.6 and 3.3 GeV² and obtained substantially better error bars than the previously existing data set. The two magnetic spectrometers—called the High Momentum Spectrometer (HMS) and the Short Orbit Spectrometer (SOS)—provide high

¹⁵This notation provides a concise representation of a scattering experiment. Symbols appearing to the left of the comma are particles in the initial state, and symbols to the right are particles in the final state. The energy and momentum of particles represented inside the parenthesis *are* measured, while measurements are not made on particles appearing outside the parenthesis (though their momentum can sometimes be inferred, as in the case of nuclei in a fixed target). Unobserved particles in the final state are sometimes neglected in the notation.

resolution data over relatively large solid angles, allowing us to capture protons with initial momenta over most or all of the Fermi cone.¹⁶

Further the HMS can reach the high excitations and small lab-frame angles needed to obtain high Q^2 events with CEBAF's medium energy (several GeV) beam.

The high current, high duty-factor beam at CEBAF can provide a large enough integrated luminosity in reasonable time to overcome the rapidly falling cross-section for quasi-elastic scattering at high values of Q^2 leading to better statistics.

Hall C's event reduction software (called Replay) and Monte Carlo simulation (SIMC) have proven their ability to produce accurate physics results from the data collected in the hall.

All of these factors combine to allow Hall C to produce high precision data in a kinematic regime that has previously been explored only at low precision. Indeed the highest Q^2 value used exceeds the previous limits of CT data taking in the $A(e, e'p)$ system.

1.3 Kinematics

The reaction studied in e94-139 is the quasi-elastic knockout of a nuclear proton by an incident electron, $A(e, e'p)$. Figures 1.2 and 1.3 show the conventions we adopt for the kinematics of the reaction¹⁷. The incoming and outgoing electron four-vectors are represented by $\mathbf{k} = (\epsilon, \vec{k})$ and $\mathbf{k}' = (\epsilon', \vec{k}')$ respectively. Together they define the scattering plane. Scattering through a lab-frame angle

¹⁶The Fermi cone is the locus of tracks available to scattered protons for a fixed electron scattering angle and energy, and arises from the Fermi motion of protons inside the nucleus.

¹⁷Unless otherwise noted, all kinematic quantities are given in the lab-frame.

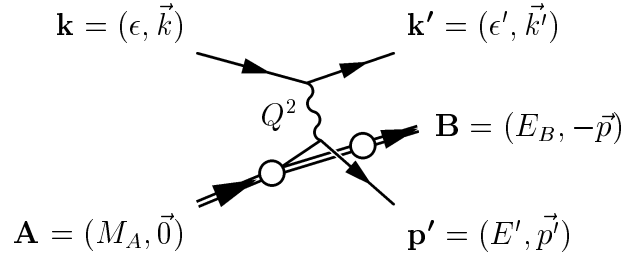


FIG. 1.2: Reaction and kinematic quantities of the quasi-elastic scattering studied in e94-139.

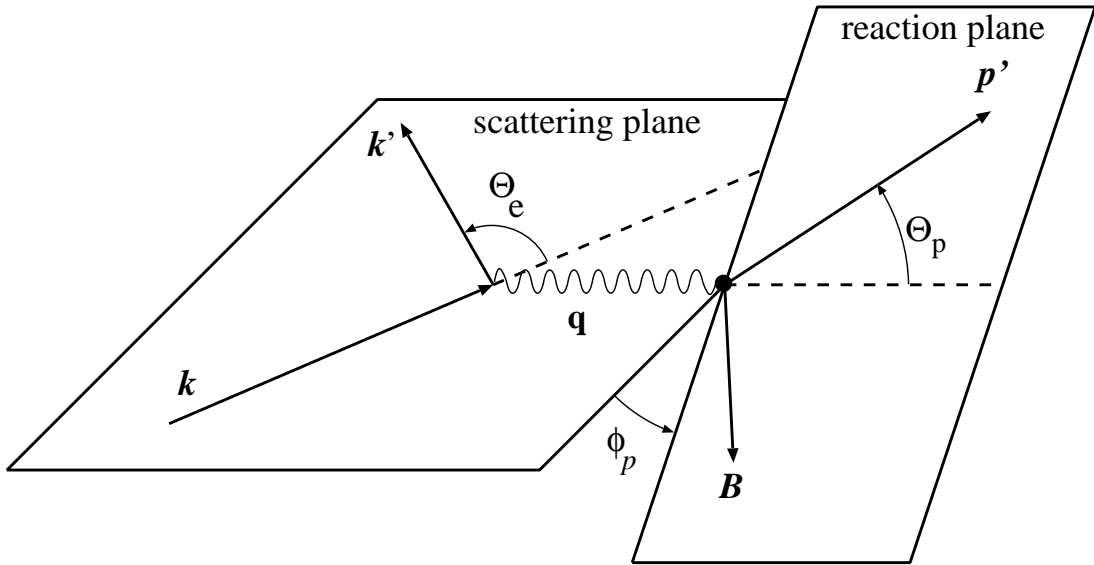


FIG. 1.3: Scattering angles in e94-139. (Figure based on the work of Jochen Volmer [13].)

of Θ_e the electron generates a single virtual photon (also in the scattering plane), with four-momentum $\mathbf{q} = \mathbf{k} - \mathbf{k}' = (\omega, \vec{q})$. The photon interacts with a bound proton carrying momentum $\mathbf{p} = (E, \vec{p})$, ejecting it from the target nucleus with momentum $\mathbf{p}' = (E', \vec{p}')$, and leaving the remnant nucleus (labeled B in Figs. 1.2 and 1.3) to recoil undetected, but carrying three-momentum $-\vec{p}$. The reaction plane is defined by the three-momenta of the virtual photon, and the scattered proton, and makes an angle ϕ_p with the scattering plane as shown in Fig. 1.3. We also define the “missing” energy and momentum:

$$\begin{aligned}
E_m &= (\epsilon - \epsilon') - E' + (E_A - E_{(A-1)}) \\
&= \omega - E' + (M_A - M_{(A-1)} - T_{(A-1)}) \\
&\approx \omega - E' + M_p - T_{(A-1)} \\
&= E_s
\end{aligned} \tag{1.8}$$

$$\begin{aligned}
\vec{p}_m &= \vec{p}' - (\vec{k} - \vec{k}') \\
&= \vec{p}' - \vec{q}.
\end{aligned} \tag{1.9}$$

The approximation made in Eq. (1.8) is that the remnant nucleus remains unexcited, at which point the missing energy can be equated with the separation energy of the struck nucleon, E_s .

Finally, we resolve the vector missing momentum \vec{p}_m into a scalar value p_m in the usual way, except that we also assign a positive (negative) sign for protons scattered farther from (closer to) the beam direction than the momentum transfer \vec{q} . That is, values of ϕ_p of $[-\pi/2, \pi/2]$ generate negative values of p_m .

Table 1.1 provides a summary of the kinematic settings used in e94-139. At the lowest Q^2 value, the proton spectrometer was swept through several angles

TABLE 1.1: Summary of E94-139 kinematics. Not all angles used for all targets. Bold face indicates quasi-elastic value for proton angle.

Q^2 (GeV ²)	Incident Energy (GeV)	Electron Angle (°)	Electron Arm Momentum (GeV)	Proton Angle (°)	Proton Arm Momentum (GeV)
3.3	3.06	54.00	1.30	19.78	2.52
				22.30	
				22.79	
				24.81	
				25.80	
				26.78	
				27.28	
				29.78	
6.1	4.47	64.65	1.20	15.33	4.09
8.1	5.56	64.65	1.27	12.84	5.15

to provide assurance that the whole Fermi cone had been mapped. This was not necessary at higher Q^2 because of the increased kinematic focusing.

1.4 Nuclear and Color Transparency

The goal of e94-139 is to study the variation of nuclear transparency, T , with Q^2 and nuclear mass number A , so it behooves us to define this quantity exactly.

1.4.1 Nuclear Transparency

Roughly, we wish to define the nuclear transparency as the fraction of quasi-elastically scattered protons to leave the nucleus without rescattering. In

practice, we require something to compare against. The elastic scattering of protons (1H) suggests itself, but this neglects off-shell effects on the electron-proton scattering cross-section. The choice made in most previous work [3, 4, 14, 15, 16] is to define the transparency as the ratio of the quasi-elastic cross-section to the plane-wave impulse approximation (PWIA) cross-section which we will define in Section 1.6.1. That is

$$T_A = \frac{\sigma_{\text{quasi-elastic}}}{\sigma_{\text{PWIA}}}. \quad (1.10)$$

1.4.2 Color Transparency

The crux of the Color Transparency hypothesis is that the nuclear transparency, T , should increase with increasing momentum transfer, Q . In the naive model, the size of the scattered, coherent proton state should be smaller, and its velocity higher, both of which improve the chances of escaping the nucleus without further interactions. More sophisticated semi-classical treatments also exhibit this behavior.

In a quantum mechanical treatment, the reduction of final state interactions may be seen as a consequence of Gribov’s inelastic scattering [11]. In this view, Color Transparency is a close parallel to the Chudakov effect in QED.

Nikolaev emphasizes that color transparency *must* be present if QCD is a gauge theory [11], but models of the scattered, “small” proton as a superposition of the proton and its resonances suggest that the onset of CT may be put back to very high Q^2 scales [11, 17, 18]. An interesting addendum is that Frankfurt et

al. suggest that the CT effect may be more pronounced in the s-shell than in the p-shell [19].

1.5 Existing Data

Exclusive quasi-elastic scattering builds on a long and glorious history of using inclusive electron scattering to probe the structure of the nucleus. The experimental history of $A(e, e'p)$ scattering goes back to experiments at Frascati in 1964 [20]. This and subsequent work “proved the literal truth of the shell model” [20]. Indeed the shell structure of light nuclei can be clearly seen with quite modest number of events, and only moderate missing energy resolution. Figure 1.4 shows the missing energy spectrum of carbon at $Q^2 = 3.3$ MeV in which the s- and p-shells are clearly visible.

These data provide a highly consistent picture of quasi-elastic processes at moderate Q^2 , and provide a foundation for understanding CT experiments [21].

The existing data on CT phenomena is quite substantial. Work at BNL, MIT-Bates, SLAC, FNAL, JLAB, and Hermes [3, 4, 14, 15, 16, 22, 23, 24, 25, 26, 27, 28] have studied $A(p, 2p)$, $A(e, e'p)$, $A(\mu, \mu\rho^0)$, $A(e, e'\rho^0)$, and $A(\pi, 2\text{jet})$ (“the diffractive dissociation into di-jets of 500 GeV pions”). These varied data present a complex picture which has required substantial theoretical effort to interpret.

One of the most striking features of the data is the contrast between the early onset of CT in systems where the scattered particle is a vector meson (typically a ρ^0), and the non-observation of CT in $A(e, e'p)$ to similar Q^2 [22, 24, 25]. Nemchik et al. argue that this is unavoidable: a result of the different wave functions of the initial ejectile state in the meson and baryon systems [18].

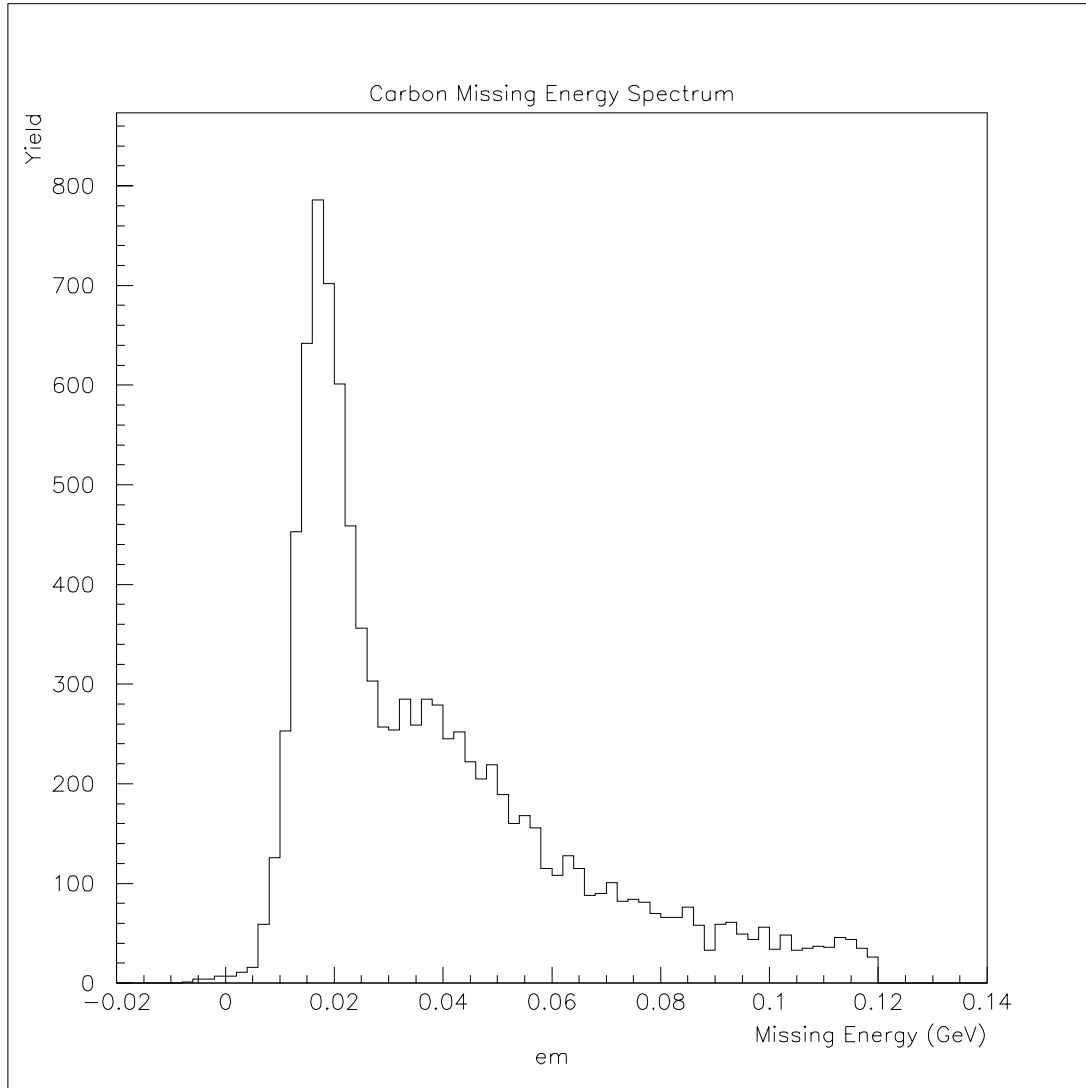


FIG. 1.4: A typical missing energy spectrum for carbon collected during e94-139. The sharp peak near .017 GeV is the p-shell, and the broader peak around .035 GeV is the s-shell.

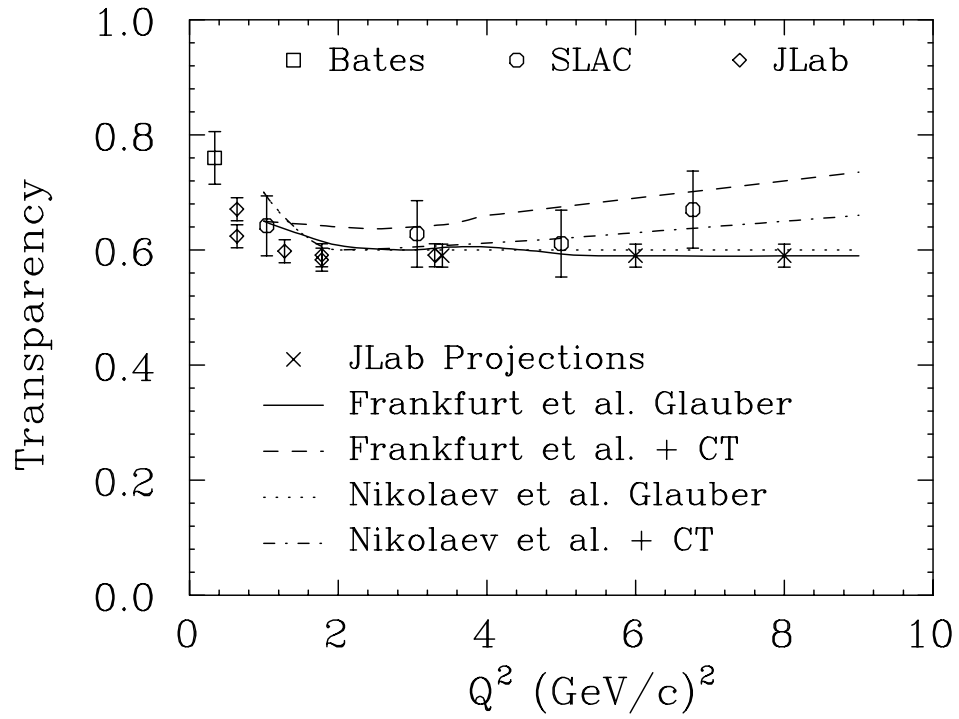


FIG. 1.5: Previous CT data for carbon. Several theoretical predictions and the projected errors for e94-139 are included [22, 23, 25, 29, 30].

Figure 1.5 shows the existing $^{12}C(e, e'p)$ data at the time of the e94-139 proposal, along with projections for the error bar to be obtained by this experiment. Also shown are some Glauber calculations by Frankfurt et al. and Nikolaev et al. with and without CT effects [29, 30].

1.6 PWIA and Other Approximations

A complete development of the theory of quasi-elastic electron scattering is far beyond the scope of this work. For a very complete treatment see Frullani and Mourgey [20]. A less comprehensive—but possibly more comprehensible—treatment is in the work of de Forest [31]. We will simply give some of the more important results, and discuss their consequences.

1.6.1 PWIA

In the Born approximation, the cross-section for unpolarized, elastic $(e, e'p)$ scattering is given by the Rosenbluth cross-section:

$$\frac{d\sigma}{d\Omega} = \left(\frac{d\sigma}{d\Omega} \right)_{\text{Mott}} \frac{Q^2}{|\vec{q}|^2} \left[G_E^2(Q^2) + \tau \epsilon^{-1} G_M^2(Q^2) \right], \quad (1.11)$$

where $\tau = \frac{|\vec{q}|^2}{Q^2} - 1$, and ϵ is the virtual photon polarization parameter, $\epsilon = \frac{1}{1+2(1+\tau)\tan^2(\frac{\theta}{2})}$. The Mott cross-section $\left(\frac{d\sigma}{d\Omega} \right)_{\text{Mott}}$ is the well known cross-section for scattering an electron from a point charge.

The form factors, G_E and G_M appearing in Eq. (1.11) contain all the information about the structure of the proton: the internal distribution of charges and currents. They are reasonably well represented by the dipole approximation:

$$G_E(Q^2) \approx \left(1 + \frac{Q^2}{0.71} \right)^{-2} \quad (1.12)$$

$$G_M(Q^2) \approx \mu G_E(Q^2). \quad (1.13)$$

A better parameterization is given by Bosted [32]¹⁸, and is used in the Hall C Monte Carlo. This is a full, first-order description (modulo the correct expressions for G_E , and G_M) of both inclusive and exclusive scattering, because the electron kinematics fix the proton kinematics.

Scattering from a nuclear target is more complicated. Not only do the protons have significantly non-zero momentum distributions, but they are off-shell, and their electro-magnetic current distributions cannot, a priori, be assumed to be the same as those of a free proton. Additionally, there can be initial- and final-state interaction due to the nucleus.¹⁹ All of these effects are dependent on the nucleon-nucleon interaction, and are not amenable to closed form calculation.

This makes for a complicated theoretical picture for which no complete solution is known. We make the following approximations:

- The primary reaction takes place by one photon exchange (the Born approximation).
- The reaction occurs quickly enough that the dynamics of the nucleus may be safely neglected (the Impulse approximation).
- Both the electron and the proton are adequately described by plane waves, and there are no hadronic final state interactions (the Plane Wave approximation).

¹⁸Earlier works seem to have used Gari and Krümpelmann, Z. Phys. A322 p689.

¹⁹ Another important change is the addition of a third final-state particle (the recoiling nuclear remnant), which increases the dimensionality of the phase space needed to describe the interaction from one (say the electron azimuthal angle) to five (the angles for both the electron and the proton and one energy). Note that because Hall C is not azimuthally symmetric, we actually use one more dimension to describe the orientation of the reaction relative the hall.

- The nucleon detected is the one the electron interacts with.

These assumptions comprise the Plane Wave Impulse Approximation (PWIA) [20], and are the basis for the Hall C Monte Carlo. If we also require, by extension from the second assumption, that the remnant nucleus is not excited by the interaction, and has mass $M_{A-1} = M_A - M_p$, we can equate the missing energy, E_m , with the separation energy of the ejected proton.

It is useful to do the quasi-elastic calculation first with only the first assumption (one-photon exchange). In this case the dependence on the nuclear structure and interaction can be grouped into a limited number of factors. We get [33]:

$$\begin{aligned} \frac{d^6\sigma}{d\epsilon d\Omega_{e'} dE' d\Omega_{p'}} &= p'E' \sigma_{\text{Mott}} \times \\ &\left(\frac{\lambda}{2} W_L(\mathbf{q}) + \tan^2\left(\frac{\Theta_e}{2}\right) W_T(\mathbf{q}) + \right. \\ &\lambda(\lambda + \tan^2\left(\frac{\Theta_e}{2}\right))^{1/2} W_{LT}(\mathbf{q}) \cos(\phi_p) + \\ &\left. \frac{\lambda}{2} W_{TT}(\mathbf{q}) \cos 2\phi_p \right), \end{aligned} \quad (1.14)$$

where $\lambda = \frac{Q^2}{|q|^2}$. The response functions, $W_{L,T,LT,TT}$, contain all the information about the nuclear structure (including the structure of the nucleons), and coupling. This is a very general relation, which we will also need in our discussion of the distorted wave impulse approximation in Section 1.6.2. If we apply all the PWIA assumptions, it becomes possible to factor the sum in Eq. (1.14) into a part depending only on the electron-proton interaction, and a part containing all

the information about the distribution of protons in the nucleus [20, 34]:

$$\frac{d^6\sigma}{d\epsilon d\Omega_{e'} dE' d\Omega_{p'}} = p' E' \sigma_{ep} S(E, \vec{p}). \quad (1.15)$$

Here σ_{ep} is the (off-shell) electron-proton cross-section, and $S(E, \vec{p})$ is called the spectral function. This factorization is a feature of the model, and is not present in more realistic models, though factorization can be restored in some forms of the distorted wave impulse approximation [20].

The correct off-shell cross-section for electron-proton interactions is not known. Many models exist [35], from which we have selected deForest's σ^{cc1} which is arrived at by forcibly restoring current conservation [34].

The spectral function represents the distribution of protons in the nucleus. It can be interpreted as a product of the average number of protons having momentum \vec{p} and the probability per unit energy interval to leave the residual $A - 1$ nucleon system with total binding energy $E + E_A$ in its center of mass after removing a proton having momentum \vec{p} [20]. That is to say, $S(E, \vec{p})$ is a probability distribution for the experimentally observed missing energy and momentum.

1.6.2 DWIA

We want to calculate how the FSIs change with increasing Q^2 , by allowing the struck proton to interact with the nuclear remnant via mean field optical models [3]. This distorts the proton's plane wave expression leading to the moniker Distorted Wave Impulse Approximation, or DWIA.

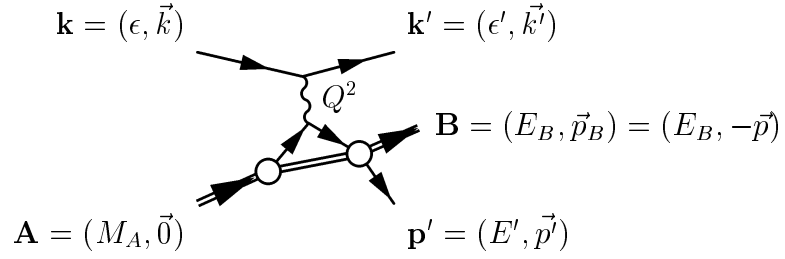


FIG. 1.6: Conceptual diagram for the Distorted Wave Impulse Approximation.

While the PWIA is represented by the bottom panel of Fig. 1.1, the DWIA is more accurately depicted as in Fig. 1.6—after interacting with the virtual photon, the proton is subject to a potential given by the mean field of the nucleus.

This re-interaction destroys the factorization of the cross-section into the fundamental e - p cross-section and a spectral function dependent only on the nuclear structure. Factorization can be re-introduced with the application of some additional assumptions [20].

The formalism is the same as for the PWIA up to Eq. (1.14), except that we now no longer expect the outgoing proton to be described by a plane wave.

The nuclear structure functions, $W_{L,T,LT,TT}$, are written in terms of sums over the scattering amplitudes, G'_μ [20]:

$$W \propto \sum \text{Re}(G'_\mu G'^*_{\nu}), \quad (1.16)$$

where $\mu, \nu \in (0, +, -)$ are spin indices, and the matrix elements are described by²⁰

$$G'_\mu \propto \iint d\vec{p} d\vec{p}'' \langle \vec{p}', \vec{p}_B | a^+(\vec{p}'') a(\vec{p}) | \vec{p}_A \rangle \langle \vec{p}'' | J_\mu(0) | \vec{p} \rangle, \quad (1.17)$$

for the PWIA, and by

$$G'_\mu \propto \iint d\vec{p} d\vec{p}'' \overline{\langle \vec{p}', \vec{p}_B |} a^+(\vec{p}'') a(\vec{p}) | \vec{p}_A \rangle \langle \vec{p}'' | J_\mu(0) | \vec{p} \rangle, \quad (1.18)$$

for the DWIA. The overline represents the distorted state.

The crucial difference lies in how the destruction operator acts on the final states:

$$a(\vec{p}) | \vec{p}', \vec{p}_B \rangle = (2\pi)^3 2p_0'' \delta(\vec{p}'' - \vec{p}') | \vec{p}_B \rangle \quad (1.19)$$

$$a(\vec{p}) \overline{| \vec{p}', \vec{p}_B \rangle} = (2\pi)^3 2p_0'' \chi^{(-)}(\vec{p}', \vec{p}'') | (\vec{p}_A, \vec{p}) \rangle. \quad (1.20)$$

Frullani and Mourgey describe $\chi^{(-)}(\vec{p}', \vec{p}'')$ as “a function representing the distorted-wave function of the outgoing proton in momentum space,” then go on to write:

One sees that, in contrast with the PWIA case, it is not possible within DWIA to deduce exactly the momentum \vec{p} of the proton in the interior of the nucleus from the measurement of the asymptotic momenta in the initial and final states. However the structure of χ ensures that for a given value of \vec{p}' only a limited range of values \vec{p}'' gives significant contributions to the reaction rate. The effect of the [final state interactions] can be understood using its analogy in optics, i.e., the change of the wavelength of light in a dispersive medium.

²⁰In the interest of keeping the notation of this section as clear as possible, I will steadfastly neglect the spin indices and operators.

It is this inability to uniquely determine the proton's "original" momentum that prevents the simple factorization that occurs in the PWIA case.

One can introduce the distorted spectral function

$$S^D(\vec{p}_B, \vec{p}', E) = \int d\vec{p} \left| \chi^{(-)*}(\vec{p}', \vec{p}) \right|^2 S(\vec{p}, E) \quad (1.21)$$

where $\chi^{(-)*}$ has been rewritten in the center-of-momentum frame of the scattered hadron and the nuclear remnant. The distorted spectral function is now a function of the recoil momentum of the nucleus because the FSI with the struck proton may have excited the nuclear remnant. We can now rewrite Eq. (1.15) as:

$$\frac{d^6\sigma}{d\epsilon d\Omega_{e'} dE' d\Omega_{p'}} = p' E' \sigma_{ep}(\vec{q}, \vec{p}', \vec{p}_A - \vec{p}_B) S^D(\vec{p}_B, \vec{p}', E). \quad (1.22)$$

However, for experimental convenience, we assume the existence of an effective spectral function, $S^{\text{eff}}(\vec{p}', E)$, such that we regain the previous factorization:

$$\begin{aligned} \frac{d^6\sigma}{d\epsilon d\Omega_{e'} dE' d\Omega_{p'}} &= p' E' \sigma_{ep} S^{\text{eff}}(\vec{p}', E). \\ &= p' E' \sigma_{ep} \int d\vec{p}_B S^D(\vec{p}_B, \vec{p}', E). \end{aligned} \quad (1.23)$$

The first line of the above defines an experimental observable (the effective spectral function), which is not unique to the theoretical analysis. The second gives its relationship to the theoretical distorted spectral function that appears in the DWIA.

1.6.3 Glauber approximation

An alternative to doing a more complete treatment of the main scattering event is to break the interaction into a principle scattering event that takes place via the PWIA, and then treat the strong final-state interaction by a separate formalism. This is the approach taken by the so-called Glauber models [8, 36].

Following the treatment of Benhar et al. [37], we are going to continue to use (the experimentally convenient) Eq. (1.23). We write

$$S(E_m, \vec{p}_m) = \sum_f |M_f(\vec{p}_m)| \delta(E_m + E_{A-1,f} + m_p - m_A). \quad (1.24)$$

Here $M_f(\vec{p}_m)$ is the matrix element for quasi-elastic scattering into final state f of the remnant nucleus. The delta function serves to enforce energy conservation. If we neglect the center of mass correlations (implying $A \gg 1$), and number the nucleons so that the struck proton is labeled “1,” we can write this as:

$$\begin{aligned} M_f &= \int d\vec{r}_1 \exp(i\vec{p}_m \vec{r}_1) M_f(\vec{r}_1) \\ &= \int d\vec{r}_1 \exp(i\vec{p}_m \vec{r}_1) \int d\vec{r}_2 \dots d\vec{r}_A \Psi^*(\vec{r}_2 \dots \vec{r}_A) \Psi(\vec{r}_1 \dots \vec{r}_A) R(\vec{r}_1 \dots \vec{r}_A) \end{aligned} \quad (1.25)$$

where $\Psi(\vec{r}_1 \dots \vec{r}_A)$, and $\Psi^*(\vec{r}_2 \dots \vec{r}_A)$ represent the pre-interaction nucleus, and the post-interaction nuclear remnant, respectively, and $R(\vec{r}_1 \dots \vec{r}_A)$ describes the FSIs.

The Glauber approximation is that the subsequent scattering of the struck proton occurs overwhelmingly in the forward direction, so, to first order, we can treat the proton as having a well defined, straight path through the nucleus. The precise conditions which need apply are:

- Typical nucleon-nucleon scattering angles, θ are small: $\theta^2 kd \ll 1$.
- The scattering occurs at “high energy”: $\frac{V}{T_k} \ll 1$, and $kd \gg 1$.
- The nucleus is frozen: we can neglect the motion of the unscattered nucleons as the struck nucleon propagates through the nucleus.
- The incident proton interacts separately with each target nucleon.

The symbols that appear in the inequalities are: d , the nucleon-nucleon interaction radius; k , the scattered proton’s wave number; V , the depth of the nucleon-nucleon potential; and T_k , the struck proton’s kinetic energy.

Under these conditions (and neglecting the longitudinal extent of the nucleon), we can write:

$$R(\vec{r}_1 \dots \vec{r}_A) = \prod_{j=2}^A \left[1 - \Theta(z_j - z_1) \Gamma(\vec{b}_j - \vec{b}_1) \right], \quad (1.26)$$

for $\Theta(z)$ the Heavyside step function, and $\Gamma(\vec{b}_j - \vec{b}_1)$ the profile function for elastic proton-nucleon scattering in terms of the impact parameters \vec{b}_i of the nucleons.²¹ Nikolaev chooses a high energy parameterization for Γ :²²

$$\Gamma(b) = \frac{\sigma_{tot}(pN)(1 - i\alpha_{pN})}{4\pi B_{pN}} \exp \left[-\frac{b^2}{2B_{pN}} \right], \quad (1.27)$$

for $\sigma_{tot}(pN)$ the total proton-nucleon cross-section, α_{pN} the ratio of the real to imaginary part of the forward elastic pN amplitude, and B_{pN} the t -dependent diffractive slope describing the same cross-section [36].

²¹Here the nucleon radius vectors, \vec{r}_i , have been decomposed into position along the direction of the struck protons motions, z_i , and position perpendicular to that motion, \vec{b}_i .

²²The profile function is the Fourier transform of the form factor: the spatial distribution of charge in the target nucleus.

The Heavyside function in Eq. (1.26) does not appear in the original Glauber paper [8], as that paper concerns a proton traversing the entire nucleus, while in quasi-elastic scattering, some of the nucleons may start “behind” the struck proton, and not contribute. This expression neglects the longitudinal extent of the nucleon, which causes some difficulty in the theoretical calculation of the longitudinal missing-momentum distribution. This can be overcome by the use of a less abrupt cut-off function [36].

We are now able, in principle, to evaluate the spectral function for this reaction knowing only the initial state of the system (i.e. the ground state wave function of the target nucleus). But we still haven’t said anything about color transparency. So far we have followed the basic Glauber formalism, in which the proton-nucleon interaction is treated as constant.

Again we follow Nikolaev, and make the substitution:

$$R(\vec{r}_1, \vec{r}_2, \dots \vec{r}_A) \Rightarrow \frac{\langle p | \hat{R}_{3q}(\vec{r}_1, \vec{r}_2, \dots \vec{r}_A) | E \rangle}{\langle p | E \rangle} \quad (1.28)$$

in which $|p\rangle$ and $|E\rangle$ represent the physical proton and the ejectile state respectively, and \hat{R}_{3q} represent the (generally time-dependent) interaction between the evolving ejectile state and the remnant nucleus.

It is the presence of \hat{R}_{3q} which gives rise to color transparency effects. The newly introduced operator can be computed by path-integrals or multiple-scattering methods [36], but Gribov’s multiple-scattering formalism is fully quantum mechanical, is easy to use, and admits approximation at any convenient level. [18, 37].

2. EXPERIMENTAL EQUIPMENT

The standard detector and instrumentation suite of Hall C is well suited to the high Q^2 scattering needed for e94-139. No modifications of the equipment were needed, though a photon radiator was installed upstream of the target to accommodate e96-003 (Photo-disintegration of the Deuteron) which was running in the same time period. The radiator was not used by this experiment.

A color transparency measurement has fairly simple experimental requirements. We need to make a coincidence measurement in quasielastic kinematics with E_m and p_m resolution on order of the size of the structures we wish to resolve, particle identification sufficient to eliminate contamination by other reactions (say $A(e, \pi p)$) and random coincidences to less than 1% of the yield, and sufficient luminosity to provide statistics commensurate with the scale of our other uncertainties. The scale of spectral function features is 5–10 MeV in missing energy, and somewhat more than that in missing momentum.

2.1 Accelerator and Beam

The CEBAF accelerator is a versatile device capable of providing high-quality, high-intensity, high-duty factor, tightly-focused beam to three experimental halls simultaneously with relatively few constraints imposed between the halls. The accelerator consists of an injector, and two super-conducting linacs

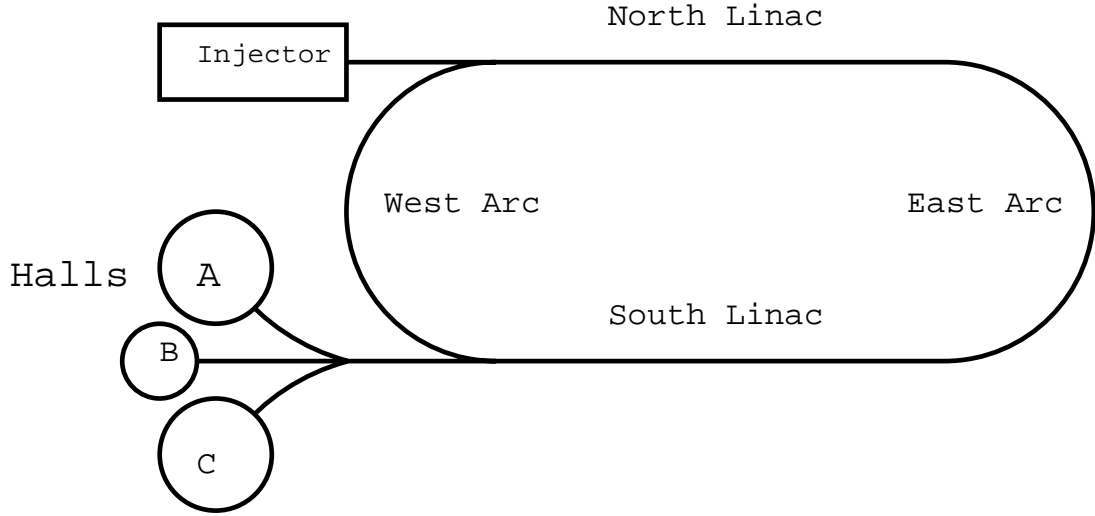


FIG. 2.1: Overhead schematic of CEBAF.

connected by recirculating arcs formed into a “racetrack” configuration as shown in Fig. 2.1. The beam makes between one and five passes through the linacs before being switched to the experimental halls at the west end of the south linac.

In continuous wave (CW) operation the accelerator delivers bunches of electrons at a frequency of 1497 GHz. Because the beam is shared between the three experimental halls, each hall receives a beam with a 2 ns bunch spacing.

CEBAF is designed to deliver as much as 200 μA total beam to the three experimental halls, and can deliver high polarization, and several different energies independently to the three halls.¹

¹The energies are constrained by the requirement of making an integer number of passes through the linacs. Further, polarization delivered at the hall depends on precession in the arcs, and cannot be set arbitrarily in more than one hall at a time. However, the injector can deliver polarized beam in some halls, and unpolarized beam in the others.

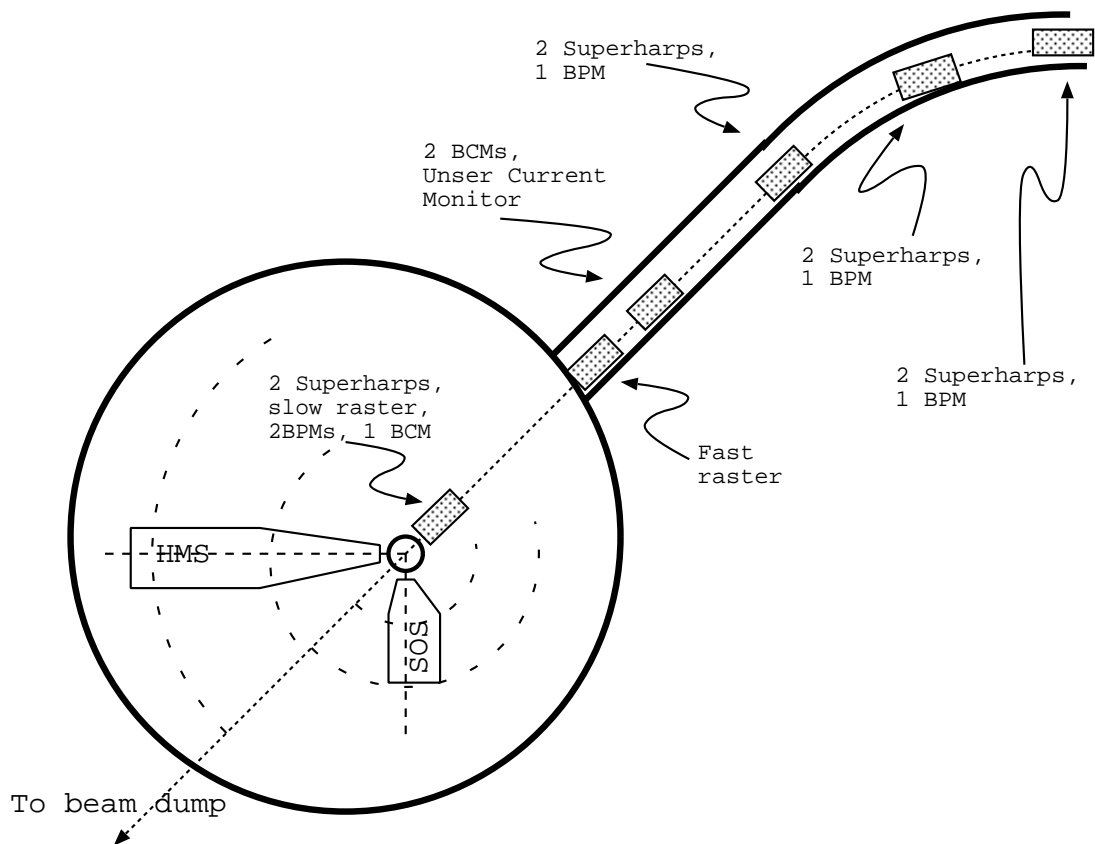


FIG. 2.2: Overhead schematic of Hall C and the Hall C beamline, indicating the position of beamline instrumentation. Here we write BCM for Beam Current Monitors, and BPM for Beam Position monitors. All beamline devices are discussed later in this chapter.

E94-139 took unpolarized CW beam at currents up to $60\mu\text{A}$, and energies between 3.0 and 5.5 GeV.

2.2 Layout and Nomenclature of Hall C

The layout of Hall C is sketched in Fig. 2.2. The beam enters the hall slightly off-center from the north-east approximately five meters above the floor

of the hall, passes through the scattering chamber on the way to the beam-dump to the south-west.

The two spectrometers are mounted on carriages that run on circular tracks on the hall floor, and are fixed to the central pivot by large bearings.

The scattering chamber sits atop the pivot at the same height as the beam line.

2.3 Beamline Instrumentation

The Hall C beamline instrumentation is able to accurately measure the position, current, and profile of the beam. A fast raster system spreads the heat load from the beam over a larger area of the target, and prevents target melting.² Figure 2.2 provides a schematic representation of Hall C, and shows the relative positions of the detectors, and the beamline instrumentation.

2.3.1 Beam Position Monitors

The beam position monitors (BPMs) used in Hall C (and in the accelerator) are cylindrical cavity resonators. The cavity is shaped and positioned so that the beam's fundamental frequency excites the *TEM* modes of the cavity. Four antennas positioned around the cavity receive a signal in this band that is proportional to the distance of the beam from the antenna. Once the antenna gains have been properly normalized, the position of the beam can then be found in terms of differences over sums of these signals: a procedure that makes the measurement independent of beam current [38]. Absolute position accuracy of the cavity BPMs is about ± 1 mm, with relative accuracy better than a fifth of that [39]. The BPMs can be calibrated to absolute position by using the superharp

²Well, mostly. See Section 5.6.1.

monitors (see Section 2.3.2), but this was not done for the running of e94-139. Instead, the BPMs were set to their nominal values, and the beam steered until it fell in the nominal position (as seen through the scattering chamber window on the monitor in the counting house), then the reading of the BPMs were noted. For the rest of the experiment, the beam was steered to these values.

2.3.2 Superharp and the Beam Profile

The superharps are forked frames with three tungsten wires mounted so that they can pass the wires through the beam path. An analog-to-digital converter (ADC) reads out the secondary emission on the wire caused by the beam. Driven by a stepper motor and monitored by a shaft encoder, the superharps can accurately measure the position and profile of the beam (albeit in a destructive way), and can measure the beam deflection in the Hall C arc to sufficient accuracy (less than $20\text{ }\mu\text{m}$) to provide a 10^{-3} measurement of the beam energy [40].

2.3.3 Beam Current Monitors and Charge Measurement

The beam current (and thus the charge on target) in Hall C is measured by three resonant-cavity beam current monitors (BCMs)³, which provide very good relative current measurement, but experience substantial gain and zero drift on a time scale of a few days. These are calibrated against an Unser monitor: a device with a noisy signal, but very good gain stability and the added advantage that it can be calibrated against a DC current in a wire [41].

The cavity monitors are similar to the BPMs, but in this case it is the TM_{010} modes which are excited. These modes are relatively insensitive to the position of the beam in the cavity—so the signal is primarily dependent on the

³One of these is actually part of accelerator division’s beam loss monitoring system, but they make its output available to the Hall C data acquisition system.

beam current. The cavities are temperature regulated [42], but still show some gain variation (on order of a few percent) on time scales of a few minutes as their resonant quality varies with changes in their physical parameters [43, 44].

The Unser monitor is a parametric current transformer driven by a 4 kHz signal, and functioning in negative feedback mode. It is not used for primary current measurement because it has a poor signal to noise ratio, and suffers from thermally induced offset drifts. More information can be found in Ref. [41].

2.3.4 Fast Raster

Twenty meters upstream of the target (near the hall entrance) are a pair of fast raster magnets. These are fast dipole coils positioned to allow the beam to be steered either horizontally or vertically. Together they allow the beam to be swept over a significant portion of the target, reducing the point heat load on the target.

The purpose of the fast raster is to spread the (considerable) heating due to the beam over a larger area of the target, thus preventing solid targets from melting, and reducing the current dependence of cryo-target density and in particular hopefully preventing the formation of large bubbles that might cause rapid and significant density fluctuations.

For the 1999 run, the raster controller was rewired to allow either the traditional square (“bedpost”) raster [43], or the newer (“circular”) raster to be used [45].

The square raster was a matter of some concern in earlier Hall C work because it was achieved by driving the raster magnets sinusoidally in each direction creating a very dense Lissajous pattern, but this drive left the beam dwelling

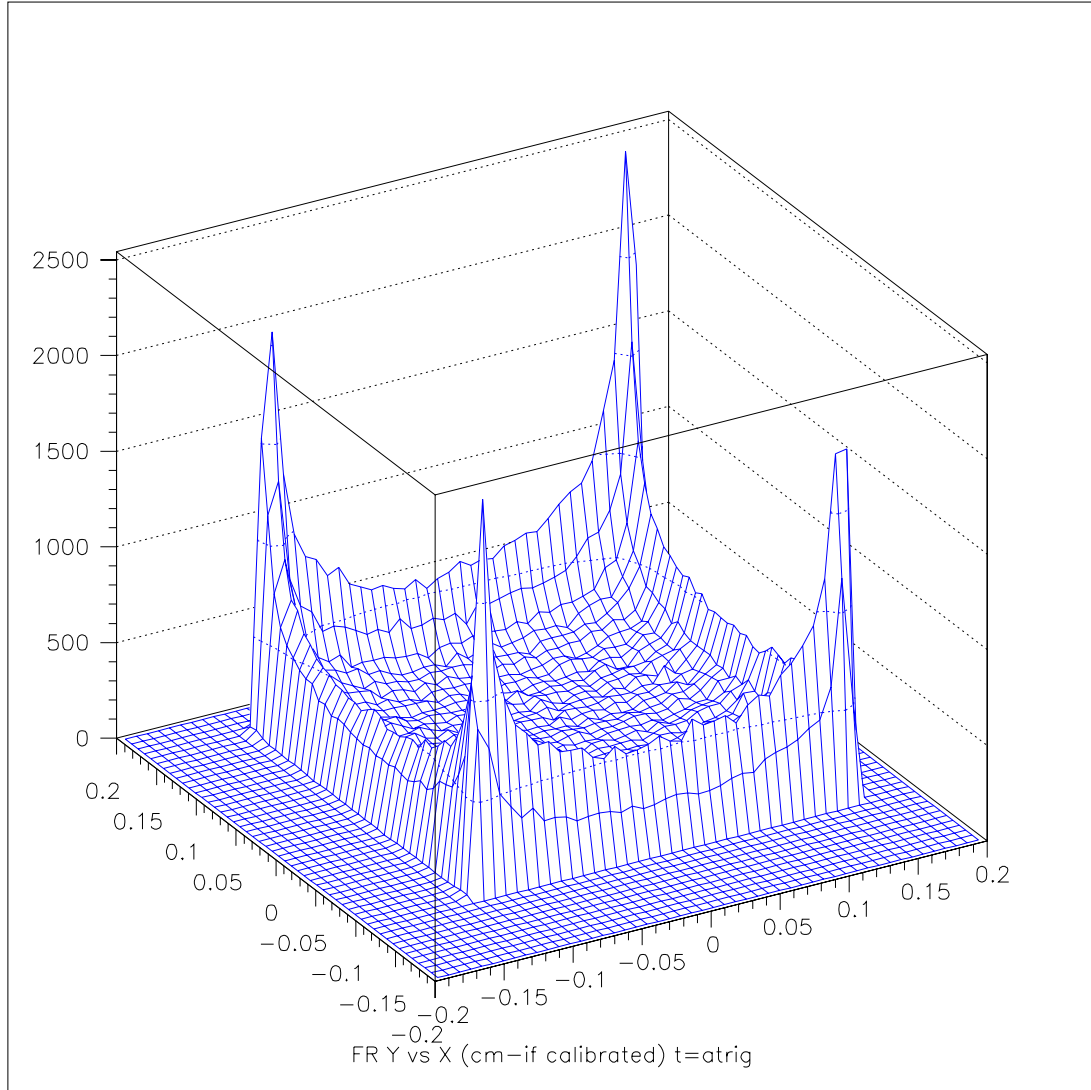


FIG. 2.3: A histogram showing the distribution of the beam due to the fast raster in square (or bedpost) mode.

longer near the edges, and particularly at the corners than in other parts of the pattern. Figure 2.3 shows the distribution of the beam due to the fast raster from one of our data runs. Note the large peak at each of the corners—the source of the bedpost appellation. There was some fear that the large flux through the corner regions was causing more cryo-target boiling and thickness fluctuation than necessary. See Section 3.5 for details of the cryo-target boiling measurements and corrections.

During a machine development downtime, the bedpost raster was modified to provide a “gating” signal to the data acquisition system indicating when the beam spot was moving “quickly.” With the addition of this signal it was hoped that events could be chosen from the bubble free region of the target.

For the circular pattern, the raster is driven in a circle, and the radius is stepped digitally in a pattern that leads to equal total flux through the entire area covered by the raster. The time to sweep the radius defines the raster’s “breathing frequency.”

Most of the e94-139 data was taken with a 1 cm (radius) circular raster, but a few early runs used a 1.5 cm raster, and near the end of the run the bedpost raster was used. The changes were made in part to evaluate the performance of the raster. Luminosity scans were taken under most raster conditions to evaluate the cryo-target density dependence (see Section 3.5).

2.4 Targets

E94-139 made use of ^{12}C and ^{46}Fe solid targets, and liquid-hydrogen and deuterium cryo-targets suspended on vertical target ladders inside the scattering chamber.

TABLE 2.1: Summary of the properties of the e94-139 targets.

#	Material	Thickness (% Rad. lengths)	Length (cm)	Notes
Solid Target Ladder				
1	Fe	$6.04 \pm .02$		
2	Fe	$5.80 \pm .02$		Reused from e89-008.
3	Fe	$2.60 \pm .01$		
4	C	3.		Thickness unknown.
5	C	$2.92 \pm .01$		
6	BeO			Used as a marker only.
Cryo-target Ladder				
11	H	$5.33 \pm .03$	4.52	
15	D	$6.07 \pm .03$	4.45	
17	Al	$2.22 \pm .01$	4.5	Dummy Target

2.4.1 Scattering Chamber

The scattering chamber is an approximately 0.9 cubic meter vacuum chamber mounted on the pivot platform. It contains the solid- and cryo-ladders, and the mechanism for moving these into and out of the beam. Thin windows are provided to reduce the mass which entering and scattered particles must traverse. There is also a transparent window through which a camera may be trained on the target-beam interaction region for visual monitoring from the counting house. Table 2.1 summarizes all the important facts about the targets used in this experiment.

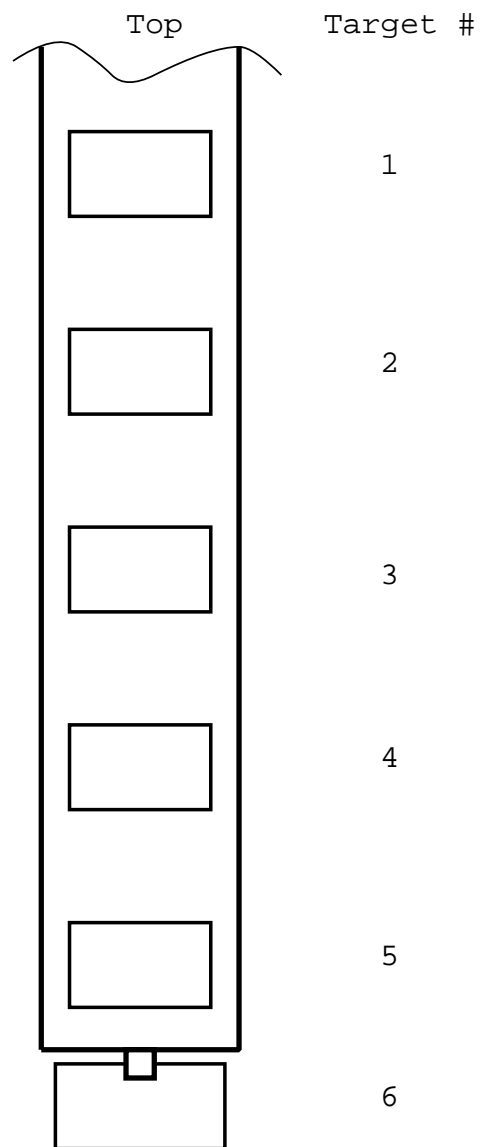


FIG. 2.4: Sketch of the solid target ladder.

2.4.2 Solid Targets

The solid target ladder is a water cooled steel frame holding five targets, and with provisions for an additional target to be hung off the bottom. The actual target ladder was reused from an earlier Hall C experiment. Jim Dunne writes in the Hall C log that it is the “Basel water cooled target ladder #2.” It is sketched in Fig. 2.4 showing the target positions. The bottom target is not effectively cooled, and must be very thin, highly conductive, or able to withstand very high temperatures. In e94-139, we used a thin Beryllium Oxide target in this position—this target shows the beam spot clearly, and was used to steer the beam to its nominal position during startup.

The ladder is constructed of machined steel, with five cutouts approximately 1.5 in width, and .75 in high. Each window has a recessed lip onto which the target is clamped by a rectangular flange bolted onto the front of the target ladder. A copper tube is soldered to the back of the ladder, to allow for the flow of cooling water around all four sides of the targets. The sixth target is attached by means of a slotted cylinder attached to the bottom of the ladder.

2.4.3 Cryo-targets

The cryo-target assembly used in e94-139 holds three loops, each with two longitudinal flow “beer can” targets.⁴ Above and below the cryo-loops are the “dummy” targets which emulate the walls of the cryo-target cells for the purposes of background subtraction. At the bottom of this ladder is an assembly of fixed target foils which provide multiple, discrete, target positions along the direction of the beam (a property which is useful in tuning the optics system).

⁴The shells of these targets are actually constructed from beer can blanks.

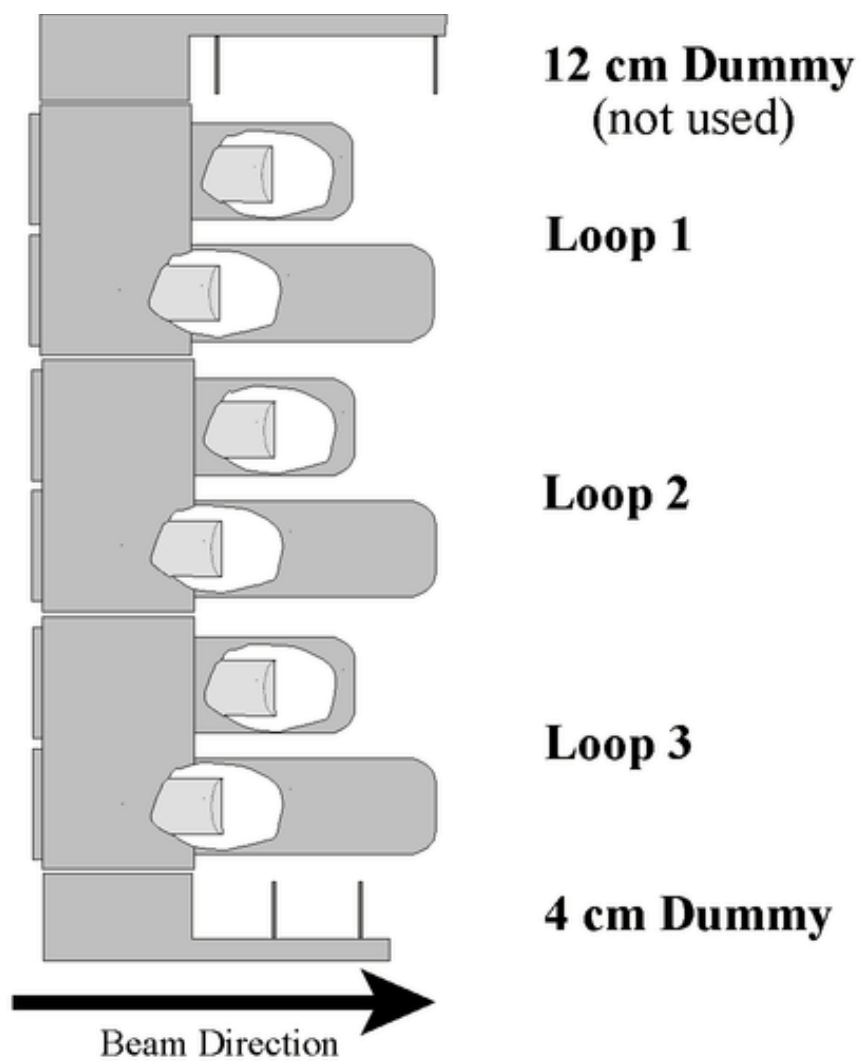


FIG. 2.5: Sketch of the cryo-target ladder.

Figure 2.5 is a sketch of the cryo-target ladder.

2.5 High Momentum Spectrometer

Hall C's High Momentum Spectrometer (HMS) is quad-quad-quad-dipole, point-to-point focusing spectrometer with a 25° bend angle. The detector package for the HMS uses hodoscopes, drift chambers, a Cerenkov detector, and a lead-glass calorimeter to provide accurate particle tracking, fast triggers, and particle discrimination. A collimator system provides a choice of two octagonal acceptance collimators, a sieve collimator, and no collimator.⁵

The nominal specification of both Hall C spectrometers is given in Table 2.2.

2.5.1 Geometry

The HMS provides the ability to analyze particles of momentum considerably higher than the design goals for the CEBAF beam with fairly high acceptance, and accurate reconstruction in space and momentum. Its four focusing elements are super-conducting magnets arranged *QQQD*, and operated in a tune (called the HMS-100 tune [46]) which provided point-to-point focusing in both optical directions [3]. Figure 2.6 is a cartoon of the geometry of the spectrometer.

2.5.2 Detector Stack

As shown in Fig. 2.7, the detector package for the HMS consists of two multi-plane drift chambers, four planes of hodoscopes, a Cerenkov detector, and a

⁵The collimators are made of heavymet (an alloy of 90% tungsten, and 10% CuNi with a density of 17.0 g/cm^3) and serve to limit the acceptance at the entrance window to the first magnet to a region in which the focusing matrix elements are well behaved. The sieve slit consists of a regular grid of holes and is used provide a discrete acceptance for tuning the matrix elements used by the analysis software.

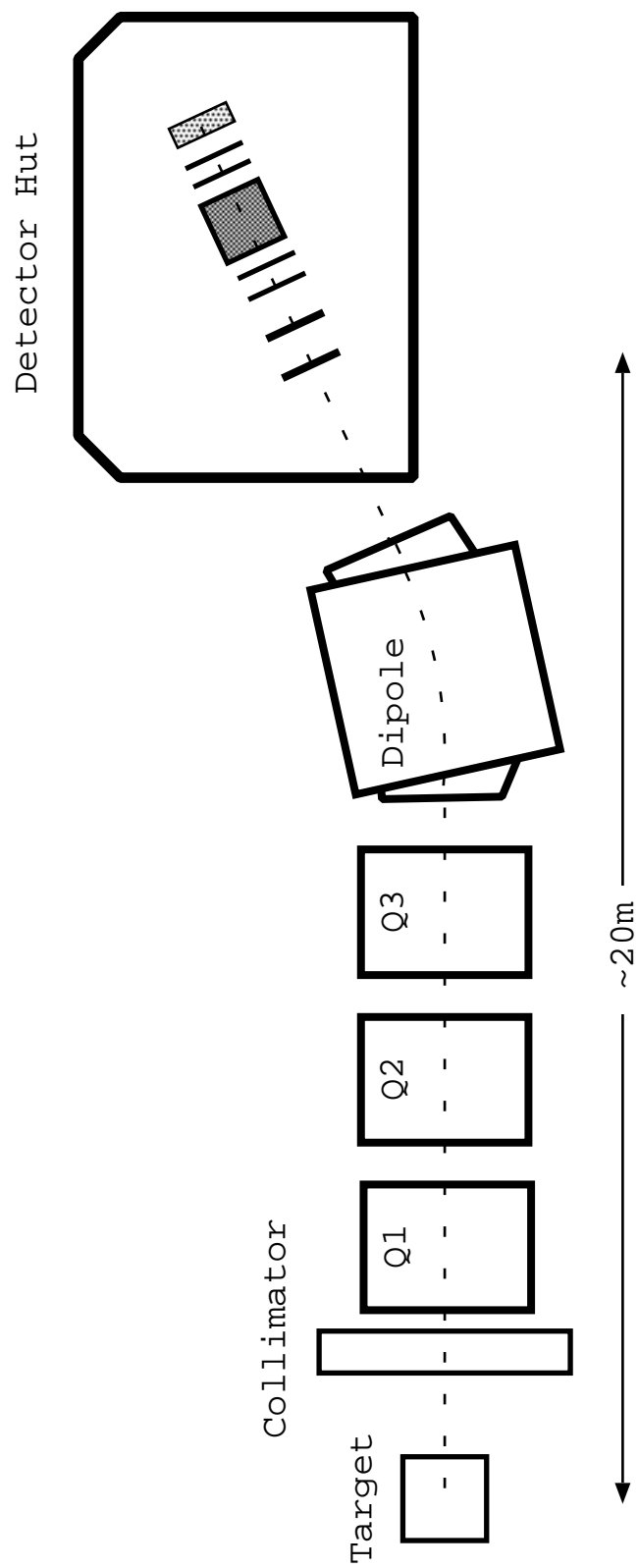


FIG. 2.6: Sketch of the overall geometry of the HMS.

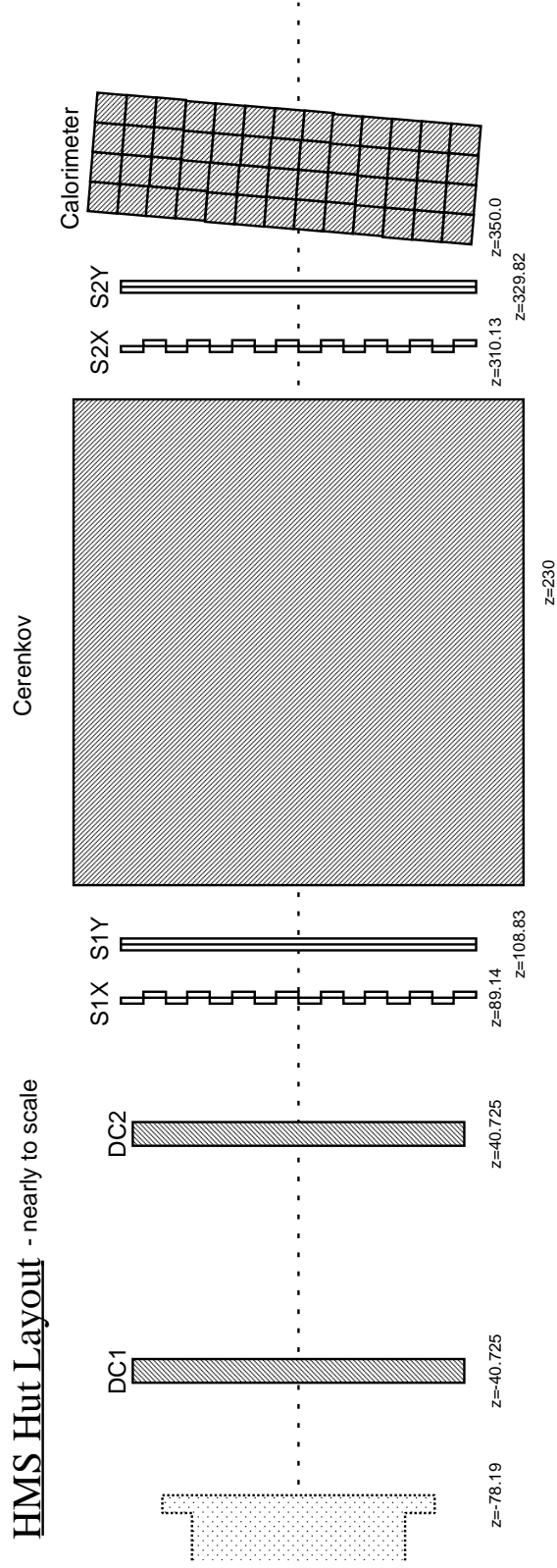


FIG. 2.7: Exploded view of the HMS detector stack. The calorimeter is tilted by 5° relative the rest of the stack to prevent losses through the cracks.

TABLE 2.2: Nominal specification for the Hall C spectrometers

Specification	HMS	SOS	Units
Maximum central momentum	7.4	1.75	GeV/c
Optical length	26.0	7.4	m
Angular range (horizontal)	10.5 - 85	13.4 - 165	degrees
Angular range (vertical)	fixed	0 - 20	degrees
Fractional momentum acceptance	$\pm 10.$	$\pm 20.$	%
Fractional momentum resolution	< 0.1	0.1	%
Solid angle	6.7	7.5	mrاد
In-plane angular acceptance	± 27.5	± 57.5	mrاد
In-plane angular resolution	1.0	2.5	mrاد
Out-of-plane angular acceptance	$\pm 70.$	± 37.5	mrاد
Out-of-plane angular resolution	2.0	0.5	mrاد
Extended target acceptance	$\pm 7.$	$\pm 1.$	cm
Vertex reconstruction accuracy	2.	1.	mm

lead-glass calorimeter. The beam first encounters the two six plane wire chambers, then a set (two planes) of x-y hodoscopes, followed by a gas Cerenkov detector (not used during e94-139), another pair of hodoscopes planes, and finally a lead glass calorimeter.

The hodoscope planes form the positive core of the fast trigger signal (see Section 2.7.1.1), and (with their 220 cm spacing) provide good time-of-flight information. The drift chambers provide high-precision tracking information, while the Cerenkov detector and calorimeters provide particle identification information (both fast vetoes for the trigger, and precise data for the full analysis).

E94-139 did not make use of the particle identification (PID) detectors in the HMS because the coincidence condition with the scattered electron was sufficient to prevent any significant contamination. Because e94-139 shared time

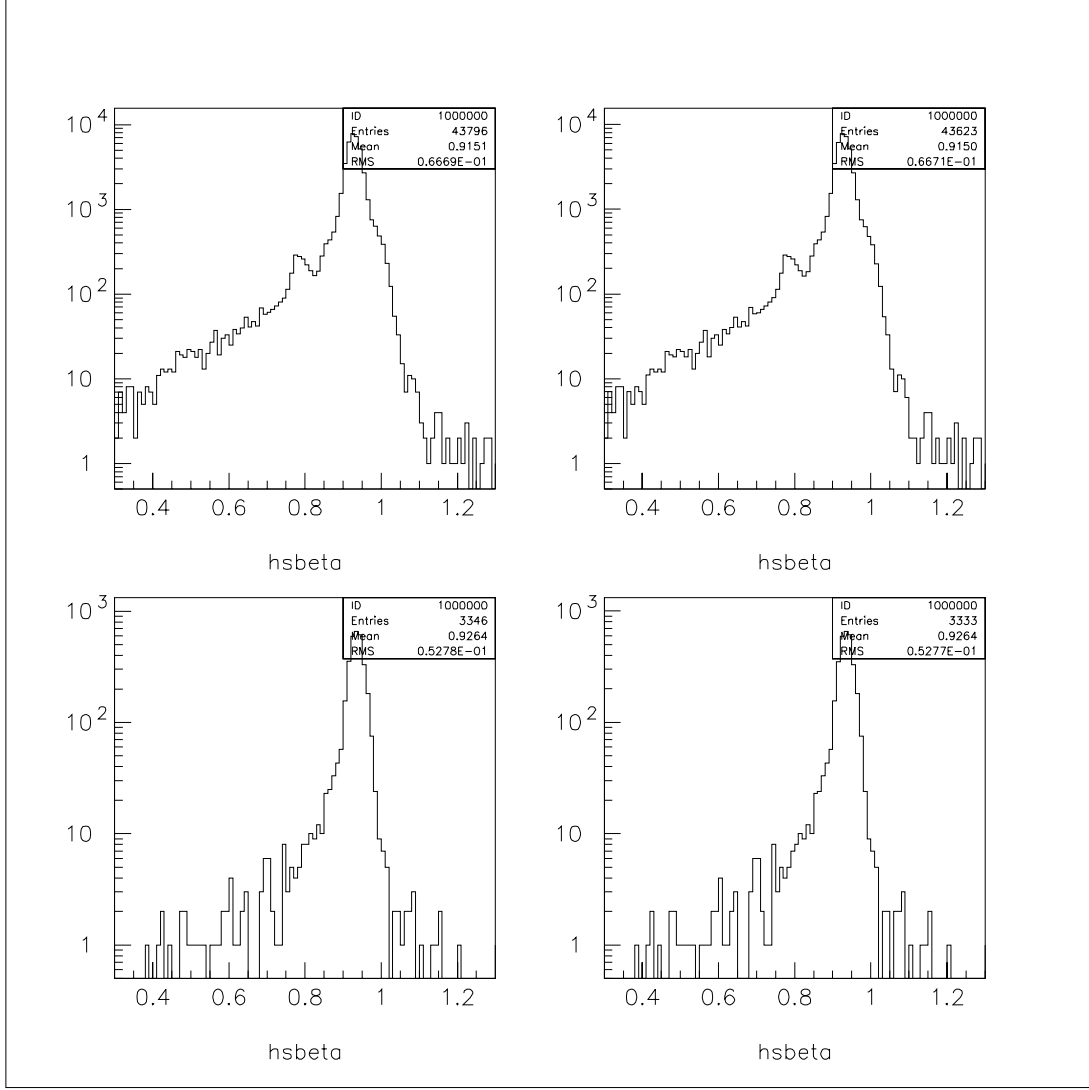


FIG. 2.8: Example particle velocity spectrum (β) in the HMS. The panels are HMS singles with acceptance cuts only (top left), HMS singles with acceptance cuts and fewer than two photons in the Cerenkov detector (top right), coincidence events with acceptance and electron PID cuts (bottom left), and coincidence events with acceptance, electron PID, and the HMS Cerenkov detector.

in the hall with two other experiments, the HMS Cerenkov detector *was* powered up and collecting data during the running of the experiment, which allows us to test this condition. As seen in Fig. 2.8, the results are quite good: neglecting PID in the HMS results in an error of less than one half of a percent.

2.6 Short Orbit Spectrometer

The Short Orbit Spectrometer (SOS) is quad-dipole-dipole, point-to-point focusing spectrometer. The detector package is similar to that in the HMS. Reference [47] is a fairly complete description of the SOS and its detector package at the time of its installation.

2.6.1 Geometry

The SOS was originally intended to function as a hadron arm of the Hall C detector pair, and as such has a very short optical path to enable it to detect short-lived particles (e.g. kaons). Its geometry is governed by this requirement combined with modest central momentum requirements, and large acceptance goals. Figure 2.9 is a cartoon of the geometry of the spectrometer.

The three resistive magnets are ordered $QD\overline{D}$, with the quadrupole focusing in the non-dispersive direction, the first dipole providing a 33 degree bend, and the second dipole bending 18 degrees in the opposite direction. The dipole fields also have significant higher order components which contribute to the focusing [48]. The magnets are operated in a tune which provides point-to-point focusing in both the dispersive and non-dispersive directions [43].

The SOS is equipped with hydraulic jacks capable of raising it as much as 20 degrees above the nominal scattering plane (horizontal) [47]—a feature of the device not yet exploited. A side effect of this feature is that the SOS actually lies

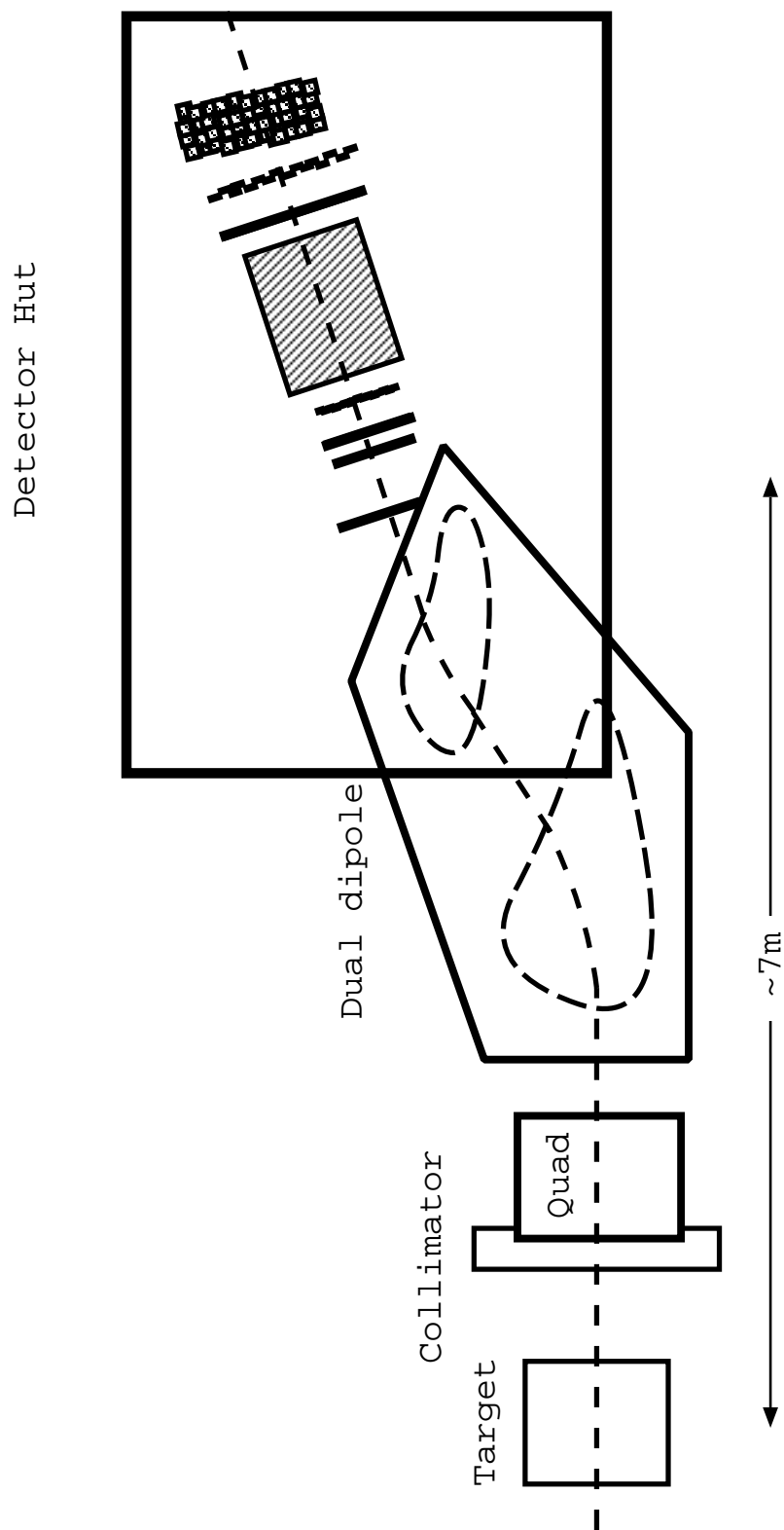


FIG. 2.9: Sketch of the overall geometry of the SOS.

about 0.15 degrees below the scattering plane if the jacks are not used to level it. Standard procedure is to neglect the jacks, and compensate in software, and we did so during e94-139.

2.6.2 Detector Stack

The SOS detector stack (shown in Fig. 2.10) is materially similar to that of the HMS. This similarity is a design feature which allows the two spectrometers to be used interchangeably as the electron- and hadron- detectors, and enables parallel construction of the trigger electronics and analysis software for the two devices.

2.7 Data Acquisition

Data acquisition in the Hall C standard equipment is handled with a simple hardware trigger which feeds into a VME based trigger supervisor, and thus into software via the CEBAF Online Data Acquisition (CODA) package. The software (running on a HP 9000/735 workstation dedicated to this task) gathers the disparate parts of each event, and builds a single event record which is written to disk, and eventually copied to tape.

2.7.1 Readout Electronics and Triggering

To get the maximum available information from each detector element, it is necessary to know both how large a signal was observed and when it occurred. This is achieved through the use of a combined ADC, discriminator, TDC strategy.⁶ Raw (preamplified) signals from the individual detectors are split, one portion going through a delay line to an ADC, the rest after going through a

⁶ADCs and TDCs are analog to digital converters and time to digital converters. They serve to convert signal amplitudes and timing to digital values suited to consumption by computers.

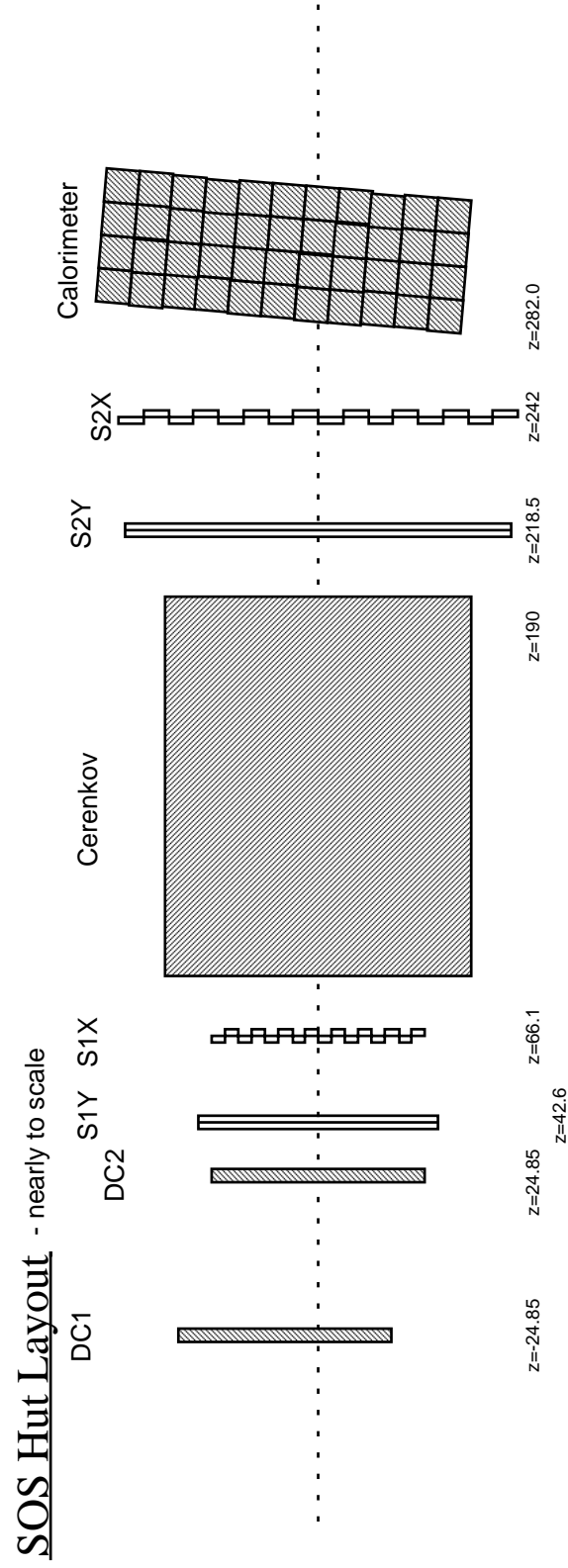


FIG. 2.10: Exploded view of the SOS detector stack. The calorimeter is tilted by 5° relative the rest of the stack to prevent losses through the cracks.

discriminator (and possibly some logic) gets fanned out to the trigger electronics and a delay line leading to a TDC and a scaler. Detailed information for each detector can be found in Ref. [43].

The delay lines are designed to allow the trigger (if it forms a signal) to latch the ADC, TDC, and scaler units for readout. Then the raw scalers, and the ADC and TDC signals from all the detectors in the hall are gathered in several VME and FASTBUS crates. The signals from the hodoscopes and particle identification (PID) detectors are also used to generate the signals which form the hardware trigger.

2.7.1.1 Hardware Trigger

The cabling which transports the triggering signals to the counting house (where the actual trigger is formed, and the trigger supervisor resides) is designed so that signals from lightcone particles emanating from a single event will all reach the counting house at roughly the same time.

The trigger electronics for each spectrometer are substantially the same—they differ only in the number of each type of detector⁷—so we will describe the system generically.

The (relatively) primitive trigger signals we form are:

- For each plane of hodoscopes, we form the logical *or* (\vee) of all the tubes on the positive (negative) side, and call this S1X+ (S1X-), S1Y+ (S1Y-), S2X+ (S2X-), or S2Y+ (S2Y-) depending on the position in the detector stack and orientation of the plane. Planes labeled X (Y) are oriented horizontally (vertically) to provide information about the vertical (horizontal)

⁷And in the name. All trigger signals names given here also take a prefix of either an “H” or an “S” depending on whether they derive from the HMS or the SOS.

Spectrometer Trigger

4/5/99

logic updated April 99, some
gate locations have changed

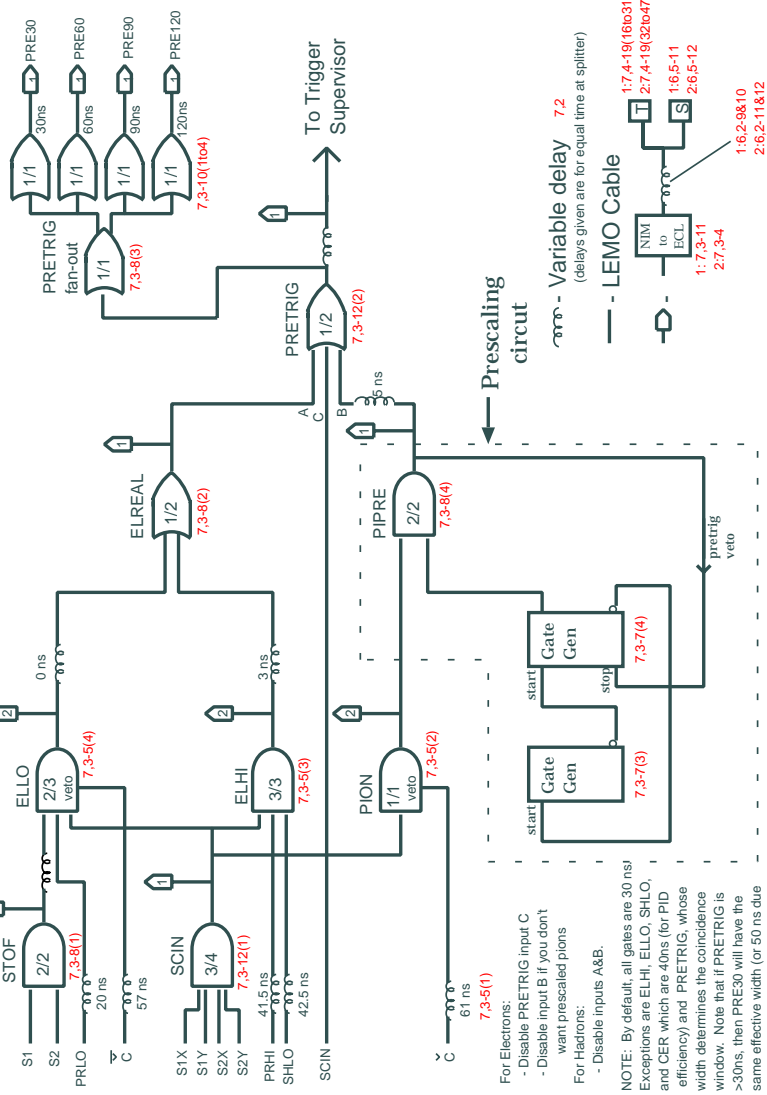


FIG. 2.11: Schematic of the single arm trigger used in e94-139. Figure from the Hall C documentation [49].

position of the particle. This is consistent with the coordinate system used by the analysis engine. See Section 3.1.1. The planes of each orientation are numbered in the order they are encountered by beam particles. That is plane 1X lies between the drift chambers and the Cerenkov detector, while plane 2Y lies between the Cerenkov detector and the calorimeter. See Sections 2.5.2 and 2.6.2.

- For each plane of hodoscopes we form the logical *and* (\wedge) of the positive and negative side signals to get S1X, S1Y, S2X, and S2Y.
- Front pair and back pair signals are formed from the logical *or* of the X and Y signals, e.g. $S1 = S1X \vee S1Y$.
- The “time of flight” trigger is $STOF = S1 \wedge S1$.
- The scintillator trigger, SCIN, is formed by requiring a signal on three out of the four hodoscope planes.
- The Cerenkov signal requires two photo-electrons in the appropriate detector.
- The signals from the calorimeter are summed to give the total energy deposited in each layer. Then the trigger PRHI (PRLO) is set if the energy in the first layer exceeds a high (low) threshold. The signal SHLO is set if the total calorimeter energy exceeds another threshold.

These signals are used to construct electron triggers (with or without prescaled pions) or hadron triggers as shown in Fig. 2.11. The trigger to accept is set by manually moving pins on the front panel of ROC 0 in the counting house.⁸

⁸ROC 0 is one of the rack mounted VME controllers that run the DAQ system. Also known as VME3 [50].

An electron trigger (ELREAL) can be formed several ways. A three out of four signal (SCIN) with a Cerenkov signal will form an electron trigger, as will SCIN with PRHI and SHLO. An electron trigger can also be formed with hodoscope hits in the front and rear planes (STOF), the Cerenkov detector, and PRLO. If prescaled pions are being accepted, they require SCIN and no Cerenkov signal.

A hadron trigger simply requires hits in three of four scintillator planes.

All of the trigger electronics have a gate width of 30 ns, except the SOS calorimeter composite signals (PRLO, PRHI, and SHLO) which were set to a gate width of 40 ns. Also, the pretrigger signal is split into several extra signals with equal or longer gate widths to enable a measurement of the electronic dead time. See Section 3.3.2.

2.7.1.2 Trigger Supervisor and 8LM

The single-arm, hardware triggers generated so far (called pretriggers) are fed into a LeCroy LC2365 8LM programmable logic module which blocks signals when the trigger supervisor is busy and generates eight output signals which are sent on to the trigger supervisor (and to the visible scalers in the counting house). The trigger supervisor decides what kind of event is to be recorded, and starts the readout of the data crates.

The 8LM reads in seven signals—four pretrigger signals (HMS, SOS, the pedestal pretrigger, PED, which comes from a pulser, and $\text{COIN} = \text{HMS} \wedge \text{SOS}$), and three condition signals from the trigger supervisor. The condition signals are GO which is set while running, EN1 which is set during normal data taking (as opposed to pedestal which generates the signal PED), and BUSY which is set while the trigger supervisor is reading out an event. From these inputs, the

Trigger Supervisor

5/10/99

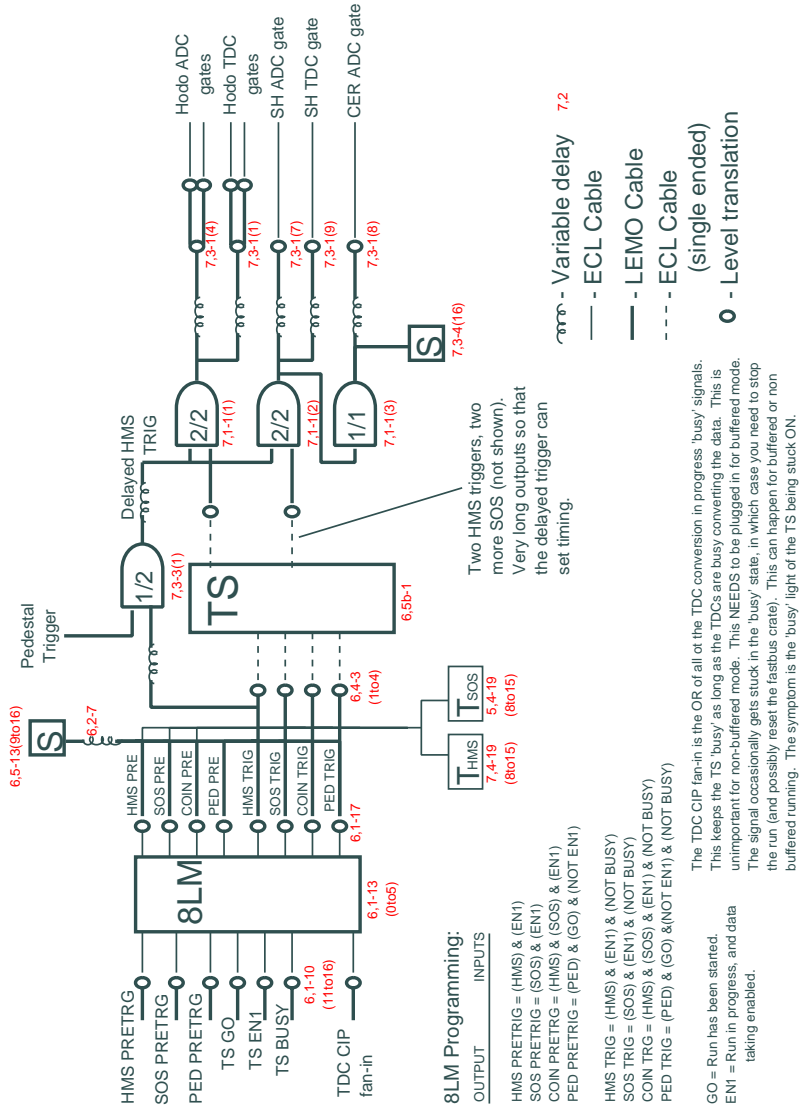


FIG. 2.12: Schematic of the 8LM and trigger supervisor used in e94-139. Figure from the Hall C documentation [51].

TABLE 2.3: 8LM trigger logic

Signal	Definition
HMS PRETRIG	$(\text{HMS}) \wedge (\text{EN1})$
SOS PRETRIG	$(\text{SOS}) \wedge (\text{EN1})$
COIN PRETRIG	$(\text{COIN}) \wedge (\text{EN1})$
PED PRETRIG	$(\text{PED}) \wedge (\text{GO}) \wedge (\overline{\text{EN1}})$
HMS TRIG	$(\text{HMS}) \wedge (\text{EN1}) \wedge (\overline{\text{BUSY}})$
SOS TRIG	$(\text{SOS}) \wedge (\text{EN1}) \wedge (\overline{\text{BUSY}})$
COIN TRIG	$(\text{COIN}) \wedge (\text{EN1}) \wedge (\overline{\text{BUSY}})$
PED TRIG	$(\text{PED}) \wedge (\text{GO}) \wedge (\overline{\text{EN1}}) \wedge (\overline{\text{BUSY}})$

8LM generates eight output signals: a PRETRIG and TRIG signal each for HMS, SOS, COIN, and PED. The trigger logic is shown in Table 2.3. Figure 2.12 is a schematic of the 8LM and trigger supervisor.

The 8LM can also prescale each of the data triggers independently by a programmable factor [43]. In e94-139, we kept the coincidence prescale factor at 1, but adjusted the single arm prescales as necessary to keep the rates reasonable. Note that this prescaling is different from the prescaled-pions option in the hardware trigger which allows a metered number of pion events to be recorded in a run intended to take electron data.

Note that the PRETRIG signals are forwarded to the scalers even when the trigger supervisor is busy. This feature enables a measurement of the computer dead time as described in Section 3.3.1.

2.7.2 Retiming

As shown in Fig. 2.12, after the 8LM forms a pretrigger, the signal is sent both to the trigger supervisor, and to a scaler, then routed around the trigger supervisor on a delay line where it is logically anded with a pair of long timing pulses from the trigger supervisor. This allows each spectrometer to set the timing for its own ADCs and TDCs, instead of having the timing set by the coincidence trigger signal, which will be correct for one spectrometer, but result in mis-timing the readout for the other arm. This procedure is called retiming.

2.7.3 DAQ

All the data needed to perform the analysis should be stored in one place. Collecting it is the job of the data acquisition software: CEBAF Online Data Acquisition or CODA [52].

CODA collects data from events, scalers and slow controls, and writes it so a single data stream on disk. Event reading is triggered by the 8LM, and causes CODA to readout the VME and FASTBUS crates. Scalers are sampled every two seconds, and written into the data stream separately (to allow rapid analysis, and idiot checking). The slow controls are those constant or slowly changing parameters, like high voltage settings, magnet excitation, and feedback from the beamline instrumentation, which are needed to perform the analysis, but are not part of the detector package output. The slow controls are read by EPICS [53], and entered into the data stream every thirty seconds.

3. ANALYSIS ENGINE AND CORRECTIONS

Reduction of the raw data to a usable form is performed by the Hall C analysis engine. Events written to the data stream are analyzed for tracks, particle identification (PID), and physics variables. Post-reduction analysis is mostly performed in CERN's computer analysis environment, PAW [54].

We summarize the behavior of the analyzer, and identify a number of known corrections for systematic losses in the experiment and software.

3.1 Analysis Engine

The Hall C analysis engine is a Fortran program called Replay.¹ Replay reads the raw data tapes written by the data acquisition system, locates possible tracks, identifies particles, builds physics events, calculates meaningful variables for those events and writes out the results in a usable format. Replay makes extensive use of CERNLIB's HBOOK engine [55], providing diagnostic output as histograms, and the event-by-event reconstructed results as a series of ntuples.² This allows much of the later analysis to be done using PAW [54].

¹Actually this program does not seem to have a well defined name. In the earliest documentation it is referred to as "the Hall C analysis engine." In various theses and internal documents, it is referred to as "ENGINE," "Engine," "REPLAY," and "Replay." In a Unix environment, the executable program is usually "replay," and this is also common spoken usage. I will use Replay.

²HBOOK provides two structures for storing data. The histogram structure corresponds very closely to the generally use of the term. The other structure, called an ntuple, is a sequence of fixed format n -tuples.

3.1.1 Coordinate Systems and Naming Conventions

There are several coordinate systems used in Hall C. The systems that are relevant to the analysis engine are the Hall C Laboratory Coordinate System, and the system used by Replay for each spectrometer.

The Hall C Laboratory Coordinate system has its origin at the intersection of the theoretical beam path and the pivot axis, and is a right-handed coordinate system with z pointing along the beam direction, and x directed down along the pivot axis [56].

In each spectrometer we define a (TRANSPORT-like³) system with z defined as being always along the direction of the central ray from the pivot into the spectrometer. The x coordinate initially agrees with the laboratory system, and always lies in the vertical plane containing z . These are also right-handed systems, so y increases towards smaller (larger) spectrometer angles in the HMS (SOS). The origin lies at the intersection of the central ray, and the detection plane: halfway between the mid-planes of the wire chambers [13, 43].

The labels associated with ntuple variables are limited to eight characters, which leads to some fairly cryptic names for quantities stored in the results ntuple. Fortunately, a number of conventions have been followed in assigning the names. These conventions seem to be derived partially from the coding standards set forth in Ref. [56]. They include:

- HMS specific quantities will begin with “hs,” SOS specific quantities with “ss,” physics quantities have no assigned prefix. The Cerenkov counter yields are an exception to this rule, being named “hcer_npe” and “scer_npe.”

³TRANSPORT is a widely used program for doing beam-optics calculations.

- Quantities evaluated at the interaction vertex (i.e. in the target) end with “tar,” those evaluated at the focal plane end with “fp.”
- Positions perpendicular to the central ray are labeled with “x” or “y” in the spectrometers coordinate system. Angles relative the central ray are evaluated in the dispersive (non-dispersive) plane, and labeled “xp” (“yp”).

These rules result in names like *hsxptar* for the angle of the particle relative the central ray in the dispersive plane evaluated at the interaction vertex.

3.1.2 Algorithm

The reconstruction algorithm used for the two spectrometers is essentially identical—differences exist only to allow for the slightly different detector packages and geometry. Event reconstruction proceeds as so:

- Hodoscope ADC and TDC signals are decoded and corrected for gains, offsets, etc. This generates a start time for the DAQ system.
- Drift Chamber, and PID detector signals (if used) are decoded. Track-independent quantities are calculated (these are mostly the raw data from the detectors).
- Single drift-chamber tracks (called stubs) are generated. Full tracks are generated whenever stubs in the two drift chambers match up, and a χ^2 is calculated for this fit. Track dependent quantities (focal plane positions and angles, etc.) are calculated for each track.
- For each track the time-of-flight (TOF) is recalculated using hodoscope hits that lie near the track, and using the proposed track to adjust the hodoscope

timing for signal propagation in the scintillator. The particle velocity β is calculated, and with its momentum used to find its mass.

- Track-dependent particle ID calculations are performed. The shower counter sums the (corrected energy) of any clusters the track points towards. All tracks use the sum of all Cerenkov signals.
- A series of cuts are made on the fitting χ^2 , energy loss, particle velocity, etc. to reject bad tracks. Usually this leaves only one track, and the rare multiple track events are resolved by choosing the track with the best χ^2 .
- The particle's track is propagated backwards through the spectrometer to find positions and momenta at the interaction vertex. During this step, the energy of the particle is corrected for the most probable energy loss.
- Physics quantities are calculated, scalars and histograms are incremented, etc. Counters for the number of expected hits are incremented for detectors judged to lie on the track—these provide an estimate of the efficiency of the detectors.

If coincidence triggers are being analyzed and there are good tracks in both the HMS and the SOS, the coincidence analysis routines are called at this point, allowing additional physics quantities to be calculated, and more output to be written. All of the gory details can be found in Refs. [43, 48].

3.1.3 Controlling Replay

Replay is a big program with *many* options, and a huge number of parameters. While the gross geometry of the spectrometers is hard coded in, almost everything else is expressed as a parameter, and read in at run-time (as opposed

to compile-time). Almost all of this run-time configuration is mediated by the CEBAF Test Package (CTP): a powerful input/output library written for Hall C [57].

The standard Replay distribution comes with a substantial tree of files which contain most of the parameters preset to the correct (or at least nominal) values, and describe where the program should look for input, and what output to generate. A user can work with the program for years, and still find new capabilities buried in all this mess. But the most important input file is the so called “kinematics file”, which is of central concern to the user from the first encounter forward.

The kinematics file is one part in the chain from which Replay chooses some important physics values to use in the analysis. The beam energy, spectrometers angles and excitations, target number,⁴ and particle masses are read first from “run-info” event in the raw data files,⁵ then reset according to the values encoded in the kinematics file, and finally overridden by any parameters the user may have entered on the command line. Clearly, for ease of use, and some protection against typos, it is desirable to collect all the known information into the kinematics file.

3.1.4 Kinematic Offsets

In the previous subsection, we noted that Replay reads the run-info event, and then asserted that it was important to write a kinematics file to override these values. Not only does the run-info event sometimes inaccurately record the

⁴The mapping between target number and composition, thickness, cryocell wall thickness (if present), etc. is read from a different file.

⁵The run-info event is inserted at the beginning of each log file, and contains information on the kinematic conditions of the run both from the DAQ system, and that entered by the operator.

TABLE 3.1: Summary of E94-139 kinematic offsets. The values are presented in the heapcheck format, where angular offsets are in units of milliradians, while energy and momentum offsets are given in increments of 10^{-3} times their nominal values. Note that the angles and momenta here are the spectrometer angles and central momenta, and not necessarily identical to the kinematic quantities defined in Fig. 1.3 [58].

Q^2 (GeV) ²	E_{beam} (GeV)	δE_{beam} ($10^{-3}E_{\text{beam}}$)	$\delta\theta_e$ (mrad)	δp_e ($10^{-3}p_e$)	$\delta\theta_p$ (mrad)	δp_p ($10^{-3}p_p$)
3.3	3.060	-0.4	0.6	1.0	-1.6	-3.4
6.0	4.471	-1.8	0.6	1.2	-0.8	-3.4
8.1	5.565	-0.8	0.6	1.0	-1.0	-0.67

conditions in the hall, but more importantly the feedback systems are only approximately correct. Hydrogen elastic runs provide an opportunity to check these measurements, and calculate corrections to them. The program “heapcheck” works on the ntuples resulting from an analysis of a $H(e, e'p)$ run by replay, and generates a (non-unique [59]) guess at the offsets of the beam energy, spectrometer angles and momenta used in the analysis from their true values [60]. The offsets used for the analysis of e94-139 are shown in Table 3.1.

Quasi-elastic scattering experiments have a subtle advantage in this area, as it is not necessary to move the spectrometers, or change their excitation when changing targets, increasing the usefulness of the heapcheck results. None-the-less, the spectrometers were moved after or before the hydrogen elastics data taking for $Q^2 = 3.3$ and 8.1 GeV² (in order to sweep the Fermi cones, and because the data taking was scheduled in several pieces respectively). After such moves the geometry was returned as close to the original conditions as possible.

3.2 Trigger and Tracking Efficiencies

Two potential sources of error in our yield are inefficiencies of the hardware trigger, and of the tracking algorithm (that part of the analyzer that constructs logical tracks from the raw detector hits). For each of these there exists the possibility of generating false positives as well as false negatives. We need an estimate of how the event yield is affected by all these processes.

3.2.1 Trigger Efficiency

Triggers might be lost (that is an acceptable physics event might not generate a trigger) if two or more planes of hodoscopes fail to register a hit, or if PID detector (Cerenkov detectors and shower counters) register an unexpected state.

The probability of forming a 3 out of 4 (or hadron) trigger (SCIN) from a single good track is the probability that at least three planes generate a signal. Writing the individual plane efficiencies as $P_{[12][xy]}$, we get

$$\begin{aligned} P_{3/4} = & P_1xP_1yP_2xP_2y \\ & +(1 - P_1x)P_1yP_2xP_2y + P_1x(1 - P_1y)P_2xP_2y \\ & +P_1xP_1y(1 - P_2x)P_2y + P_1xP_1yP_2x(1 - P_2y). \end{aligned}$$

The efficiencies of the individual planes can be measured in the analyzer by counting the number of times a plane registers a hit “on” a track. Because multiple scattering can deflect a particle from its “original” path, this quantity is calculated only for tracks that point to within 1 cm of the center of the paddle. Over our entire data set, we found these efficiencies to lie between .91 and 1.000,

TABLE 3.2: Average hodoscope plane efficiencies as measured by tracking for the entire e94-139 data set.

Plane	Measured Efficiency	
	HMS	SOS
S1X	0.9985 ± 0.0003	0.9987 ± 0.00003
S1Y	0.9975 ± 0.0002	0.9938 ± 0.0010
S2X	0.9631 ± 0.0010	0.9405 ± 0.0004
S2Y	0.9408 ± 0.0014	0.921 ± 0.004

and to be very stable in time. This leads to a average overall efficiency of .992 (.987) in the HMS (SOS), and in all cases the efficiency was at least .97 in both spectrometers.

The calculated trigger efficiency for the SOS is believed to be low [43]. Not only does multiple scattering result in larger deflections at the lower momentum used in the electron arm, but the physical paddles in the SOS are narrower. The result is that measured efficiencies in the rear planes are significantly reduced. A crude calculation suggest that in our kinematics, multiple scattering could give expected electron deflections of nearly 4 cm by the time they reach the S2X plane. As the hodoscope paddles are only 10 cm (7.5 cm) wide in plane S2Y (S2X), we would expect to see non-trivial reductions in the measured efficiency of these planes. By contrast, our worst kinematics in the HMS yields an expected deflection of less than 3 cm, on 8 cm paddles. The truth isn't as bad as that, but does suggest that the measurement is not trustworthy. The per-plane efficiencies measured this way can be found in Table 3.2. Following John Arrington's example, we correct only for the HMS efficiency on the assumption that the (small)

over-correction for the rear HMS planes will roughly compensate for the (also small) loss of efficiency in the SOS [43].

The individual efficiencies of the PID detector can be estimated by a similar procedure, and they are generally found to be quite high. However, because our analysis cuts on both PID detectors in the SOS are stricter than the cuts in the trigger hardware, we need not correct for losses to the trigger. See Section 3.4 for corrections arising from the analysis cuts.

False positives might arise from multiple particles in the spectrometer simultaneously, or from other random processes, but it is unlikely that such events will be reconstructed as an acceptable event in the analyzer (mainly due to chi-squared cuts of the tracking algorithm results), and we neglect them.

Because the trigger efficiency is calculated automatically by the analyzer, yields are corrected on a run-by-run basis.

3.2.2 Tracking Efficiency

Replay’s tracking algorithm requires that both wire chambers have a minimum number of hits, that at least one chamber does not exceed a “reasonable” maximum number of hits, and that the track-independent TOF value corresponds to a forward-going particle [43].⁶ Of course, this only applies if the event was recorded in the data stream, which implies that the event generated a trigger in the first place.

Each chamber requires a minimum number of hits to generate a track stub, and solve the left-right ambiguity. If too few hits are required, the algorithm could “find” a track in line noise, or resolve real tracks in the wrong place or with the

⁶Due to the geometry of the spectrometers, cosmic ray events typically traverse the detector stack “backwards.”

wrong direction. A number of algorithms have been tested for this purpose [61], but a simple five out of six algorithm is optimal, and is the method used by e94-139.

Too many signals in a wire chamber require a great deal of processing time, and generate many possible stubs which must be tested. The problem is compounded if both chambers show “many” hits. An analysis of what causes signals to fire *en masse* shows two principle causes: noisy discriminators or amplifier electronics (which can affect 16 channels at once), and events in which an incident electron has scraped the edge of a magnet body and generated a shower [43]. Scraping events almost always cause many hits in both chambers, and electronics noise rarely affected both chamber on a single event, so events are tracked if at least one chamber has fewer than fifteen hits.⁷ Early in the analysis of a run, a time-of-flight value is extracted from the raw hodoscope TDC signals on the assumption that the particle had the expected mass, and was traveling in the \hat{z} direction (see Section 3.1.1). A rough set of cuts on this value restricts the tracking algorithm to events that might plausibly have a good track.

To measure the tracking efficiency, define a series of cuts to select triggers which include at least one physical track. Then count the fraction of triggers satisfying this requirement for which tracks are found. This value is known as the “fiducial efficiency” of the spectrometer for that run. Fiducial efficiencies are calculated automatically and used to correct the physics yields on a run-by-run basis.

The selection of the cuts to use when calculating the fiducial efficiency is more of an art than a science. Before spring 1999, Hall C used a set of cuts first

⁷Dave Gaskell has studied the effect of setting the value to 30, and found it to be helpful when the chambers are experiencing a lot of noise [62].

defined by Derek van Westrum which required a forward going event with four hodoscope triggers in a very limited fiducial region to guarantee that the track had passed through the active area of the wire chambers [61]. In March 1999, John Arrington introduced a new definition which used cuts on the number of hits in the wire chambers, and the relative position of hodoscope hits between the front and back planes, enabling the use of a larger fiducial area on the hodoscopes [63].

3.2.3 Error

Error estimates for these corrections are not easy to obtain. However, as these are small corrections (rarely over 10% for tracking efficiency) we need be concerned only with relatively large errors. The statistical uncertainty of each can be expected to be a Poisson counting error, and may be safely neglected. The systematic uncertainty is more problematic. We have already discussed the difficulties in measuring the trigger efficiency, and the heuristic method used to deal with it.

Studies of the tracking efficiency have found it to be fairly insensitive to the precise choice of cuts to apply [61, 62], allowing us a certain degree of optimism about its correctness.

3.3 Dead Time

In a perfect world, events could be read, and the individual detector elements made ready to detect another event instantaneously. In the real world, the data acquisition electronics and computers (Section 2.7) take a finite amount of time to process each event. Any further events which occur during that time will not be recorded. Notationally, the system is “dead” for that period.

Dead times in Hall C are lumped into two categories: computer dead time arising from the trigger supervisor busy signal, and electronic dead time which covers the complex behaviors of the early trigger electronics. Electronic dead time has a short characteristic period (≈ 50 ns), but is partially paralyzable⁸, and is associated with *every* event in the detectors, be it interesting physics, a cosmic ray, a random particle, or detector noise. The trigger supervisor is busy for a longer period (around $600 \mu\text{s}$ [45]) but only goes to work on events that are to be written to the data stream.

3.3.1 Computer Dead Time

The trigger supervisor busy signal prevents the 8LM from forming triggers from pretriggers (see Table 2.3). Since all pretriggers are recorded as scaler events in the data stream, we know exactly how many events are lost at this level. We write the fractional live time L associated with the trigger supervisor busy as one minus the fractional dead time D :

$$L_{\text{Computer}} = 1 - D_{\text{Computer}} = \frac{N_{\text{trigger}}}{N_{\text{pretrigger}}} \quad (3.1)$$

The uncertainty associated with this computation is strictly statistical.

3.3.2 Electronic Dead Time

No simple mechanism exists to measure the electronic dead time. Indeed this correction arises from physical response of individual detectors, the limits of

⁸A system is said to be paralyzable or extensible if hits occurring during the dead interval can extend that interval. That is, if the system does not become active again until some characteristic time τ passes without any hits. By contrast, a non-paralyzable system becomes live after time τ has passed since the triggering event, regardless of any hits that may have occurred in the mean time. The two types of system require different mathematical treatment [64].

their discriminators, and the logic gate widths in the trigger electronics. Some of these sources are paralyzable, and some are not. However, the characteristic dead time, τ , of all of these devices is short enough that at all reasonable data rates, R , it holds that $R\tau \ll 1$, and to first order both an extensible and a non-extensible treatment yield the same (trivial) approximation to live time [45]:

$$L_{\text{Electronic}} = 1 - R\tau. \quad (3.2)$$

We then take advantage of the linear nature of Eq. (3.2). The pretrigger generated by the logic is fanned out into four signals with varying gate width (30, 60, 90, and 120 ns⁹). These generate separate scalers (labeled EL30, EL60, EL90, and EL120) which can be used to compute the dead time correction by linear extrapolation to zero gate width. That is the true number of counts should be given by

$$N_{\text{true}} = N_{\text{measured}} + \frac{N_{\text{EL120}} - N_{\text{EL60}}}{60 \text{ ns}} W_{\text{PRETRIG}}, \quad (3.3)$$

where $W_{\text{PRETRIG}} = 50 \text{ ns}$ is the actual width of the pretrigger gate.

$$L_{\text{Electronic}} = \frac{N_{\text{measured}}}{N_{\text{true}}} = \left(N_{\text{EL120}} - N_{\text{EL60}} \right) \frac{50 \text{ ns}}{60 \text{ ns}}. \quad (3.4)$$

Again the uncertainty is statistical.

⁹All of these are actually at least as long as the actual gate width of PRETRIG which is the 50 ns gate of the hodoscope discriminators. The ‘30’ notation is historical [45].

3.3.3 Dead Time Corrections

All yields are corrected for dead times on a run-by-run basis by dividing them by the fractional live times found in Eqs. (3.1) and (3.4).

3.4 Particle Identification

Particle identification (PID) in e94-139 turns out to be fairly easy, and high π^- to e^- discrimination ratios are easily obtained.

Because the accidental coincidence rate drops rapidly with increasing Q^2 [1], it was judged safe to neglect particle identification in the HMS. In the SOS, PID was needed to separate the (interesting) electrons from a fairly large pion background. Both the Cerenkov detector and the lead-glass calorimeter are employed for this purpose.

The trigger makes an initial selection of events during data taking, requiring one of several conservative combinations of detector hits to generate a trigger. See Section 2.7.1.1 for a full explanation. Then, during the analysis of the data runs, PID cuts are applied requiring that:

$$\text{Total number of Cerenkov photons} > 2$$

$$\text{Fraction of energy deposited in the calorimeter} > 0.6.$$

A series of studies conducted by Ioana Niculescu suggests that each of these cuts provides better than 99% accurate discrimination, leading to a 10^4 suppression of pion events in the SOS [65].

3.5 Dependence of Cryo-target Density on Beam Current

The effective “thickness” of cryo-liquid targets (hydrogen and deuterium in e94-139) depends on the density of the fluid, which depends both on the bulk temperature, and on the presence of any local boiling.

The beam can transfer quite significant quantities of heat to relatively small regions of cryo-fluid, and while the overall heating is quite well compensated by a temperature feedback mechanism, it is not possible to eliminate local boiling. The remedy is to measure the effect as a function of beam current (i.e. to take a so-called luminosity scan), and correct the observed yield.

One naively expects the density of the target to drop linearly with increasing beam current, and this expectation agrees quite well with historical Hall C measurements. One further expects the size of the effect to have little dependence on beam energy, and to vary roughly inversely with the area swept by the fast raster (see Section 2.3.4).

The dependence of cryo-target density on beam current in Hall C has a history of being difficult to pin down. One can work from the yield of raw trigger signals, tracks found by the analyzer, or physics events generated. Using data from further along the analysis stream seems preferable because it more closely resembles the actual data, however doing so sacrifices statistics in a measurement that often has a large uncertainty associated with counting and fitting error.

As described in Section 2.3.4 multiple raster configurations were available and used over the course of the experiment. Multiple luminosity scans were taken, giving good information on which to base a current dependent correction. The single value $(-2.0 \pm 0.4)\%$ per $60 \mu\text{A}$ was selected for actual use.

TABLE 3.3: Summary of cryo-target density dependence measurements taken during the experimental run. Note that beam does not boil carbon, and that scan can be used to validate the method. The results for all the May scans are taken from analyzer track yield in the SOS, the July runs were analyzed from single-arm physics events.

Scan Date	Target	Raster size (mm)	change per 60 μ A (%)	Notes
May 8	^1H	1.0	-6.3 ± 1.1	63 Hz breathing, scalers
May 16	^2H	1.0	-2.0 ± 0.3	63 Hz breathing, scalers
May 19	^1H	1.0	-3.9 ± 0.7	47(!!) Hz breathing, scalers
May 19	^1H	1.0	-4.4 ± 0.8	100 Hz breathing, scalers
May 19	C	1.0	$+0.7 \pm 0.4$	100 Hz breathing, scalers
May 23	^2H	1.0	-4.9 ± 0.3	63 Hz breathing, scalers
July 15	^1H	2.5x1.3	-1.4 ± 0.1	HMS, Cerenkov cut, no ytar cut
July 15	^1H	2.5x1.3	-1.5 ± 1.3	SOS, ytar cut, no PID
July 15	^1H	1.5	-2.0 ± 0.2	HMS, Cerenkov cut, no ytar cut
July 15	^1H	1.5	$+0.2 \pm 2.6$	SOS, ytar cut, no PID

3.6 Proton Absorption

While the goal of e94-139 is to measure changes in the probability that the recoiling proton interacts before exiting the original nucleus, there remains a chance that it will be removed from the acceptance after leaving the original nucleus, but before generating a trigger in the detector stack. The cause of this may be multiple scattering, a single hard scattering event, or an inelastic nuclear interaction. We call this phenomena “proton absorption,” and expect it to be a sizable correction.

3.6.1 Basic Measurement

We can measure the proton absorption in hydrogen elastic scattering— $(e, e'p)$. The simple initial state means that every electron seen in elastic kinematics should be paired with a proton in the opposite detector arm. Where this is not true a proton has been lost. We count the number of times we generate a qualifying electron arm trigger *without* generating a coincidence trigger, and divide by the total number of electron arm triggers:

$$\text{Absorption} = \frac{N^{\text{electron arm only}}}{N^{\text{electron arm, or coincidence}}}. \quad (3.5)$$

3.6.2 Previous Work

Several previous measurements of the proton absorption in the Hall C spectrometers exist. Derek van Westrum analyzed the proton absorption for the earlier nuclear transparency experiment (e93-013) in Hall C, and found the absorption in the HMS to be $A_p^{e91013} = (5.5 \pm 2)\%$ [66]. Chris Armstrong also studied the problem and got a result of $A_p^{e94014} = (2.8 \pm 1.2)\%$ [48].

The disagreement of these results suggests that the measurement may be more difficult than it appears.

3.6.3 Issues and Definitions

The proton absorption calculation is simple in theory, but the realities of the experimental process add some complexity. We need to deal with background subtraction, trigger prescales, the way the data are written to ntuples, and the various detector inefficiencies.

3.6.3.1 What’s in the Ntuples?

Replay writes two ntuples containing information pertinent to the electron arm. In Replay’s notation, these are referred to as “singles” and “coincidence,” but the “singles” ntuple actually contains data for all events which generate a trigger in the electron arm. (i.e. more or less the quantity in the denominator of Eq. (3.5)). For clarity, I will use the term “inclusive” to refer to this data, and the term “singles” to mean events which generated a trigger *only* in the electron arm (i.e. the quantity in the numerator of Eq. (3.5)). To get the singles yield from the inclusive yield, we subtract.

3.6.3.2 Prescales

The trigger is constructed with separate prescalers for each arm, and for coincidences. In e94-139, we always ran with the coincidence prescale at 1, but the electron arm prescale often took other values. We use P for the prescale value of the electron arm. Under these conditions, an event gets written to the tape, and then into the inclusive ntuple if it generates a coincidence trigger, *and* every P^{th} time there is a singles trigger in the SOS. With this in mind, we write the number of singles triggers as $N^{\text{singles}} = N^{\text{inclusive}} - N^{\text{coincidence}}$, and the total number of singles events as PN^{singles} (plus some number fewer than P).

3.6.3.3 Efficiencies

In Hall C we define five types of detector efficiencies corrections: electronic dead times in each arm, fiducial efficiencies in each arm, and computer dead time. Typical electronic dead times are insignificant (less than .05%). Of the remaining three, only the proton arm fiducial efficiency affects one type of trigger, and

not the other. We will find that our final expression for the proton absorption (Eq. (3.7)) has the form of a ratio of terms linear in assorted yields, so we cancel all the common efficiencies. The only correction that remains is for the HMS fiducial efficiency. We define the efficiency corrected coincidence yield as:

$$Y'^{\text{coin}} = \frac{Y^{\text{coin}}}{E_{\text{proton-arm fiducial}}}. \quad (3.6)$$

3.6.3.4 Definitions

Now we try to rewrite Eq. (3.5) in terms of experimental yields. Let the symbol $Y_{\text{target}}^{\text{data}}$ mean the yield, after cuts, of a particular class of data, on a particular target. Data may be “inc” or “coin” meaning inclusive or coincidence respectively, and target may be “LH2” or “dummy.” All dummy yields are normalized to account for different integrated luminosities, and the extra thickness of the dummy walls.

We also define separate prescale factors P_{LH2} and P_{dummy} . Using the efficiency correction convention of Eq. (3.6), we write:

$$\begin{aligned} Y_{\text{target}}^{\text{singles}} &= Y_{\text{target}}^{\text{inc}} - Y_{\text{target}}^{\text{coin}} \\ Y_{\text{target}}^{\text{total}} &= Y_{\text{target}}^{\text{singles}} P_{\text{target}} + Y_{\text{target}}'^{\text{coin}}, \end{aligned}$$

where the “singles” yield is the number of singles *triggers* (so the number of real singles events is $Y_{\text{target}}^{\text{singles}} P_{\text{target}}$), and the “total” yield is the total number of *events*. For yields that have had the background events removed¹⁰, we drop the

¹⁰Precisely how this should be done is the topic of Section 3.6.4

target symbol, so we can write the proton absorption as:

$$A_P = \frac{Y^{\text{total}} - Y^{\text{coin}}}{Y^{\text{total}}} \quad (3.7)$$

3.6.4 Background

Our data set contains some data from events that originated in the cell walls. Good cuts can reduce the number of these that contribute, but we would like to be able to remove them altogether.

Removal of the background contribution turns out to be fraught with difficulty. Two methods present themselves: subtracting the background as measured from the dummy cell, and placing strict y_{target} cuts to exclude the contributions of the the walls.¹¹

3.6.4.1 Dummy subtraction

Background subtraction should be straight forward: normalize the background yield for the total luminosity of the runs and the extra thickness of the dummy target, then subtract. We define the normalization factor N_{dummy} , to allow for the different total luminosity, and the additional thickness of the dummy cell. Then we write

$$\begin{aligned} Y^{\text{inc}} &= Y_{\text{LH2}}^{\text{inc}} - N_{\text{dummy}} Y_{\text{dummy}}^{\text{inc}} \\ Y^{\text{coin}} &= Y_{\text{LH2}}^{\text{coin}} - N_{\text{dummy}} Y_{\text{dummy}}^{\text{coin}}. \end{aligned}$$

¹¹We write y_{target} for the y position (in the spectrometer coordinate system, see Section 3.1.1) of the interaction vertex as determined by Replay. Cuts on y_{target} can affect the SOS acceptance, but in this case, it shouldn't matter—what we're measuring is the fraction of protons *in the HMS* that are lost after leaving the nucleus.

which lets us write

$$\begin{aligned}
A_P &= \frac{Y^{\text{total}} - Y^{\text{coin}}}{Y^{\text{total}}} \\
&= \frac{(Y_{\text{LH2}}^{\text{total}} - Y_{\text{dummy}}^{\text{total}}) - (Y_{\text{LH2}}^{\text{coin}} - Y_{\text{dummy}}^{\text{coin}})}{(Y_{\text{LH2}}^{\text{total}} - Y_{\text{dummy}}^{\text{total}})} \\
&= \frac{Y_{\text{LH2}}^{\text{singles}} P_{\text{LH2}} - Y_{\text{dummy}}^{\text{singles}} P_{\text{dummy}}}{(Y_{\text{LH2}}^{\text{singles}} P_{\text{LH2}} - Y_{\text{dummy}}^{\text{singles}} P_{\text{dummy}}) + (Y_{\text{LH2}}^{\text{coin}} - Y_{\text{dummy}}^{\text{coin}})}.
\end{aligned}$$

If both prescale factors are one, this simplifies to

$$\begin{aligned}
A_P &= \frac{(Y_{\text{LH2}}^{\text{inc}} - Y_{\text{dummy}}^{\text{inc}}) - (Y_{\text{LH2}}^{\text{coin}} - Y_{\text{dummy}}^{\text{coin}})}{(Y_{\text{LH2}}^{\text{inc}} - Y_{\text{dummy}}^{\text{inc}}) - (Y_{\text{LH2}}^{\text{coin}} - Y_{\text{dummy}}^{\text{coin}}) + (Y_{\text{LH2}}^{\text{coin}} - Y_{\text{dummy}}^{\text{coin}})} \\
&= \frac{(Y_{\text{LH2}}^{\text{inc}} - Y_{\text{dummy}}^{\text{inc}}) - (Y_{\text{LH2}}^{\text{coin}} - Y_{\text{dummy}}^{\text{coin}})}{(Y_{\text{LH2}}^{\text{inc}} - Y_{\text{dummy}}^{\text{inc}}) - (Y_{\text{LH2}}^{\text{coin}}(1 - \frac{1}{E}) - Y_{\text{dummy}}^{\text{coin}}(1 - \frac{1}{E}))}.
\end{aligned}$$

3.6.4.2 Background Mismatch

If we attempt to perform the subtraction outlined above, we find a problem: in the $Q^2 = 3.3 \text{ GeV}^2$ kinematics (where we have the best statistics), the walls of the target cells lie very near the edges of the SOS acceptance. Nominally the dummy and the cryo-cell are in the same place, but in reality their positions differ by about 2.5 millimeters. Consequently the nominal background normalization is questionable. See Fig. 3.1.

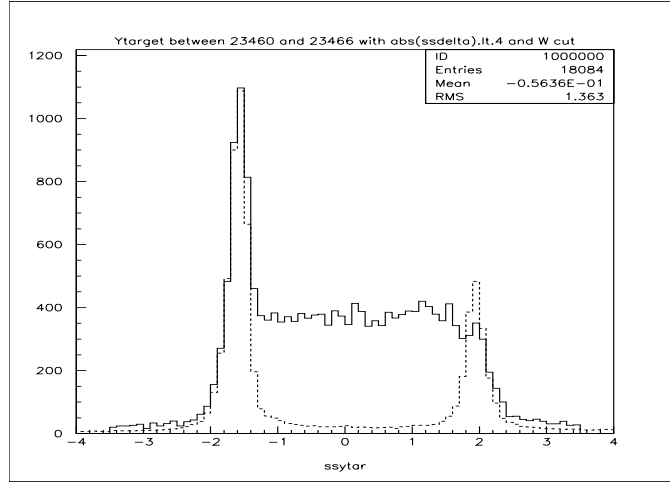


FIG. 3.1: Comparison of the y'_{target} spectra between liquid hydrogen and the dummy target for $Q^2 = 3.3 \text{ GeV}^2$. (Solid line is LH2, dashed is dummy) The dummy has been scaled by the nominal factor.

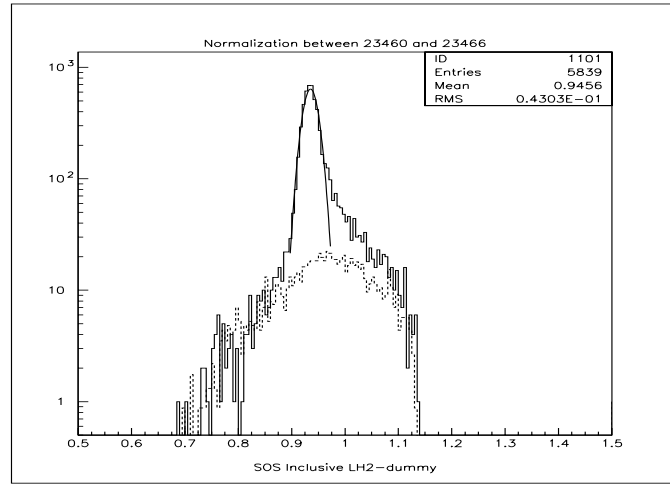


FIG. 3.2: Direct comparison of invariant mass (W) spectra between the LH2 (solid line) and dummy (dashed) targets.

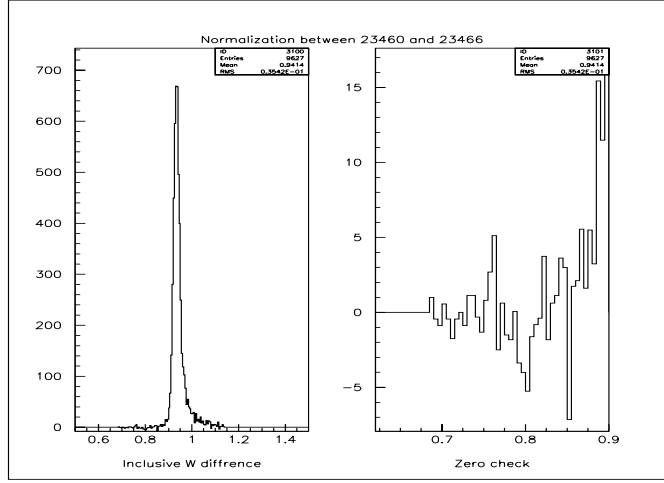


FIG. 3.3: Residual invariant mass (W) spectra after dummy subtraction with $N_{\text{dummy}} = 0.393$.

To deal with this, we compare the invariant mass, W , spectra of the two runs (see Fig. 3.2), and choose the normalization constant such that the super-elastic¹² spectra match (Fig. 3.3).

This method suffers from additional statistical errors from the choice of what region in W to integrate when matching the super-elastic spectra, and from the limited number of counts in that region (non-independent, but not completely linked quantities), and from an unknown systematic error arising from the different contributions of the front and back windows between the two targets.

¹²By super-elastic we mean events with an invariant mass less than the proton mass. Because such events are kinematically disallowed, we believe that any we appear to receive are random triggers. These should be largely independent of the experimental conditions, though they should vary with the square of the scaler trigger rate.

Doing the work results in:

$$\begin{aligned} N_{\text{Dummy}} &= .393 \pm 0.60 \\ A_p^{\text{BG Normalization}} &= (3.5 \pm 1.5(\text{stat}) \pm 0.8(\text{sys}))\%. \end{aligned}$$

This result for the proton absorption agrees with the previous work of Chris Armstrong, but disagrees with previous work by Derek van Westrum.

3.6.4.3 Pure LH2

An alternative method is to put a strict y_{target} cut on the data so that we examine a region with essentially no background to subtract. Examining Fig. 3.1 we see that a cut of $|y_{\text{target}}| < 1.25$ cm or tighter should do the trick.

This method sacrifices some statistics, and introduces a substantial systematic error when correcting extended targets because the SOS acceptance is strongly y_{target} dependent.

The results of this work are:

$$A_p^{\text{Pure LH2}} = (6.4 \pm 2.2)\%$$

This result agrees with van Westrum’s work, and disagrees with Armstrong’s.

3.6.5 Theoretical Calculation

Given the ambiguous results of past and current attempts to measure the proton absorption, we try to model the problem. Perhaps some insight can be found in theory. Further, we will need a model of the proton absorption to correct for the target dependency of this quantity—the proton can see a substantial

quantity of absorption in the target itself, and the different targets have different thicknesses. This can be a substantial correction for the A dependent analysis, and a smaller one for the Q^2 dependent analysis.

3.6.5.1 A Simple Model

The simplest way to calculate the expected loss is to add up the number of radiation lengths of material between the target and the point at which the proton generates a trigger, and write the transmittance, $T_p = 1 - A_p$, as:

$$T_p = \exp\left(-\sum_i \frac{X_i}{\lambda_i}\right).$$

Here the X_i 's are the mass-depths of the materials on the proton's flight path, the λ_i 's are the radiation lengths of those materials, and i runs over enough of the detector to guarantee a trigger.

3.6.5.2 What is λ ?

The total interaction cross-section of protons in an arbitrary material may be written in terms of elastic and inelastic parts. The Particle Data Book [67] tabulates the radiation length in terms of the total (physical) radiation length, λ_T , which is based on the whole cross-section, and the “inelastic” radiation length, λ_I , which neglects the elastic cross-section. The radiation length that we want lies somewhere between these, because the elastic scattering cross-section is strongly peaked in the forward direction and does not always remove the proton from the acceptance.

A simple multiple-scattering calculation suggests that typical elastic interactions deflect the proton through angles that are smaller than our angular cuts. For the rest of this discussion, we neglect the elastic cross-section, taking $\lambda = \lambda_I$.

3.6.5.3 How Far to Go?

We need to follow the proton far enough to guarantee that a trigger will be generated. The simplest approach is to require the proton to penetrate enough of the third scintillator plane to generate a pulse [66].

However, the proton has a lot of momentum: any interaction it undergoes is likely to result in some forward-going charged hadron. If the interaction takes place after the proton enters the detector stack, a trigger might still be generated. This provides an argument for setting the limit earlier in the detector stack.

To understand this question exactly, we require a complete Monte Carlo of the detector, which is not currently available. For now, this is another uncertainty in our model.

3.6.5.4 Results

Using the simplest set of assumptions (with the proton traversing one forth of the third horscope plane), we get a predicted proton absorption of:

$$A_p^{\text{HMS calculated}} = 1 - e^{-.04967} = 4.8\%$$

See Table 3.4 for the masses and radiations lengths of materials in the HMS. This agrees reasonable well with our pure LH2 measurement, and with the e93-013 measurement, but with two parameters (the correct choice of λ in terms of

TABLE 3.4: (Effective) Thickness of materials in HMS through the rear hodoscopes.

Absorber	Density (g/cm^3)	Thickness (cm)	λ (g/cm^2)	X (g/cm^2)	X/λ (10^{-3})	Cumulative X/λ (10^{-3})
2.49cm LH (after scattering)	0.0723	2.49	50.8	0.1800	3.543	3.543
5 mil Al target window	2.70	0.0127	106.4	0.0343	0.322	3.865
16 mil Al chamber window	2.70	0.0406	106.4	0.1096	1.030	4.895
Air	0.00121	~ 15	90.0	0.0182	0.202	5.097
Kevlar	0.74	0.0381	85.2	0.0282	0.331	5.428
Mylar	1.39	0.0127	85.7	0.0177	0.2106	5.634
Kevlar	0.74	0.0381	85.2	0.0282	0.331	5.965
Mylar	1.39	0.0127	85.7	0.0177	0.206	6.171
Air (exit pipe through S2)	0.00121	~ 35	90.0	0.0424	0.471	6.642
2mil Mylar (enter/exit)	1.39	0.0051	85.7	0.0071	0.083	6.725
Sense Wires 25 μ m W, 6 planes	19.3	0.000038	185	0.00073	0.004	6.729
Field Wires 150 μ m Al/Au (99/1)	2.70	0.0068	89.1	0.0184	0.206	6.935
18 planes Ar/Ethane (50/50 weight)	0.00154	8.3	103.1	0.0128	0.124	7.059
2mil Mylar (enter/exit)	1.39	0.0051	85.7	0.0071	0.083	7.142
Sense Wires 25 μ m W, 6 planes	19.3	0.000038	185	0.00073	0.004	7.146
Field Wires 150 μ m Cu/Be (50/50)	5.40	0.0068	105.0	0.0368	0.350	7.496
18 planes Ar/Ethane (50/50 weight)	0.00154	8.3	103.1	0.0128	0.124	7.610
Poltysty. (1.067 overlap)	1.03	2(1.067)	82.0	2.198	26.805	34.415
Čerenkov windows (40mil Al entrance/exit)	2.70	2(0.102)	106.4	2(0.275)	5.169	39.584
Čerenkov gas N ₂	0.00125	150	87.8	.1875	2.136	41.720
Rohacell Mirror support	~ 0.05	~ 1.8	~ 80	0.09	0.112	39.696
Mirror SiO ₂	2.20	0.3	99.2	0.66	6.653	46.349
Poltysty. (1.067 overlap)	1.03	2(1.067)	82.0	2.198	26.805	73.154

TABLE 3.5: Individual target proton absorption corrections.

Target	Q^2 (GeV) ²	X (g/cm ²)	λ (Rad. length)	$\frac{X}{\lambda}$ (10 ⁻³)	$1 - \exp(-\frac{X}{\lambda})$ (%)
LH2	3.3	0.180	50.8	3.54	.35
	6.0	0.169		3.33	.33
	8.0	0.168		3.30	.33
LD2	3.3	0.180	54.7	7.50	.75
	6.0	0.169		7.06	.70
	8.0	0.168		6.98	.70
Fe(1)	3.3	0.920	131.9	6.97	.69
	6.0	1.029		7.86	.78
	8.0	0.995		6.57	.65
C(5)	3.3	0.920	86.3	15.87	1.57
	6.0	1.029		17.74	1.76
	8.0	0.995		17.17	1.70

λ_I and λ_T and the penetration required of the proton), we can also match Chris Armstrong's results with reasonable assumptions.

3.6.6 Target Corrections

The measured proton absorptions apply to the LH2 target in the geometry for $Q^2 = 3.3$ GeV² kinematics. Each target and geometry will give a different contribution which should be corrected for (because of differing target thickness, and differing relative angles between the target and the HMS). Table 3.5 gives the correction on the assumption that $\lambda = \lambda_I$. All the measured and theoretical values given up to this point in the text include the LH2 target at $Q^2 = 3.3$ GeV².

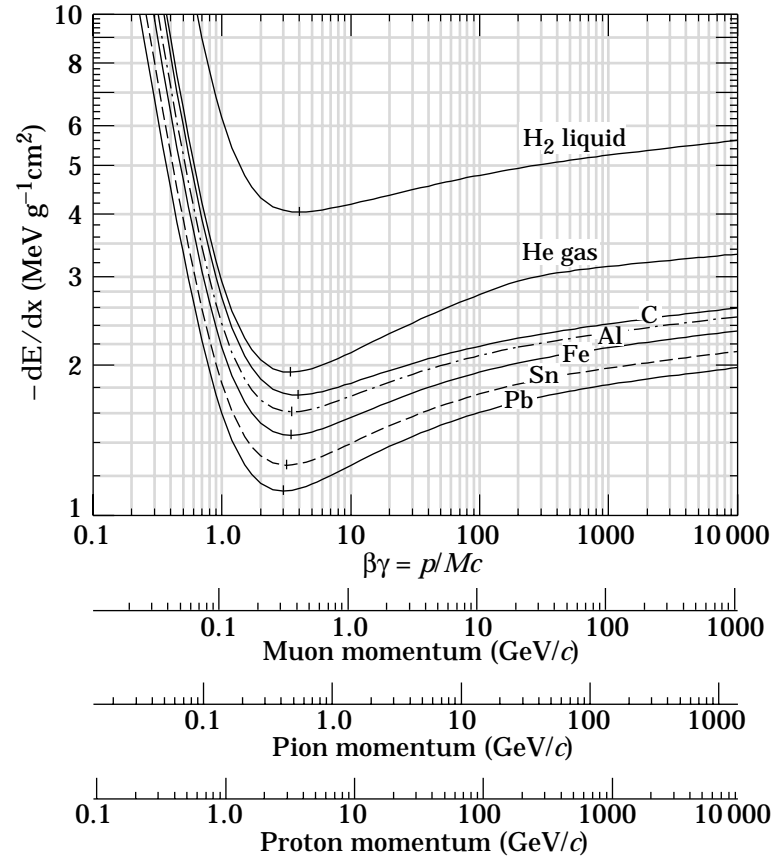


FIG. 3.4: Energy loss by massive particles in various materials. Figure from the Particle Data Book [67].

3.6.7 Momentum Dependence

We expect the proton absorption to show very little dependence on the kinematics being measured. The proton momentum took values between 2.52 and 5.15 GeV. Looking at Fig. 3.4, we see that all these momenta lie near the minimum ionizing peak for protons in all materials. Consequently the proton interaction cross-section should have little dependence on the proton momenta.

This assumption has been tested with the Hall C equipment in the past [48, 66], and has been found to be reliable. We cannot make a definitive test with our data because the SOS singles were prescaled when running hydrogen elastic at $Q^2 = 6.0$ and 8.0 GeV^2

We choose to use a value of $A_P = .0465$ for the nominal proton absorption in the HMS. The target dependent values listed in Table 3.5 should be added to this value.

Errors in choosing the proton absorption associated with the HMS would have little effect on the transparency analysis (because all data points will be multiplied by the same factor), though it will effect our normalization relative the rest of the world data set. An error in understanding the target dependent effects (i.e. the corrections listed in Table 3.5) would cause a small point to point variation in Q^2 , and a slightly larger point to point variation in A . This effect contributes directly to the normalization of the extracted spectral functions.

4. MONTE CARLO

The analysis of the data requires a comparison with theory. It is a fact of life that experimental results depend on many experiment-specific details, while theorists prefer to put their work in general terms—not worrying about the details of a particular apparatus or measurement. We use a Monte Carlo simulation to get the theoretical results and data to a common point for comparison.

4.1 SIMC—The Hall C Monte Carlo

The Hall C Monte Carlo is called SIMC, and is a descendant of the NE-18 simulation called SIMULATE. It is written in VAX Fortran, and is intended to provide a highly realistic simulation of the underlying physical processes, and the transport through the detector. Corrections are provided for Coulomb effects, internal- and external-Bremsstrahlung, multiple scattering, and ionization energy losses.

The 1999 version of SIMC is capable of simulating a variety of physical processes. I will discuss only elastic and quasi-elastic proton scattering. For a further discussion of the capabilities of the program see Refs. [68, 69].

I will provide a brief summary of the method used, then discuss some important topics in detail.

4.1.1 Summary

SIMC generates an event as follows:

- Generate the incident electron 4-vector \mathbf{k} from distributions which match those of the real beam.
- Generate outgoing electron and proton 4-vectors \mathbf{k}' and \mathbf{p}' respectively, from flat distributions covering a solid angle somewhat larger than the requested limits.¹
- Calculate the missing energy and momentum, E_m^v and \vec{p}_m^v , at the fundamental vertex (before the radiative corrections, at the level of the PWIA).
- Apply radiative corrections (if requested) to \mathbf{k} , \mathbf{k}' , and \mathbf{p}' ; calculate the weight, W_{rad} associated with these corrections; and correct E_m^v and \vec{p}_m^v .
- Transport the scattered particles forward through the spectrometers. Multiple scattering and ionization are taken into account. Find the focal plane quantities.
- Transport the focal plane quantities back to the vertex in the same way Replay does. This yields the target quantities that go into the ntuple.
- Assign the event the weight:

$$E' p' \sigma_{ep}(E_m^v, \vec{p}_m^v) S(E_m^v, \vec{p}_m^v) W_{\text{rad}}.$$

¹This allows for radiation and multiple scattering effects, and wastes a very modest amount of computation on events lying outside the spectrometer's acceptance.

Where $S(E_m^v, \vec{p}_m^v)$ represents the model spectral function. Events which generate a non-physical vertex, or fall outside the acceptance are assigned a weight of zero.

In addition to this procedure, all events are weighted by a luminosity and phase-space factor,

$$\frac{\mathcal{L} \Delta E_p \Delta \Omega_p \Delta E_e \Delta \Omega_e}{N_{\text{gen}}},$$

to normalize the Monte Carlo output for direct comparison with the data. (The calculation of the necessary Jacobian is buried in this weight.)

For elastic scattering, this procedure is varied: only the electron four vectors are generated—the proton kinematics are obtained by conservation of momentum—and the model spectral function weight is not applied.

4.1.2 Running SIMC

The user provides SIMC with an input text file (in CTP format) describing the conditions to be simulated, and what corrections to apply. In some cases a so-called theory file describing a model for the spectral function (quasi-elastic) or momentum distribution (meson production) of the target nucleus may be required. Output includes an event by event summary in the form of a CERNLIB ntuple, and a plain text file detailing the run conditions and results (commonly called a history file). The detail are found in Ref. [69].

To obtain results from SIMC that are properly normalized for the simulated charge and number of events, it necessary to weight each event by the ntuple entry “weight,” and a global phase space and luminosity factor obtained from the history file: $\text{normfac}/N_{\text{gen}}$ [69]. That is to say the yield in some experimental

volume is found by

$$N_{\text{region}}^{\text{MC}} = \frac{\text{normfac}}{N_{\text{gen}}} \sum_{\text{qualifying events}} \text{weight}. \quad (4.1)$$

4.2 Model Spectral Functions

In order to model interactions on non-trivial nuclei, SIMC requires as input a description of the structure of the nucleus to be modeled.

The model spectral functions used in this analysis were inherited from NE18 by way of e91-013, and were generated by the program DWEOPY [3, 14] which solves the Schrödinger equation for nucleon wave functions in the independent particle shell model (IPSM).

4.2.1 Optical Model

The spectral functions generated by DWEOPY are based on the independent particle shell model (IPSM) in which the nucleus is described as A independent nucleons occupying well defined shells and interacting only by Pauli exclusion and a mean potential. The spectral function is also assumed to factor into a sum over the shells of the product of a momentum distribution, $\rho(\vec{p}_m)$, and an energy distribution, $L(E_m)$:

$$S(E_m, p_m) = \sum_n O_n \rho_n(p_m) \mathcal{L}_n(E_m), \quad (4.2)$$

where O_n is an occupation number for shell n .² DWEOPY then solved the Schrödinger equation for $\rho(\vec{p}_m)$ in an optical model potential. The energy de-

²I have dropped the spin and orbital angular momentum indices under the assumption of spherical symmetry arising from the use of an unpolarized target.

pendence $\mathcal{L}(E_m)$ was assumed to have a Lorentzian form (i.e. that of an isolated resonance):

$$\mathcal{L}(E) = \frac{1}{\pi} \frac{\Gamma/2}{(E - E_B)^2 + (\Gamma/2)^2}. \quad (4.3)$$

For deuterium, the Bonn potential [70] was used as input to the optical model. For heavier nuclei, a sum of Coulomb and Woods-Saxon potentials:

$$V = -V_o f(r, R_0, a_0) + V_{so} \left(\frac{\hbar}{m_\pi c} \right)^2 \frac{2}{r} \frac{df}{dr} \mathbf{l} \cdot \mathbf{r} + V_C(r), \quad (4.4)$$

was employed. With the Woods-Saxon potential written as

$$f(r, R, a) = \frac{1}{1 + e^{\frac{r-R}{a}}}, \quad (4.5)$$

and the the Coulomb potential that of a uniform, spherical, charge distribution of radius $R_C \equiv r_C A^{1/3}$:

$$V_C(r) = -\frac{(Z-1)e^2}{4\pi\epsilon_0 R_C} \left(\frac{3}{2} - \frac{r^2}{2R_C^2} \right). \quad (4.6)$$

These and other considerations leave the model with a considerable number of free parameters which were fit to experimental data (for light nuclei and outlying shells on heavier nuclei), and to the results of a Hartree-Fock calculation (for the lowest lying shells in iron). See Ref. [14] for complete details.

One additional concern is the effect of short-range correlations on the spectral function. It is known that nucleon-nucleon correlation effects (neglected by construction in the IPSM) have a significant effect on the distribution of nucleons in the nucleus by pushing some of the spectral density to higher energy and momentum than is calculated in the pure IPSM. To a good approximation

this effect leads to a uniform suppression of the spectral strength at all momenta less than or comparable to the Fermi momentum, without significant changes in the shape of the spectral function. So the model spectral functions were multiplied by a so-called spectroscopic factor chosen individually for each nucleus [14, 71]. It is important to note that this correction is not only model dependent, but also dependent on the volume of phase space over which it is evaluated. See Section 4.4.5 for further discussion.

4.2.2 Theory file

The results of the modeling and fitting described in this section are tabulated in plain-text, theory files. These file have a simple, unannotated format. They are laid out thus:³

Line 1: Consists of three values: the number n of shells to be simulated (an integer), the overall spectroscopic factor and the Fermi energy.

Next n lines: Each represents one nuclear (sub)shell. Four values are given: the occupation number of the shell (including the spin degeneracy), the binding energy of the shell (actually the Lorentzian resonance peak in missing energy), the uncertainty (Lorentzian width parameter, Γ) in that quantity, and a normalizing factor for the spectral density of *this* shell.

Rest of the file: What follows are groups of lines describing each shell in sequence. The lines consist of a momentum and a spectral density. The momenta are sorted so that the lowest (most negative) momenta of the first

³The meaning and interpretation of this file is varied somewhat for deuterium because the binding energy is fixed.

```

2 0.56 15.96
2 38.1 20 0.960
4 16.2 5.0 0.972
-490.0000 0.1186195E-12
-480.0000 0.1340165E-12
-470.0000 0.1416847E-12
:
480.0000 0.1340165E-12
490.0000 0.1186195E-12
-490.0000 0.8374227E-13
-480.0000 0.5532198E-13
:
470.0000 0.2144142E-13
480.0000 0.5532198E-13
490.0000 0.8374227E-13

```

FIG. 4.1: An abbreviated view of the carbon theory file (c12.theory) used in this analysis.

shell comes first, and the rest of the momenta bins for that shell follow in ascending order. Then the next shell is similarly arranged, then the next...

The spectral density, $\rho_i(p_m)$, is computed by linear interpolation on the table in the theory file.

Figure 4.1 is a short view of a sample theory file.

4.3 Radiative Corrections

SIMC uses a Plane Wave Impulse Approximation (see Section 1.6.1) to model physical interaction at the vertex. This is conceptually simple, and easy to calculate, but produces results very unlike the real data. Applying certain radia-

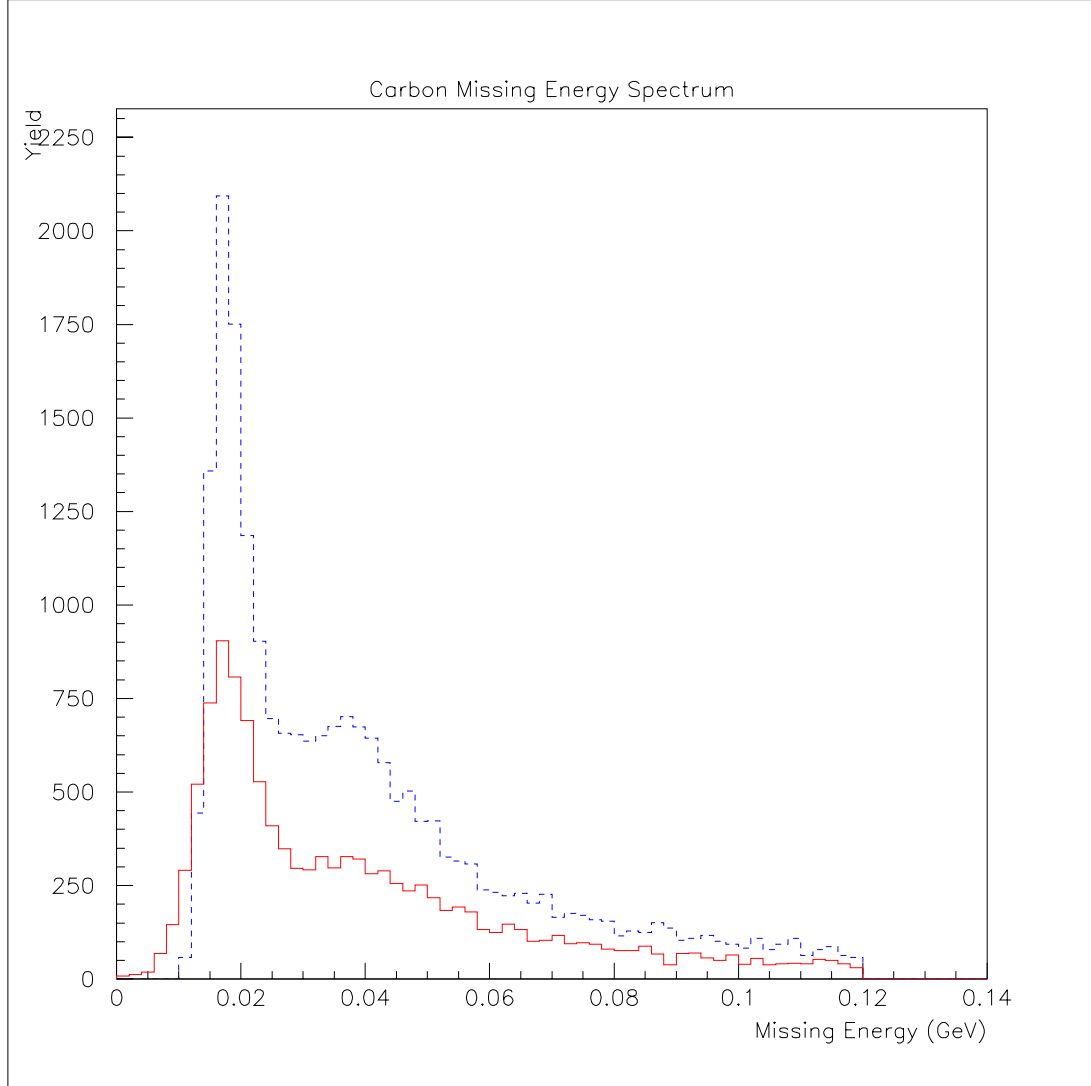


FIG. 4.2: A comparison between data (solid line) and Monte Carlo (dashed line). The graph shows the missing energy spectrum of carbon at $Q^2 = 3.3$ GeV and proton central angle of 24.8 degrees. The difference in yield is due to the (unsimulated) nuclear opacity of the real target.

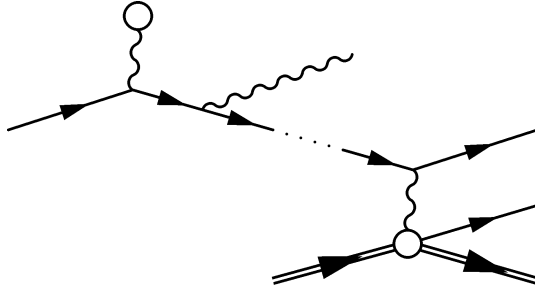


FIG. 4.3: Example of a diagram contributing to the external Bremsstrahlung cross-section.

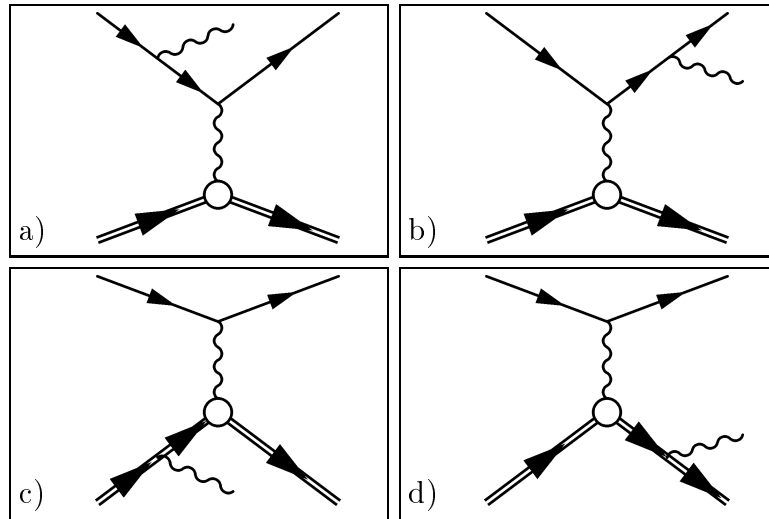


FIG. 4.4: Diagrams contributing to the internal Bremsstrahlung cross-section. A real photon is emitted by the incoming or outgoing electron or proton. Here the double line represents only the proton—radiation from the remnant nucleus is neglected.

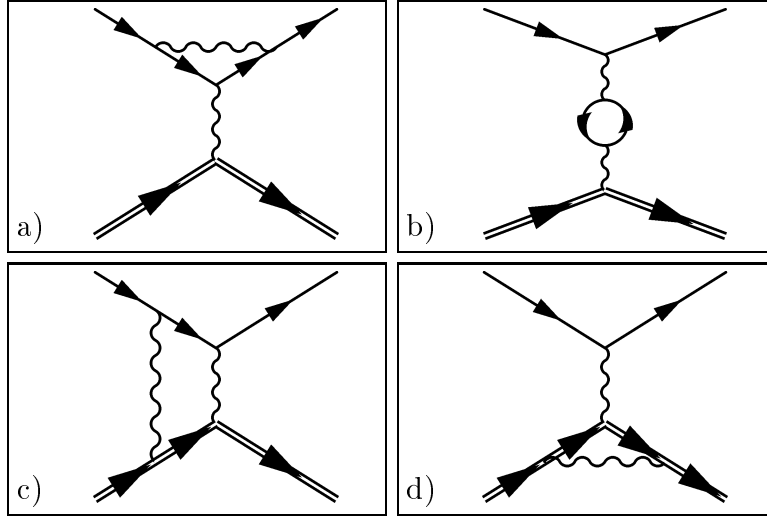


FIG. 4.5: Diagrams for first order corrections to the hard-scattering vertex. Here the double line represents only the proton—radiation from the remnant nucleus is neglected.

tive correction to the Monte Carlo events allows reasonable comparison between the simulation and the data as in Fig. 4.2. These corrections may be conveniently divided into three types: external Bremsstrahlung (see Fig. 4.3), internal Bremsstrahlung (see Fig. 4.4), and higher-order corrections to the hard-scattering vertex itself (see Fig. 4.5).

The methodology that SIMC uses to account for these processes is derived from that developed by Naomi Makins [14, 72] for the SIMULATE Monte Carlo following the work of Mo and Tsai [73]. The full calculation is rather involved. I will sketch this derivation to show how the SIMC procedure is derived from the theory. The theory consistently attempts to calculate a differential cross-section (of various variables) for elastic-proton scattering with various photon emissions.

The goal is to use the derived cross-section as a probability distribution from which the Monte Carlo can find event weights in $\langle E_m, \vec{p}_m \rangle$ space.

4.3.1 Internal Bremsstrahlung and Vertex Corrections

The bremsstrahlung calculations of Mo and Tsai assume an inclusive scattering event, and derive the cross-section, $\frac{d\sigma}{d\Omega_e}(\omega \leq \Delta E)$, for scattering an electron into a solid angle, Ω_e accompanied by the radiation of a single photon with energy, ω , not exceeding some threshold, ΔE [73].⁴ At this point the cross-section has two non-physical divergences: one arising in the limit of low photon energy, and another arising from the artificially introduced cutoff energy, ΔE .

The infrared divergence can be canceled by inclusion of the vertex correction terms (which are the same order in α). Here we note that in general, radiative corrections involving only electron-photon interaction can be calculated exactly, but corrections involving the proton are dependent on the incompletely known proton current distribution, and can be found only approximately. Makins includes the exactly calculable terms from Fig. 4.5 panels a) and b), and those terms from panels c) and d) needed to cancel the infrared divergences in the one photon bremsstrahlung cross-section. The proton-photon calculations are made using on-shell form-factors and kinematic quantities, but these approximations are believed to cause only small discrepancies in already small terms [72].

The energy-cutoff divergence can be removed by summing the corrections for emitting any number of soft photons, a procedure equivalent to exponentiation. Makins attributes the method for doing this to Yennie, Frautschi and Suura [74]. The cross-section found at this point still has the form we saw be-

⁴I will exhibit all these cross-sections in their elastic forms. The procedure generalizes to $A(e, e'p)$ without difficulty.

fore, $\frac{d\sigma}{d\Omega_e}(\sum \omega \leq \Delta E)$, except that we now require the total radiated energy of all bremsstrahlung photons to be less than ΔE .

This cross-section works well for inclusive experiments, but for coincidence measurements we need to calculate a more complicated cross-section that allows the determination of the radiated energy *and* momentum. Applying a peaking approximation⁵ to find the angular distribution of the bremsstrahlung radiation makes this possible. Finally, a change of variables is made by dividing the total bremsstrahlung radiation into three photons with energies E_i , E_f , and E_p , propagating in the direction of the incoming and outgoing electrons, and the ejected proton respectively.⁶ We write the cross-section as:

$$\begin{aligned} \frac{d\sigma}{d\Omega_e dE_i dE_f dE_p} &= \left. \frac{d\sigma}{d\Omega_e} \right|_{ep} (1 - \delta_{hard}) \\ &\times \frac{\lambda_i \lambda_f \lambda_p}{\left(\sqrt{k, k'}\right)^{\lambda_i} \left(\sqrt{k, k'}\right)^{\lambda_f} \left(\sqrt{m_p p'}\right)^{\lambda_p}} \\ &\times \frac{1}{E_i^{1+\lambda_i} E_f^{1+\lambda_f} E_p^{1+\lambda_p}}, \end{aligned} \quad (4.7)$$

where m_p is the proton mass, δ_{hard} is contribution from uncanceled vertex correction terms,

$$\delta_{hard} = 2\alpha \left[-\frac{3}{4\pi} \ln \left(\frac{-q^2}{m_e^2} \right) + \frac{1}{\pi} - \sum_{j \in \text{quarks, leptons}} \frac{1}{3\pi} \left[-\frac{5}{3} + \ln \left(\frac{-q^2}{m_j^2} \right) \right] \right],$$

⁵Makins employs an extended peaking approximation to obtain the angular distribution on bremsstrahlung photons while retaining the interference effects and the correct normalization which are lost in the more naive treatment.

⁶We will use this convention of labeling quantities by i , f , and p when they are related to the initial electron, the final electron, and the proton respectively through-out this section.

and the λ 's are given by:

$$\begin{aligned}\lambda_i &= \frac{\alpha}{\pi} \left[\ln \left(\frac{4k^2}{m_e^2} \right) + 2 \ln \left(\frac{k}{k'} \right) + \ln \left(\frac{1 - \cos \Theta_e}{2} \right) - 1 \right], \\ \lambda_f &= \frac{\alpha}{\pi} \left[\ln \left(\frac{4k'^2}{m_e^2} \right) + 2 \ln \left(\frac{k}{k'} \right) + \ln \left(\frac{1 - \cos \Theta_e}{2} \right) - 1 \right], \\ \lambda_p &= \frac{\alpha}{\pi} \left[\ln \left(\frac{p' + |\vec{p}'|}{p' - |\vec{p}'|} \right) - 2 \right].\end{aligned}$$

4.3.2 External Bremsstrahlung

Electrons can also radiate in the field of nuclei that are spectators to the main interaction, a process called external bremsstrahlung. SIMC treats external bremsstrahlung starting at the scattering chamber entrance window, and following the particles all the way through the spectrometer entrance windows, but neglects it for material that the particles may encounter after they have entered the spectrometer magnets because energy loss and multiple scattering are the dominant corrections at that point.

External bremsstrahlung receives a slightly different treatment to take advantage of its incoherent nature. The method of Early [75] is well suited for this purpose. External bremsstrahlung from the proton is strongly suppressed relative the effects on the incoming and outgoing electrons, and is neglected. Early derives an expression of the probability of a fermion with momentum \vec{k} radiating a total energy E^{ext} when traversing t radiation lengths of material with atomic charge Z . For convenience, Early expresses the Z dependence in terms of:

$$b = \frac{1}{9} \left(12 + \frac{Z+1}{ZL_1 + L_2} \right),$$

$$\begin{aligned}
L_1 &= 5.216 - \frac{1}{3} \ln(Z), \\
L_2 &= 7.085 - \frac{2}{3} \ln(Z).
\end{aligned}$$

The code assumes that the target is much thicker than the windows and air gaps, and calculates b using the atomic charge of the target. Also present in Early's solution is a correction for high photon energies which SIMC approximates as:

$$\Phi_i^{ext}(E_i) = 1 - \frac{bt_i}{bt_i - \lambda_i} \frac{E_i}{|k_i|},$$

and similarly for the scattered electron.

Again, the extended peaking approximation is applied and a change of variables into a two-photon basis is made. The results are combined with the earlier expression for the internal bremsstrahlung and vertex corrections giving [4, 14, 68, 72]:

$$\begin{aligned}
\frac{d\sigma}{d\Omega_e dE_i dE_f dE_p} &= \left. \frac{d\sigma}{d\Omega_e} \right|_{ep} (1 - \delta_{hard}) \\
&\times \frac{1}{\Gamma(1 + bt_e)} \frac{bt_i + \lambda_i}{k^{bt_i} (\sqrt{k}k')^{\lambda_i}} \frac{1}{E_i^{1-\lambda_i-bt_i}} \Phi_i^{ext}(E_i) \\
&\times \frac{1}{\Gamma(1 + bt_f)} \frac{bt_f + \lambda_f}{k'^{bt_f} (\sqrt{k}k')^{\lambda_f}} \frac{1}{E_f^{1-\lambda_f-bt_f}} \Phi_f^{ext}(E_f) \\
&\times \frac{\lambda_p}{(\sqrt{M_p p'})^{\lambda_p}} \frac{1}{E_p^{1-\lambda_p}}, \tag{4.8}
\end{aligned}$$

exhibited here in a form which makes the four independent corrections clear.

4.3.3 Monte Carlo Weight Generation

Eq. (4.8) gives the five-fold (nine-fold for quasi-elastic processes) differential cross-section for scattering with radiative corrections. But SIMC has to bin these events in the two-fold (six-fold)⁷ phase space of the scattered (and recoiling) particles. An integration is in order:

$$\begin{aligned}
\frac{d\sigma}{d\Omega_e} \text{RadCor} &= \int_{\text{radiative phasespace}} dE_i dE_f dE_p \frac{d\sigma}{d\Omega_e dE_i dE_f dE_p} \quad (4.9) \\
&= \left. \frac{d\sigma}{d\Omega_e} \right|_{ep} (1 - \delta_{hard}) \\
&\quad \times \frac{1}{\Gamma(1 + bt_e)} \frac{bt_i + \lambda_i}{k^{bt_i} (\sqrt{k k'})^{\lambda_i}} \int dE_i \frac{1}{E_i^{1-\lambda_i-bt_i}} \Phi_i^{ext}(E_i) \\
&\quad \times \frac{1}{\Gamma(1 + bt_f)} \frac{bt_f + \lambda_f}{k'^{bt_f} (\sqrt{k k'})^{\lambda_f}} \int dE_f \frac{1}{E_f^{1-\lambda_f-bt_f}} \Phi_f^{ext}(E_f) \\
&\quad \times \frac{\lambda_p}{(\sqrt{M_p p'})^{\lambda_p}} \int dE_p \frac{1}{E_p^{1-\lambda_p}}. \quad (4.10)
\end{aligned}$$

We seek a multiplicative factor, W_{rad} , to weight each event. If values for E_i , E_f , and E_p are drawn randomly for the correct distributions for each event and used to calculate W_{rad} , the Monte Carlo will perform the integrals automatically. All other factors may be inserted directly into the weight, or grouped with the integrals. SIMC computes the last three lines of Eq. (4.10) by the usual Monte Carlo method [4, 68].⁸

⁷Strictly one (five) dimensional. See footnote 19 in Chapter 1.

⁸Given a non-negative probability distribution of the form $g(x)$ defined and normalized over the range $[a, b]$, we define the cumulative probability distribution $F(x) = \int_a^x g(x') dx'$. The original probability distribution, $g(x)$ can be sampled by throwing G randomly over the range $[0, 1]$ and computing $x = F^{-1}(G)$, a result known as the Fundamental Theorem of Sampling. The integral $\int_a^b f(x)g(x)dx$ may be computed by summing $f(x_i)$ over many samples of x_i from g [76].

4.4 Other Features, Physics, and Corrections

A physically meaningful model requires careful consideration of a great many factors. In this section, I give an overview of some of the work SIMC does.

4.4.1 Offshell Cross-section

As discussed in Section 1.6.1 it is necessary to select a model of the electron's interaction with the off-shell proton. SIMC provides several choices, but uses deForest's $\sigma_{cc}^{(1)}$ model by default [34]. This is also the choice made for e94-139. Previous investigation suggest that the error introduced by this choice is quite small throughout the kinematic region that we investigate [3].

4.4.2 Coulomb Correction

Though we have concerned ourselves with the interaction of the electron with a single constituent proton of a nucleus, the Coulomb attraction between the incident electron and the nucleus affects the course of the interaction. This effect can be described by summing the Feynmann diagrams in which the electron exchanges one or more photons with the nucleus (as a whole) in addition to its hard interaction with the proton. SIMC uses an equivalent semi-classical prescription involving an adjustment to the initial and final electron momenta, implying an alteration of the momentum transfer and a concurrent adjustment of the electron-nucleon cross-section [77].

Writing R_C for the effective charge radius of the nucleus, we corrected the electron momenta by:

$$k_{i,f}^{\text{eff}} = k_{i,f} + f_C \frac{\alpha Z}{R_C}, \quad (4.11)$$

where f_C depends on the nuclear charge distribution. For a uniform spherical distribution $f_C = 1.5$, and we expect this to be a good approximation for heavy nuclei. SIMC chooses this value randomly (but non-uniformly, rather tending towards higher values) between .75 and 1.5.

The alteration of the electron momenta affects the momentum transfer:

$$\mathbf{q}^{\text{eff}} = \mathbf{q} \left(1 f_C \frac{\alpha Z}{R_C k_f} \right) + f_C \frac{\alpha Z \mathbf{k}_i}{R_C} \left(1 - \frac{k_i}{k_f} \right). \quad (4.12)$$

Note that the direction as well as the magnitude may be affected.

Finally, the e - p cross-section is altered, both in that it should be calculated at the effective kinematics, and in the addition of a normalizing term that restores the original asymptotic behavior:

$$\sigma_{ep}^{\text{eff}} = \left(\frac{k_i^{\text{eff}}}{k_i} \right)^2 \sigma_{ep}(k_i^{\text{eff}}, k_f^{\text{eff}}, q^{\text{eff}}, p, E). \quad (4.13)$$

4.4.3 Spectrometer Models

The two spectrometers are implemented as separate modules in the code, and are optional. The simulation can be instructed to quit after event generation, dispensing with transport to the spectrometer focal planes and projection of the results back to the target

SIMC's focal plane to vertex mapping uses the same method as Replay, but SIMC must first map vertex quantities to the focal plane. This is accomplished by a set of “reverse” matrix elements computed from the same COSY model used to generate the matrix elements for the analyzer [4]. Transport proceeds in

a stepwise fashion from one landmark to another, with multiple scattering and energy loss computed and folded in at each step.

4.4.4 Energy Loss and Multiple Scattering

The Monte Carlo can correct the path and momenta of particles propagating through the spectrometer for energy loss and multiple scattering. Indeed, standard practice is to enable these corrections to obtain the best possible physical approximation, however these features can be turned off if desired (as in Section 5.4.1).

Further, if energy losses are being calculated, the energies assigned to the particle by the reconstruction routines can be corrected for the most probable energy loss. This option is separate from that for doing the energy loss while propagating the particle through the spectrometer, and *should* be enabled, because the analyzer always does so.

4.4.5 Correlation Correction

The spectroscopic factors (See Section 4.2) used in the theoretical spectral functions were determined by integrating the actual strength over a small (≈ 20 MeV) range in missing energy above the nominal position of the peak. However our yields are measured over a larger range (missing energies up to 80 MeV), so the basic spectroscopic factors will mis-estimate the actual yield. Makins calculated a “correlation correction” on a per nuclei basis which she used in place of the spectroscopic factor provided.⁹

⁹Makins’ correlation correction also has the opposite sense of the spectroscopic factor. That is, where the spectroscopic factor is a number less than unity by which the simulated yield is multiplied to get the corrected yield, the correlation correction is a number greater than unity by which the simulated yield must be divided.

4.5 SOS Extended Target Acceptance

Table 2.2 lists the SOS extended target acceptance as ± 1.0 cm.¹⁰ In fact events originating further from the central ray can be accepted by the spectrometer, but the acceptance in this region is a complicated function of y_{target} , y'_{target} , and δ (momentum expressed as a fraction of the spectrometer's central momentum).

For our 4 cm liquid targets and our fairly large spectrometer angles (see Table 1.1), the SOS acceptance during data taking never fully covered the target region, and we have events originating at high y_{target} .

Unfortunately, the Monte Carlo encounters difficulty modeling the acceptance near the edges of the SOS y_{target} acceptance. Though we believe that the problem is understood—we can get the right yields if a small y_{target} cut is imposed—we have chosen to use the hydrogen elastic data (which has neither correlation corrections, nor nuclear FSIs to complicate it) to normalize the deuterium yields. The Monte Carlo correctly replicates the world data set average for hydrogen elastic cross-section, so we compute the nuclear transparency for hydrogen data, and use this quantity to normalize the Monte Carlo yields for deuterium. This procedure should neatly cancel the extended target acceptance problems and allow us to retain our full statistics [78].

¹⁰This quantity (called y_{target}) is in the spectrometer coordinate system, so the acceptance along the beam in the Hall coordinate system is larger by a factor of $(\sin(\theta_{\text{SOS}}))^{-1}$.

5. PHYSICS ANALYSIS

With an understanding of both the experiment and the simulation in hand, we can proceed to extract some physics from the data.

5.1 Extraction of the Transparency

As stated in Section 1.4.1 we define the transparency as the ratio of the physical yield to the theoretical yield, a largely operational definition, which allows us to proceed in a straightforward way.

5.1.1 Analysis Cuts

All data are subject to a set of nominal cuts intended to limit the analysis to actual (quasi-) elastic events collected in the portion of the spectrometer's acceptance for which the spectrometer optics are well understood. The sole exception to this is the lack of a cut on the SOS extended target acceptance which is treated by the means explained in Section 4.5. The cuts we use are listed in Table 5.1.

The data are analyzed only over a particular kinematic range that we believe to be well understood. For heavy nuclei, we used the region defined by $0 < E_m < 80$ MeV and $-300 < p_m < 300$ MeV,¹ while for hydrogen and

¹This is the same range used in calculating the correlation correction (see Section 4.4.5).

TABLE 5.1: Analysis cuts. Kinematic cuts were applied to both the actual data and the Monte Carlo results in the same way. Particle identification cuts were applied only to our real data.

Quantity	Limits		Units
	Lower	Upper	
Kinematic Cuts			
HMS Momentum Fraction (δ)	-8.0	8.0	%
SOS Momentum Fraction (δ)	-15.0	15.0	%
HMS x' at target	-.08	.08	mrاد
SOS x' at target	-.04	.04	mrاد
HMS y' at target	-.04	.04	mrاد
SOS y' at target	-.08	.08	mrاد
Particle Identification Cuts			
Coincidence time	21.	31.	ns
Invariant Mass	.05		GeV
HMS β	.7	1.15	
SOS Cerenkov photons	2.		photons
SOS Calorimeter Fractional Energy on Track	.6		

TABLE 5.2: Correction applied to raw data and Monte Carlo yields. No correction is made for the SOS trigger efficiency for reasons explained in Section 3.2.1.

Correction	Applied to	Value
Data		
Proton Absorption	All	1.05-1.07
Cryo-target density	H,D	$2.0 \pm 0.4\%$ at $60 \mu\text{A}$
HMS Tracking Efficiency	All	run-by-run
SOS Tracking Efficiency	All	run-by-run
HMS Trigger Efficiency	All	run-by-run
HMS Dead Time	All	run-by-run
SOS Dead Time	All	run-by-run
Dummy target subtraction	H,D	
Monte Carlo		
Extended Target Normalization	D	T_{H}
Correlation correction	C	$(1.11 * .56)^{-1} = 1.61$
	Fe	$(1.22 * .36)^{-1} = 2.28$

deuterium it was necessary to extend the missing energy range down to -10 MeV because these targets have negligible or non-existent separation energies.

5.1.2 Yield Corrections

Various corrections are applied to both the simulated and real data to account for experimental losses, remove the spectroscopic factor included in the model spectral functions, and introduce the correlation correction. Table 5.2 shows the corrections applied. These corrections have all been discussed earlier, but it is worth noting here how they are applied. The dead times, fiducial efficiencies, and trigger efficiencies are determined programatically by Replay, and

applied on a run-by-run basis automatically in subsequent analysis. The dummy target subtraction and cryo-target density correction are applied to the liquid target data. The dummy target data were taken at similar kinematics, and are normalized for charge and the extra thickness of the dummy target walls. Cryo-target density corrections are calculated on the basis of the average run current. Proton absorption depends on the target and geometry (see Section 3.6.6) with a fixed value of 4.65% for the mass encountered in the HMS, and a target dependent correction given in Table 3.5. The SOS extended target normalization is applied by multiplying the SIMC weight by the transparency found for hydrogen in the same kinematics.

5.2 Relationship Between the Cross-Sections

This section explores the relationship between the fundamental scattering cross-section expressed in kinematic quantities at the vertex, and the measured experimental yields expressed in experimental observables. Also of interest is the relationship between the theoretical spectral function and the experimental spectral function as expressed in missing energy and momentum. Understanding this relationship is the first step towards extraction of the spectral functions which will be done in more detail in Section 5.3.

We follow (roughly) Dutta’s discussion [3].

Our strategy here is to write the yield for the underlying physical process in terms of a one photon exchange cross-section plus Bremsstrahlung radiation, then transform from the vertex variables into experimental observables. A series of approximations will simplify this complex expression into a part measured directly, and a phase-space factor which can be modeled by the Monte Carlo.

5.2.1 Physical Process

The correct physical yield over some volume, V , of phase space in the proton and electron kinematic variables E' , $\Omega_{p'}$, ϵ' , and $\Omega_{k'}$, is given by:

$$N(V) = L * \int_V \frac{d^6 \sigma_{\text{physics}}}{dE' d\Omega_{p'} d\epsilon' d\Omega_{k'}} dE' d\Omega_{p'} d\epsilon' d\Omega_{k'}. \quad (5.1)$$

This serves as a definition of σ_{physics} . SIMC assumes a one photon exchange (OPE) interaction, and applies corrections for Bremsstrahlung, so we rewrite this in terms of the OPE cross section (which we write without subscript for brevity) and a radiation smearing function, $R(\vec{p}'_r, \vec{k}'_r; \vec{p}', \vec{k}')$:²

$$N(V) = L * \int_V d^6 V_r \int_{\vec{p}', \vec{k}'} R(\vec{p}'_r, \vec{k}'_r; \vec{p}', \vec{k}') \frac{d^6 \sigma}{dE' d\Omega_{p'} d\epsilon' d\Omega_{k'}} dE' d\Omega_{p'} d\epsilon' d\Omega_{k'}.$$

5.2.2 Finite Detectors

So far we have been working with the physics yield in an idealized system. Now we concern ourselves with two issues arising from the limits of the experimental apparatus and methodology.

The spectrometers have finite acceptance and resolution, which smear the observables still further. We integrate over an acceptance function denoted by $A(p'_{exp}, k'_{exp}; p'_r, k'_r)$. Also, we wish to express the results in terms of the missing energy and momentum, rather than the individual particle kinematic quantities.

²While I have been striving for notational consistency throughout this document, this particular discussion poses some problems. We are starting with an expression (Eq. (5.1)) written in the vertex variables of Section 1.3, and have to make several transformations in the form of integrations over the experimental volume of the yield multiplied by a transforming function. A mathematician would usually use one or more primes (') to distinguish the coordinates of each of these integrations, but I have already used that notation to indicate final-state kinematic variables. My solution is to introduce (hopefully mnemonic) variable subscripts as needed. Thus \vec{p}'_r is the final-state proton momentum after radiation, and so on.

Putting this together, we get:

$$N(V) = L * \int_V d^6 V_{exp} \int_{\vec{p}_r, \vec{k}_r} d^6 V_r A(\vec{p}_{exp}, \vec{k}_{exp}; \vec{p}_r, \vec{k}_r) \\ \int_{\vec{p}', \vec{k}'} R(\vec{p}_r, \vec{k}_r; \vec{p}', \vec{k}') \frac{d^6 \sigma}{dE' d\Omega_{p'} d\epsilon' d\Omega_{k'}} dE' d\Omega_{p'} d\epsilon' d\Omega_{k'}$$

and then choosing as our volume a rectangular bin defined by E_m , ΔE_m , \vec{p}_m , and $\Delta \vec{p}_m$

$$N(E_m, \Delta E_m, \vec{p}_m, \Delta \vec{p}_m) = L * \int_{E_m, \Delta E_m, \vec{p}_m, \Delta \vec{p}_m} dE_m d^3 \vec{p}_m \int_V d^6 V_{exp} \\ \delta(E_m - (\epsilon - \epsilon'_{exp} - E'_{exp} + M_p - T^{rec})) \delta(\vec{p}_m - (\vec{k} - \vec{k}'_{exp} - \vec{p}'_{exp})) \\ \int_{\vec{p}_r, \vec{k}_r} d^6 V_r A(\vec{p}_{exp}, \vec{k}_{exp}; \vec{p}_r, \vec{k}_r) \\ \int_{\vec{p}', \vec{k}'} R(\vec{p}_r, \vec{k}_r; \vec{p}', \vec{k}') \frac{d^6 \sigma}{dE' d\Omega_{p'} d\epsilon' d\Omega_{k'}} dE' d\Omega_{p'} d\epsilon' d\Omega_{k'}$$

This rather intimidating expression may be simplified by the use of some approximations.

5.2.3 Finite Resolution and Averaging

Limited accuracy and precision in the detectors (and in our understanding of the detectors) is another source of imprecise mapping between the vertex variables and the observed missing energy and momenta. SIMC models these effects, and we group them into the acceptance function A .

For the purposes of continuing the analysis, we assume that:

- The spectrometers do not bias the measurements, i.e. that $\mathbf{p}'_{exp} = \mathbf{p}'_r$, etc. This can be reasonably expected to hold except at the edges of our acceptance.

- That the spectrometer acceptances are independent. That is we may write
(also applying the first item)

$$A(\vec{p}_{exp}, \vec{k}'_{exp}; \vec{p}_r, \vec{k}'_r) = A(\vec{p}_{exp})A(\vec{k}'_{exp})\delta(\vec{k}'_{exp} - \vec{k}'_r)\delta(\vec{p}_{exp} - \vec{p}_r).$$

Applying these assumptions, and inserting the appropriate Jacobian for transformation from physics coordinates to the experimental coordinates,

$$|J| = \frac{1}{(1 + (\Delta\theta_{e'})^2 + (\Delta\phi_{e'})^2)^{3/2}(1 + (\Delta\theta_{p'})^2 + (\Delta\phi_{p'})^2)^{3/2}},$$

and integrating over V_r and the primed vertex coordinates we express the yield in a particular (E_m, \vec{p}_m) bin as:

$$\begin{aligned} N_{bin} &= N(E_m, \Delta E_m, \vec{p}_m, \Delta \vec{p}_m) \\ &= L * \int_{E_m, \Delta E_m, \vec{p}_m, \Delta \vec{p}_m} dE_m d^3 \vec{p}_m \int_V d^6 V_{exp} \\ &\quad \delta(E_m - (\epsilon - \epsilon'_{exp} - E'_{exp} + M_p - T^{rec})) \delta(\vec{p}_m - (\vec{k} - \vec{k}'_{exp} - \vec{p}_{exp})) |J| \\ &\quad A(\vec{p}_{exp}) A(\vec{k}'_{exp}) \int_{\vec{p}', \vec{k}'} R(\vec{p}_{exp}, \vec{k}'_{exp}; \vec{p}', \vec{k}') \frac{d^6 \sigma}{dE' d\Omega_{p'} d\epsilon' d\Omega_{k'}} dE' d\Omega_{p'} d\epsilon' d\Omega_{k'} \\ &= L * \int_{E_m, \Delta E_m, \vec{p}_m, \Delta \vec{p}_m} dE_m d^3 \vec{p}_m \int_V d^6 V_{exp} \\ &\quad \delta(E_m - (\epsilon - \epsilon'_{exp} - E'_{exp} + M_p - T^{rec})) \delta(\vec{p}_m - (\vec{k} - \vec{k}'_{exp} - \vec{p}_{exp})) |J| \\ &\quad A(\vec{p}_{exp}) A(\vec{k}'_{exp}) \frac{d^6 \sigma^R}{dE'_{exp} d\Omega_{p'_{exp}} d\epsilon'_{exp} d\Omega_{k'_{exp}}}. \end{aligned}$$

The last equivalence defines $\frac{d^6 \sigma^R}{dE'_{exp} d\Omega_{p'_{exp}} d\epsilon'_{exp} d\Omega_{k'_{exp}}}$, the radiated, OPE, differential cross-section in the measured vertex variables.

5.2.4 Defining the Experimental Spectral Function

The general partition of a quasi-elastic cross-section into spectral function and fundamental parts has the form introduced in Eq. (1.15):

$$\frac{d^6\sigma}{dE'd\Omega_{p'}d\epsilon'd\Omega_{k'}} = E'p'\sigma_{ep}S(E_m, p_m). \quad (5.2)$$

Applying this to the radiated OPE cross-section, we write:

$$\frac{d^6\sigma^R}{dE'_{exp}d\Omega_{p'_{exp}}d\epsilon'_{exp}d\Omega_{k'_{exp}}} = E'_{exp}p'_{exp}\sigma_{ep}S^R(E_m, p_m), \quad (5.3)$$

where $S^R(E_m, p_m)$ is the radiation smeared (or radiated) spectral function in the spirit of Eq. (1.23).

Now making the assumption that both the radiated fundamental cross-section and the spectral function are slowly varying over our bins, we average them, and take them out of the integrals:

$$\begin{aligned} N_{bin} &= L\bar{E}'_{exp}\bar{p}'_{exp}\bar{\sigma}_{ep}S_{bin}^R|J| \\ &\int_{E_m, \Delta E_m, \vec{p}_m, \Delta \vec{p}_m} dE_m d^3\vec{p}_m \int_V d^6V_{exp} A(\vec{p}_{exp}) A(\vec{k}'_{exp}) \\ &\delta(E_m - (\epsilon - \epsilon'_{exp} - E'_{exp} + M_p - T^{rec})) \delta(\vec{p}_m - (\vec{k} - \vec{k}'_{exp} - \vec{p}'_{exp})), \end{aligned} \quad (5.4)$$

where the barred quantities represent appropriate averages over the bin.³

The integral over V_{exp} (is a Jacobian which) establishes the relation between the vertex energy and momenta, E_m and p_m , and the energy and momenta

³The Mean-Value Theorem guarantees that this replacement is valid for some values of \bar{E}'_{exp} , \bar{p}'_{exp} , $\bar{\sigma}_{ep}$, and S_{bin}^R between their respective extrema, but does not guarantee a closed form means of finding the correct values. The slowly varying condition serves to limit the error that can be made by a poor choice. See Eq. (5.8) in Section 5.3.1.

observed in the spectrometers subject to physical conservation requirements: that is the phase space available to the reaction in terms of the experimental observables. The presence of the acceptance functions means that it cannot be calculated in closed form, but this is part of what SIMC models. The remaining integrals limit the evaluation to the chosen bin in (E_m, p_m) space. We define the phase space over a bin as:

$$\begin{aligned}
\mathcal{P}_{bin} &= \mathcal{P}(E_m, \Delta E_m, p_m, \Delta p_m) \\
&= \int_{E_m, \Delta E_m, \vec{p}_m, \Delta \vec{p}_m} dE_m d^3 \vec{p}_m \int_V d^6 V_{exp} A(\vec{p}_{exp}) A(\vec{k}'_{exp}) \\
&\quad \delta(E_m - (\epsilon - \epsilon'_{exp} - E'_{exp} + M_p - T^{rec})) \delta(\vec{p}_m - (\vec{k} - \vec{k}'_{exp} - \vec{p}_{exp})).
\end{aligned} \tag{5.5}$$

Together Eqs. (5.3) and (5.5) lead to our goal:

$$N_{bin} = L \bar{E}'_{exp} \bar{p}'_{exp} \bar{\sigma}_{ep}^R S_{bin}^R |J| \mathcal{P}_{bin}. \tag{5.6}$$

Now we simply rewrite Eq. (5.6) to express the spectral function in terms of the yield and other quantities:

$$S_{bin}^R = \frac{N_{bin}}{L \bar{E}'_{exp} \bar{p}'_{exp} \bar{\sigma}_{ep}^R |J| \mathcal{P}_{bin}}. \tag{5.7}$$

5.3 Extraction of the Spectral Function

This and the following sections build upon the work of Sections 1.6 and 5.2 (with particular reference to Subsection 5.2.4) in which the meaning of the spectral function was discussed and placed in the context of the experimental observables.

5.3.1 Calculation of the Spectral Function

Eq. (5.7) provides a framework for extracting the spectral function from the data and some results of the Monte Carlo, but some questions remain unanswered.

We divide Eq. (5.7) into a part to be calculated by SIMC, and a part to be found from the data like this:⁴

$$\begin{aligned}
S_{bin}^R &= \left[\frac{1}{L\mathcal{P}_{bin}} \right]_{SIMC} \left[\frac{N_{bin}}{\bar{E}'_{exp} \bar{p}'_{exp} \bar{\sigma}_{ep}^R |J|} \right]_{data} \\
&= \left[\sum_{events} \frac{weight}{E' p' \sigma_{ep} SW_{rad}} \right]_{SIMC}^{-1} \left[\sum_{events} \frac{1}{E' p' \sigma_{ep} |J|} \right]_{data} \\
&= \frac{1}{L\mathcal{P}} K.
\end{aligned} \tag{5.8}$$

Here L is the (fixed) luminosity, \mathcal{P} is the phase space and K is the sum of the inverse cross-sections related to each data event. A straight-forward analysis provides an uncertainty estimator for this expression of

$$\begin{aligned}
[\Delta S_{bin}^R]^2 &= \left(\frac{\delta S_{bin}^R}{\delta \mathcal{P}_{bin}} (\Delta \mathcal{P}) \right)^2 + \left(\frac{\delta S_{bin}^R}{\delta K_{bin}} (\Delta K) \right)^2 \\
&= \left(-\frac{S_{bin}^R}{\mathcal{P}} \right)^2 (\Delta \mathcal{P})^2 + \left(\frac{S_{bin}^R}{K} \right)^2 (\Delta K)^2 \\
&= (S_{bin}^R)^2 * \left[\frac{(\Delta \mathcal{P})^2}{\mathcal{P}^2} + \frac{(\Delta K)^2}{K^2} \right].
\end{aligned}$$

Now we are left with the problem of evaluating the uncertainty in the phase space calculation and our convenience variable, K . For each we can find a statistical variance by the usual method while we are finding the sums that appear in Eq. (5.8), but if the values summed are (nearly) equal, the error will be dominated

⁴This relation establishes how we will take the averages needed for Eq. (5.4). See footnote 3.

by the statistics of counting (i.e. the Poisson distribution error). In practice we calculate both and use the larger. Both terms also include a calculation of the cross-section which includes a model dependent uncertainty. See Section 5.6.4.

In order for this procedure to work correctly, the data and Monte Carlo distributions must occupy the same part of the (E_m, p_m) phase space to a precision similar to our detector resolution, and certainly better than the bin spacing used in defining C_{bin} . However our data consistently appears at lower missing energy than the Monte Carlo results generated from the same kinematics. The size of the discrepancy is as high as 6 MeV. This is almost certainly due to a misunderstanding of the beam energy or spectrometer central momenta. Eq. (1.8) shows how these quantities enter into the determination of the missing energy.

Accordingly, before extracting the spectral function, the real and simulated data are fit with a reasonable function⁵, and the fits used to prescribe a missing energy offset for the real world data. The final results are surprisingly sensitive to this parameter, and we found it necessary to invest some time in this process.

5.4 Deradiation of the Data

We have just extracted a spectral function from the data, but it is not useful for comparison to theory. While the nuclear shells can be discerned in results of this kind, they are artificially broadened by energy loss, multiple scattering, imperfect understanding of the spectrometer optics, and even by the granularity of the spectrometers themselves. Fig. 5.1 displays an example result. Further, they are not cleanly resolved because the large radiative tails from shells at low E_m contribute significant background to shells at higher E_m . We would like to map

⁵One or more Lorentzians exponentially smeared towards higher missing energy to simulate radiative corrections.

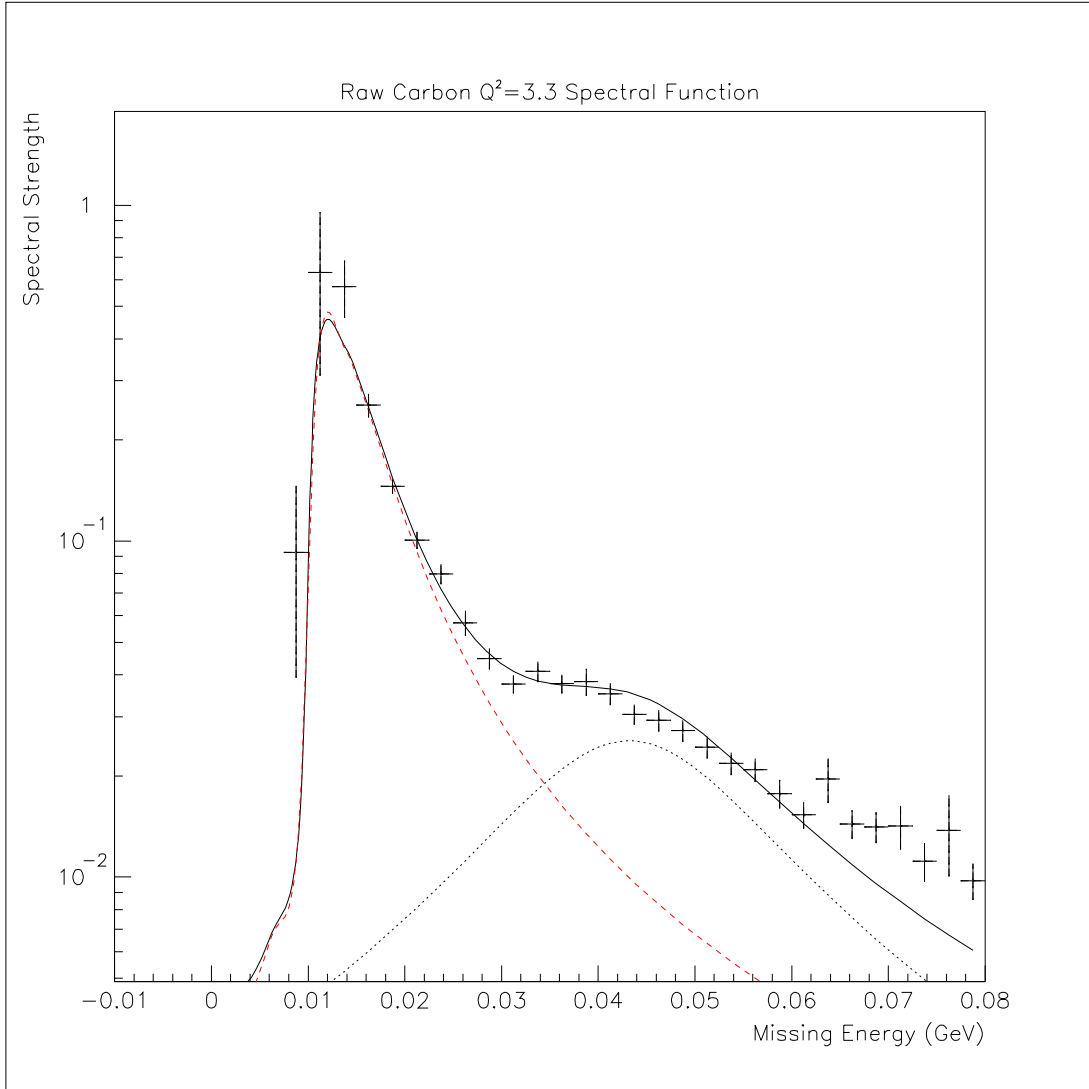


FIG. 5.1: The missing energy dependence of the raw spectral function extracted from our data on carbon at $Q^2 = 3.3 \text{ GeV}^2$. The lines represent simple fits and are intended as rough guides only. We fit each peak with a Lorentzian exponentially smeared towards high missing energy, and apply a cutoff at low missing energy. The solid line is the sum of the p-shell (dashed line) and s-shell (dotted line) results, and can be seen to reasonably represent the data. The large extent to which each shell underlies the other is partially due to the intrinsic width of the states, but is exacerbated by radiative effects and the intrinsic imperfection of the measurement. Compare with Fig. 5.3.

this spectral function back to the vertex spectral function (essentially undoing the all of these effects).

Radiative corrections are the single biggest effect present, and we call this process of removing them “deradiation.”

SIMC uses a physics model that works in the one photon exchange approximation, then adds internal- and external-bremsstrahlung radiation, multiple scattering, etc—in essence what we did in Section 5.2—so it should be well suited to unfolding the radiative effects. We are going to rely on SIMC’s ability to correctly model the physics of the actual experiment.

5.4.1 An Ideal Experiment

Imagine, if you will, a “perfect” quasi-elastic scattering detector. Its energy and momentum resolution are much finer than any detail we might be interested in, and it measures (somehow) the vertex values of energy and momentum for the scattered particles without radiative corrections, energy loss, or multiple scattering.

This is not a realizable device, but SIMC can model it. Clearly the experimental spectral function extracted from data collected by such a device would be the desired observable: it would be a good approximation to the real spectral function.

5.4.2 Mapping Out the Radiation and Other Effects

All the physical processes which smear the experimental spectral function are redistributive. That is, they move events in (E_m, p_m) space, but do not change the number of events occurring.⁶

⁶This is only strictly true in the limit of full acceptance. For real devices, events which “should” fall just inside the acceptance can be shifted outside, and vice versa. SIMC’s design

Consider a small region, \mathcal{A} , of (E_m, p_m) space. It can be expected to receive n events at the vertex level. Some of these will experience bremsstrahlung radiation, and be measured by the real detectors in some other part of (E_m, p_m) space. Some events from other “starting locations” will radiate and be measured in region \mathcal{A} . Multiple scattering will push some events which started in \mathcal{A} to other places, and some that started elsewhere into \mathcal{A} . And so on. In the end the real detectors will measure m events in region \mathcal{A} . If we form $f(\mathcal{A}) = \frac{m}{n}$, the redistributive nature of these processes means that $\int dE_m dp_m f = 1$.

If the simulation is correctly modeling the physical processes which introduce this redistribution, then it should be performing the same redistribution, and we can use the fact to back them out.

We define a bin-by-bin correction factor C_{bin} such that the fundamental spectral function S_{bin} is related to the experimental spectral function by:⁷

$$S_{bin} = C_{bin} S_{bin}^R. \quad (5.9)$$

If the Monte Carlo is correctly modeling the fundamental interaction, and the radiative processes, we can extract an approximation to C_{bin} by taking the ratio of the spectral functions of two runs with the same conditions, one modeling the

makes allowances for this fact by initially generating events over a region larger than the actual acceptance. We make further allowance, by extracting and deradiating the spectral functions over a region larger still, before restricting the integration and reporting of results to the canonical area. The validity of this approach was checked, by testing the dependence of our results at one kinematics on a variation of our initial analysis region. No sensitivity was observed.

⁷The corrections function C_{bin} defined here differs from that defined by Dutta [3], but the result derived will be the same.

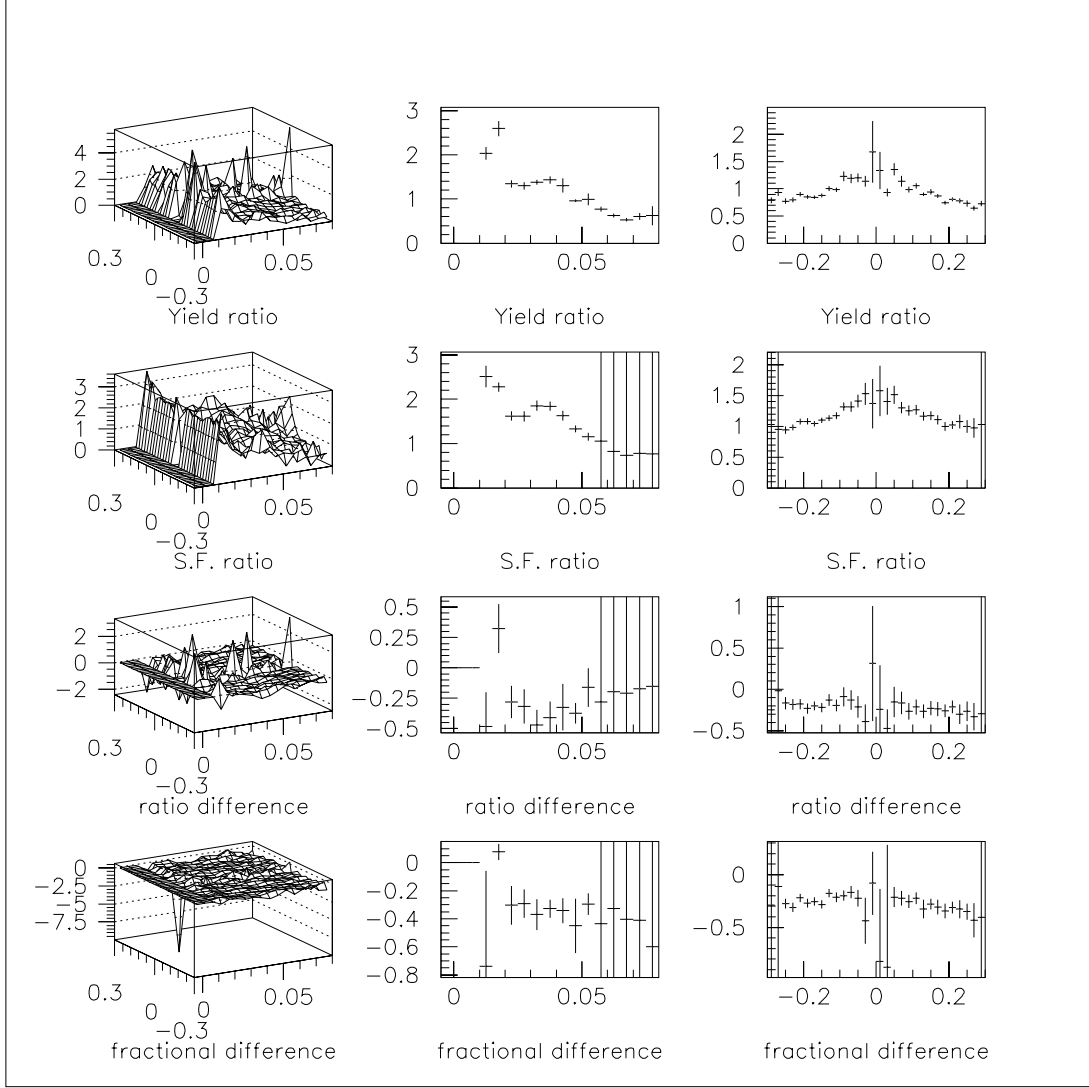


FIG. 5.2: A comparison of $\frac{S_{bin}^{MC,norad}}{S_{bin}^{MC,rad}}$ with $\frac{N_{bin}^{MC,norad}}{N_{bin}^{MC,rad}}$ for ^{12}C at $Q^2 = 3.3 \text{ GeV}^2$. Both Monte Carlo runs generated 200,000 simulated events. The ratios differ appreciably, suggesting that the yield ratio is not a sufficiently accurate estimate to the spectral function ratio.

real detectors, and one modeling the ideal detector of Section 5.4.1:

$$C_{\text{bin}} = \frac{S_{\text{bin}}^{MC,norad}}{S_{\text{bin}}^{MC,rad}}. \quad (5.10)$$

Dutta observed that the final yield is related linearly to the spectral function, and relied on this fact to define a correction factor equivalent to:

$$C_{\text{bin}}^{\text{yield}} = \frac{N_{\text{bin}}^{MC,norad}}{N_{\text{bin}}^{MC,rad}}, \quad (5.11)$$

which should have less statistical uncertainty⁸ [3]. Unfortunately, there remains the possibility that the barred kinematic quantities in Eq. (5.7) differ between cases with and without radiative effects. We expect this effect to be small if the bins in (E_m, p_m) are small, but Fig. 5.2 shows that the two corrections factors are not statistically equivalent for our bin size, nor does the situation improve markedly when the bin sizes are halved in both directions. Accordingly, we choose to define the deradiation factor using the Monte Carlo spectral functions. This choice is not entirely unambiguous because this definition brings the model-dependent uncertainty of the off-shell cross-section into the definition of C_{bin} . However we expect the model-dependence to largely cancel out in the quotient.

5.4.3 Sum Over Kinematics

In some of our kinematic settings, the spectrometers were moved, or the magnets reset after part of the data taking. In some cases this was deliberate (e.g. to scan the Fermi cone in the $Q^2 = 3.3$ GeV data), in other cases it occurred

⁸The spectral functions must be found by the method of Section 5.3.1 which introduces the model dependent uncertainty of the calculation of σ_{ep} , and also counts the statistical fluctuations of each run twice: once for each sum in Eq. (5.8). Using the yields avoids these problems.

because our run-time was not contiguous. In either case, care must be taken to insure that the data is combined in a meaningful way.

We aggregate runs for post-replay analysis only if their kinematic conditions agree to high precision. Once the data has been processed to extract and deradiate the spectral functions, it is independent of the particular kinematics (though possibly dependent on the Q^2 , and clearly dependent on the target nuclei), and may be combined in a straight forward way. We form the error weighted average of all data pertaining to a particular target and Q^2 value on a bin-by-bin basis.

5.5 Spectral Function Integration and Nuclear Transparencies From Spectral Functions

In the absence of final state interactions, and in the limit of full acceptance, we would expect the integral of the spectral function to give Z , the number of protons in the target nucleus. Accepting the untidiness of real physics and our limited analysis region in (E_m, p_m) space, we expect the integral of our data to give $Z * (\text{nuclear opacity})/(\text{correlation correction})$.

In order for this integration to work, we must recall that the spectral functions that we've defined in (E_m, p_m) space actually represent a distribution in a four dimensional (E_m, \vec{p}_m) space, and apply the appropriate Jacobian when integrating the spectral function. This is necessary despite the fact that the data originally occurred in the four dimensional space because the factors related to aggregation of events into scalar p_m bins cancel out in the formation of the ratio in Eq. (5.8).

The measured spectral function is reduced from its vertex value by the nuclear opacity just as the measured yields are, and we can calculate a nuclear

transparency by forming the ratio:

$$T_A^{\text{SF}} = \frac{\int dE_m d\vec{p}_m S^{\text{derad}}}{\int dE_m d\vec{p}_m S^{\text{PWIA}}} \quad (5.12)$$

in exact analogy with Eq. (1.10). This form makes this extractions independent of any normalization problems which may exist in the spectral function extractions procedure.⁹

The correlation correction introduced in Section 4.4.5 (and applied as a multiplicative factor to our data) is dependent on the region in which it is defined. Indeed it represents the same physics as the spectroscopic factor, only defined over a much larger region of (E_m, p_m) space, and given the opposite sense. We note again that deradiation is a redistributive procedure, which moves strength around in the missing energy and momentum space conservatively. This means that the deradiated spectral functions correspond to a set of events from a different region in (E_m, p_m) space than the limits we integrate over. In particular, we draw in events from higher missing energy. Accordingly, we do not expect transparencies found by Eq. (5.12) to have the same value as those found from the yields. However, because the correlation correction is (largely) independent of Q^2 , we expect the point-to-point variation to show the same behavior.

As stated in Section 1.4.2 there are some theoretical reasons to expect that the color transparency may begin sooner in the s-shell than in the p-shell. An examination of Fig. 5.3 reveals that it is still not possible to cleanly resolve the two nuclear shells, however the asymmetry of the mixing has been largely removed. We define ranges of missing energy corresponding to the peaks in the figure which

⁹This is true as long as the PWIA spectral function is extracted by the same procedure as the data spectral functions, which is the case in this analysis.

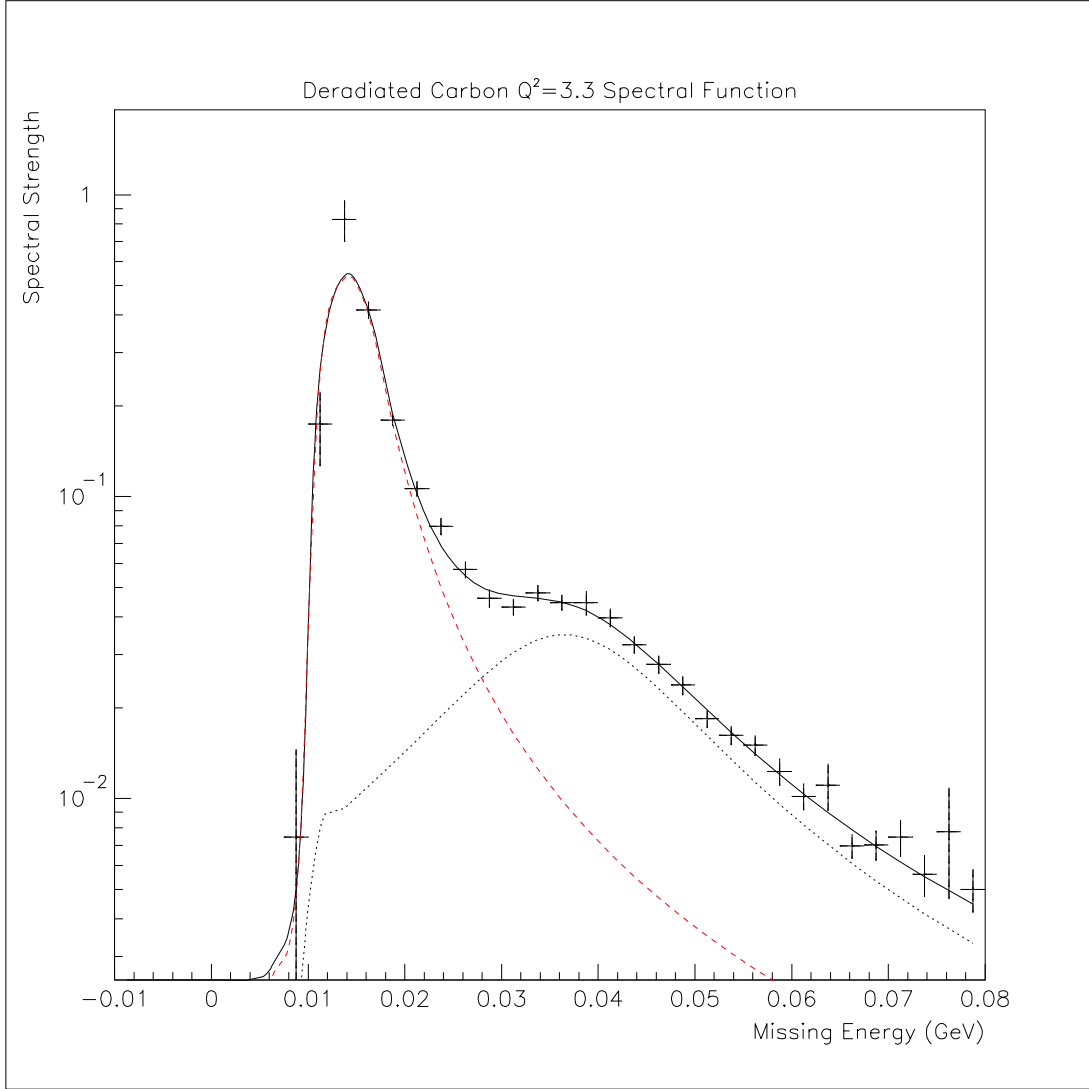


FIG. 5.3: The missing energy dependence of the deradiated spectral function extracted from our data on carbon at $Q^2 = 3.3 \text{ GeV}^2$. The lines represent simple fits and are intended as rough guides only. We fit each peak with a Lorentzian and apply a cutoff at low missing energy. The solid line is the sum of the p-shell (dashed line) and s-shell (dotted line) results, and can be seen to reasonably represent the data. Note the considerable overlap of the shells. Compare with Fig. 5.1.

are “mostly” composed of a single shell, and measure the transparency over that region. The transparency of the p-shell is measure over missing energy values from 15 to 25 MeV; the s-shell from 30 to 50 MeV. Dutta estimates the contamination of each shell by the other is approximately 8% over each of these ranges [3]. Again, the correlation correction will be incorrectly defined over the region we choose for each shell, but we expect the point-to-point behavior to be unaffected.

5.6 Error Analysis

It is usual to divide the sources of experimental uncertainty up into groups which (hopefully) have uniform mathematical properties. In addition to the ubiquitous statistical and systematic errors, we have some uncertainty associated with certain theoretical choices we made in the construction of the model, and an additional problem associated with the fate of our thick iron target.

5.6.1 Melted Target

Our 6% radiation length iron target (target #1) was not fully as wide as the space provided to clamp it into the target ladder (see Section 2.4). This was not thought important by the graduate student supervising the mounting because the clamp held it firmly. However, the heat tolerance for the target had been closely calculated on the assumption that it would be in firm contact with the (water cooled) frame on all four sides.

The target melted. The problem was first noted in hlog entry #13677 on the morning of May 21, but the problem was later ascertained to have begun two and a half days and ≈ 1700 good physics events earlier. The sequence of events is not entirely clear, but it is believed that the melting proceeded very slowly, manifesting first as a bulging of the target in the region of the actual beam spot.

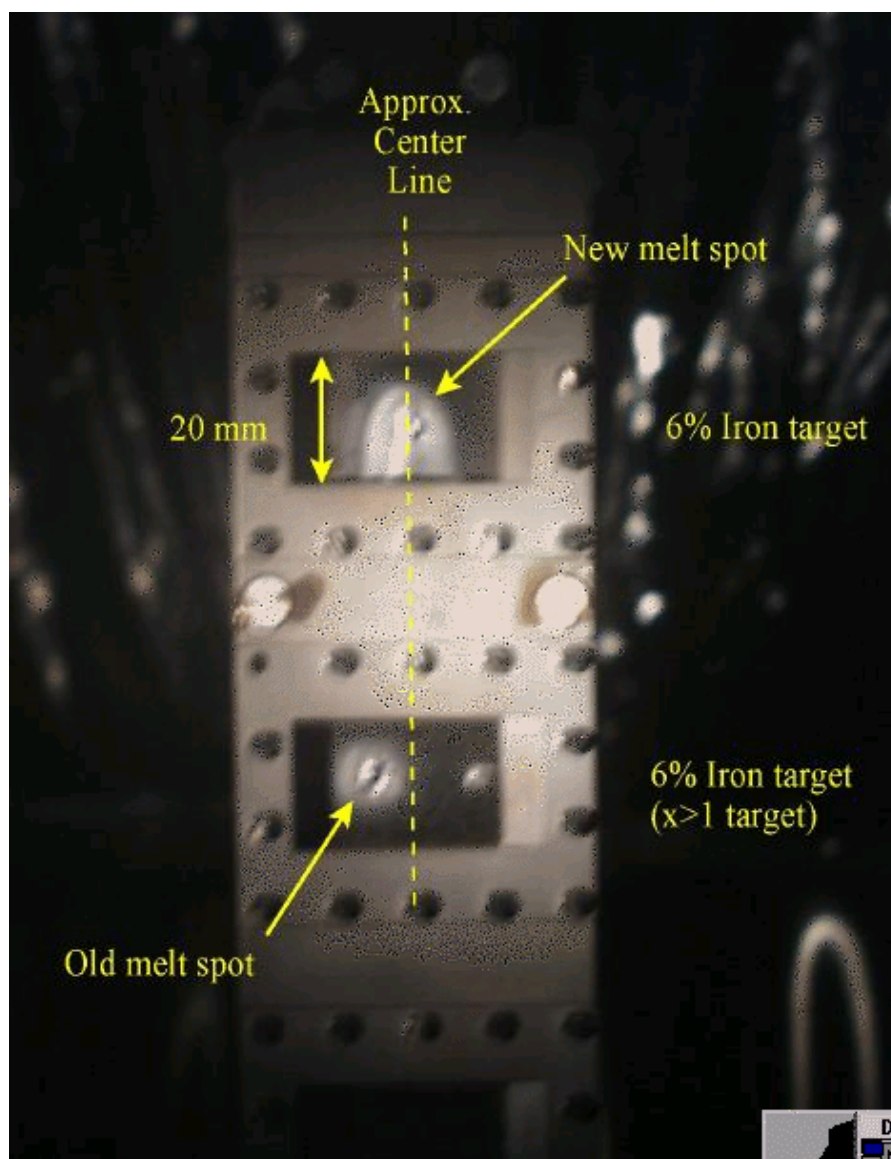


FIG. 5.4: A photograph of the melted iron target. This picture is taken through the view port on the scattering chamber, accounting for the poor lighting and definition. Also visible is the pre-existing meltspot on the 5.8% radiation length target recycled from an earlier Hall C experiment.

This conclusion is supported by evidence from the scaler and coincidence rates, and the visual evidence (see Fig. 5.4). Later the hot bubble seems to have flowed leaving a low areal density region at the point the beam was illuminating. The sudden reduction of yield at this time alerted the shift crew.

We have discarded all data taken on this target from run #25180 onward, and have also assigned an additional systematic error to the iron data taken at $Q^2 = 6.1 \text{ GeV}^2$. See Section 5.6.3. The remaining data constitute our smallest data set, and consideration was given to trying to recover the affected runs by using the spectrometer singles rate to normalize the coincidence rates for the changing target thickness. However, our conclusions do not depend sensitively on this data point, so the idea was shelved.

5.6.2 Statistics

The behavior of errors associated with counting is well understood, and we've used the standard methods to evaluate and propagate these errors. Our run time was divided in an effort to provide at least 3% statistics at all data points, and 2% (1%) statistics for our Fe (H, D, C) data at the lowest momentum transfer. Table 5.3 details how many good events we collected.

5.6.3 Systematic Errors

We subsume into our systematic error all the dependency of our results on beam and spectrometer parameters (beam energy, beam current, magnet excitation, optical matrix elements, etc.) and analysis corrections (trigger and tracking efficiencies, cryo-target density corrections, proton absorption, etc.). Also included in this uncertainty is our increments for the SOS extended target renor-

TABLE 5.3: Actual number of good events taken.

Target \ Q^2 (GeV ²)	3.3	6.1	8.1
Hydrogen	23,235	7,920	1,669
Deuterium	12,646	7,768	2,490
Carbon	30,124	6,928	4,623
Iron	3,612	934	1,171
Dummy	308	101	42

malization applied to the deuterium target, and the iron target melting behavior described in Section 5.6.1.

Most of these have been discussed in earlier sections, and most of them represent uncertainties in measurements, which can be assumed to be independent. We assign a total systematic error of 3.8% to the results for iron at $Q^2 = 6.1$ GeV², 3.0% to all our deuterium results, and 2.3% to the remaining results.

Note that many of the sources of systematic error can be expected to affect the overall normalization of our results, without affecting the point-to-point differences.

5.6.4 Model Dependence

We have noted earlier that the extraction procedure depends on the model used by the simulations (and in the calculation of the inverse cross-sections in Eq. (5.8)).

Pollock attempts to evaluate the model dependence, and finds that it can be quite large under some circumstances [35]. Derek van Westrum reports on some tests performed during the analysis of e91-013 which suggest that the choice

of σ_1^{cc} as opposed to σ_2^{cc} makes a difference of about 1.5% [4]. For the purposes of comparison of experimental results, however, it is sufficient for all the relevant measurements to have been analyzed with the same model. Our choice agrees with that made in e91-013, and NE-18 [3, 4, 14, 15].

6. RESULTS AND CONCLUSIONS

With the data taken, reduced, simulated, corrected, analyzed, and understood, we are finally ready to present the results.

6.1 Transparency Results

The results presented in this section are those published in our paper: Ref. [78]. We summarize here for completeness.

The results of mapping the Fermi cones of carbon and iron at the lowest Q^2 point are summarized in Fig. 6.1. Our data (filled symbols) can be seen to be consistent in yield (upper panel) and transparency (lower panel) with both the predictions of the Monte Carlo (solid lines in the upper panel), and the earlier Hall C experiment (open symbols). Further our measured transparencies at the quasi-free angle agree with the statistically averaged transparency (solid line in the lower panel). The large asymmetries about the quasi-free angle noted at lower Q^2 in the earlier experiment [25] are greatly reduced, suggesting that the reaction mechanism is better understood at these Q^2 values.

Table 6.1 exhibits our nuclear transparency results as quoted in Ref. [78]. The striking feature of the data is the substantial lack of any Q^2 dependence. For all three nuclei studied, the data can be reasonably fit with constant values [78].

TABLE 6.1: Measured nuclear transparencies for D, C, and Fe. The uncertainties include statistical and systematic uncertainties, but do not include model-dependent systematic uncertainties in the simulations.

Q^2 (GeV/c) ²	T_D	T_C	T_{Fe}
3.3	0.897±0.030	0.548±0.014	0.394±0.013
6.1	0.917±0.031	0.570±0.015	0.454±0.023
8.1	0.867±0.032	0.573±0.016	0.391±0.015

TABLE 6.2: Results of the fits to the A-dependence. Please note that the values quoted for σ_{eff} follow the framework of [79], and numerical values differ slightly from those quoted in [16, 23].

Q^2 (GeV/c) ²	Ref.	α	σ_{eff} (mb)
0.3	[27] (Bates)	-0.22 ± 0.03	16 ± 3
0.6	[25] (JLab)	-0.17 ± 0.04	24 ± 3
1.0	[16, 23] (SLAC)	-0.18 ± 0.02	21 ± 3
1.3	[25] (JLab)	-0.22 ± 0.05	26 ± 2
1.8	[25] (JLab)	-0.24 ± 0.04	30 ± 2
3.1	[16, 23] (SLAC)	-0.24 ± 0.02	28 ± 4
3.3	[25] (JLab)	-0.25 ± 0.05	29 ± 2
3.3	present work	-0.24 ± 0.02	32 ± 2
5.0	[16, 23] (SLAC)	-0.24 ± 0.02	30 ± 5
6.1	present work	-0.24 ± 0.03	29 ± 4
6.8	[16, 23] (SLAC)	-0.20 ± 0.02	24 ± 3
8.1	present work	-0.23 ± 0.02	31 ± 2

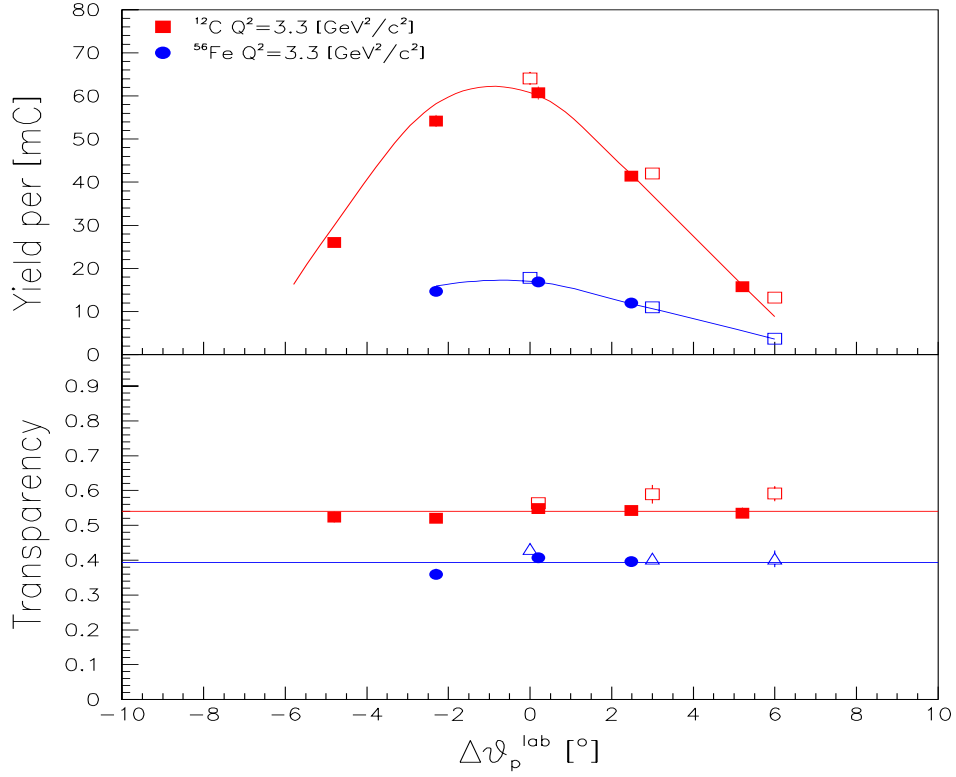


FIG. 6.1: Experimental (e,e'p) coincidence yields and transparency as function of proton angle. (Upper panel) Experimental (e,e'p) coincidence yields vs. the difference between the proton spectrometer lab angle and the conjugate angle for data from $^{12}\text{C}(\text{e},\text{e}'\text{p})$ and $^{56}\text{Fe}(\text{e},\text{e}'\text{p})$ at $Q^2 = 3.3 \text{ (GeV/c)}^2$. Closed (open) symbols are for the present experiment (for the data from Ref. [25]). (Lower panel) Transparency as function of proton angle for the same data. The curves in each panel are simulations of the yield based on the model described in the text and normalized by a single Transparency factor.

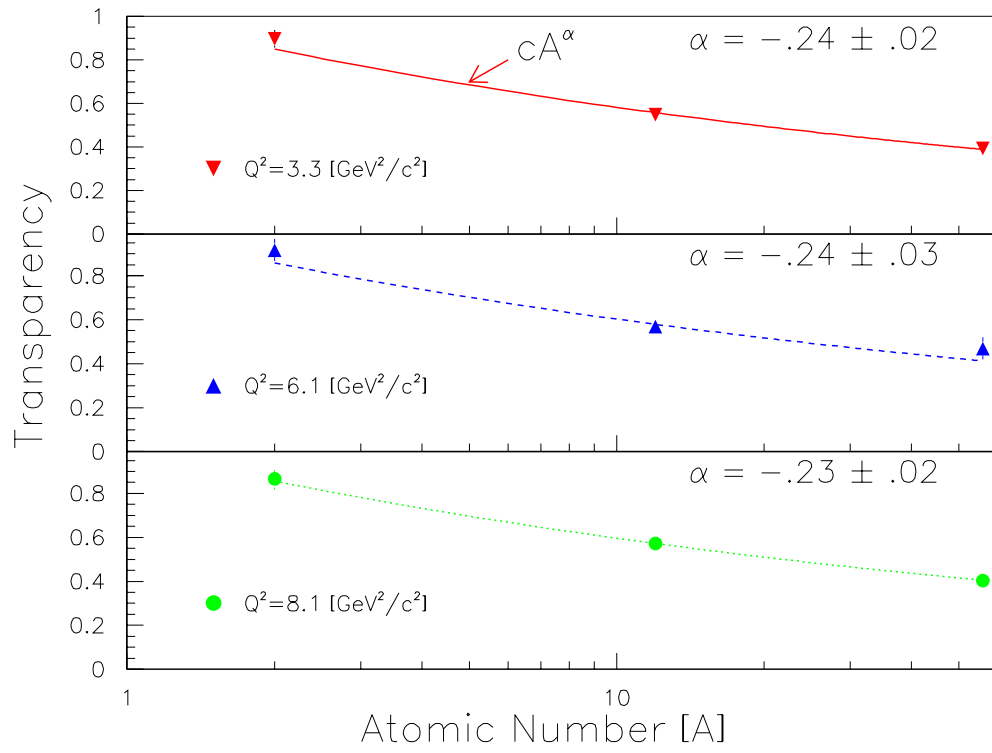


FIG. 6.2: Nuclear Transparency as a function of A at $Q^2 = 3.3, 6.1,$ and 8.1 (GeV/c)^2 . The curves are fits to the D, C, and Fe data using $T = cA^\alpha$.

6.1.1 A-Dependence

We consider the nuclear transparency T as a function of nuclear mass A . Figure 6.2 shows the results of fitting our data at each Q^2 value with the empirical function $T = cA^{\alpha(Q^2)}$. The results of this fit are also displayed in Table 6.2 along with values generated by fitting the results of other experiments to the same function. It is evident that above $Q^2 \approx 1.8 \text{ GeV}^2$ the world data settles into a nearly constant value of $\alpha = 0.24$. Also given in Table 6.2 are the effective proton-nucleon cross-sections derived for these experiments from a classical model characterized by the expression:

$$T_{\text{class}} = \frac{1}{Z} \int d^3r \rho_Z(\vec{r}) \exp \left[- \int dz' \sigma_{\text{eff}} \rho_{A-1}(\vec{r}') \right]. \quad (6.1)$$

The details of this calculation can be found in Ref. [78]. Again, above $Q^2 \approx 1.8 \text{ GeV}^2$ the data are nearly constant.

6.1.2 Q^2 -Dependence

We have observed no significant Q^2 dependence in the nuclear transparencies, fits of the parameter α , or the effective proton-nucleon cross-section derived from a classical model of the FSIs. Recall that the measured transparencies include two effects—the loss of protons to hard FSIs and the reduction of spectral strength in the analysis region by short range correlations.¹ It is conceivable that a falling value for the spectroscopic factor coincident with the onset of color transparency could show no significant trend in the measured nuclear transparencies. However, there is no theoretical work to suggest that this is the case.

¹Represented by the spectroscopic factor or the correlation correction, which is assumed to be a constant in our analysis.

TABLE 6.3: Statistical comparisons of $^{12}\text{C}(e,e'p)$ data with various model calculations. The first model is a Glauber calculation only, the alternative models incorporate Color Transparency effects. We also added entries assuming a floating normalization in these models, to take into account uncertainties both in assumptions made in the Glauber calculations and in the analysis.

Ref.	Normalization	$\chi^2/\text{d.f.}$	conf. level
[80] (Glauber)	Fixed	0.84	55%
[81] (Glauber)	Fixed	1.82	9%
[81] (+ CT)	Fixed	9.4	<0.1%
	Floating	4.0	<0.1%
[29] (+ CT)	Fixed	10.1	<0.1%
	Floating	1.87	9%
[82] (+ CT)	Fixed	7.8	<0.1%
	Floating	0.86	52%
[83] (+ CT)	Fixed	7.4	<0.1%
	Floating	8.4	<0.1%

Making the assumption that color transparency is not present, the constancy of the nuclear transparencies suggest that the quasi-free electron-proton cross-section equals the theoretical cross-section used in the analysis (that is the free electron-proton cross-section corrected for off-shell effects as prescribed in Ref. [34]) [78].

Figure 6.3 exhibits our data as part of the world data set on nuclear transparency in $A(e,e'p)$ experiments [29, 80, 81, 82, 83].

Figure 6.4 and Table 6.3 compare our ^{12}C results with some recent theoretical calculations of the nuclear transparency in this kinematic regime. It is

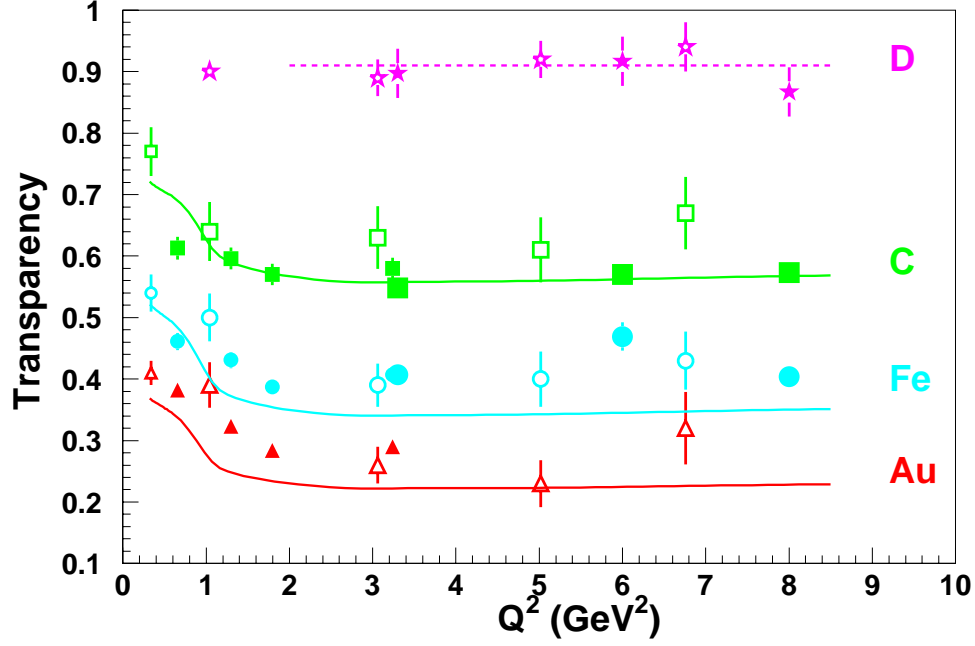


FIG. 6.3: Transparency for (e,e'p) quasielastic scattering from D (stars), C (squares), Fe (circles), and Au (triangles). Data from the present work are the large solid symbols. Previous JLab data (small solid symbols) are from Ref. [25]. Previous SLAC data (large open symbols) are from Ref. [16, 23]. Previous Carroll data (small open symbols) at the lowest Q^2 on C, Ni, and Ta targets, respectively, are from Ref. [22]. The errors shown include statistical and systematic ($\pm 3.2\%$) uncertainties, but do not include model-dependent systematic uncertainties on the simulations. The solid curves shown from $0.2 < Q^2 < 8.5$ (GeV/c)² are Glauber calculations [8]. The dashed curve shown is a one-parameter fit to the D data for $2 < Q^2 < 8.5$ (GeV/c)², with a fit value of 0.91.

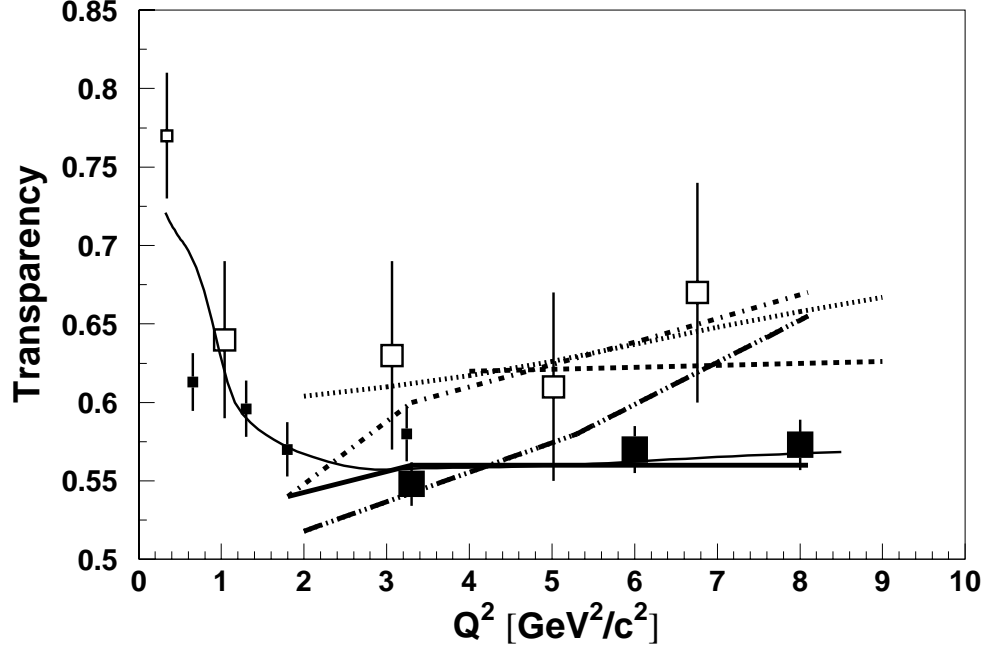


FIG. 6.4: Nuclear Transparency for $^{12}\text{C}(e,e'p)$ quasielastic scattering. Symbols and thin solid curve are identical to Fig. 6.3. The errors shown include statistical and the point-to-point systematic ($\pm 2.3\%$) uncertainties, but do not include model-dependent systematic uncertainties on the simulations or normalization-type errors. The net systematic error, consisting of point-to-point, normalization-type and model-dependent errors, is estimated to be ($\pm 4.6\%$). The error bars for the previous data sets [16, 23, 27] include their net systematic and statistical errors. The thick solid curve is a Glauber calculation of Ref. [81]. The dot-dashed, dotted, dashed, and dot-dot-dash curves are Color Transparency predictions from Refs. [81], [29], [82], and [83], respectively.

evident that our data are not in agreement with any of these models, and rule out any significant color transparency effects up to $Q^2 = 8.1 \text{ GeV}^2$ [78].

6.2 Deradiated Spectral Functions

The spectral functions used and measured in this work are two dimensional objects that vary by more than two orders of magnitude in the region studied, and exhibit (for nuclei with $A > 2$) several interesting structures in that space. In this raw form they are difficult to present, and compare. The usual method used in the past to digest this complexity and present it in a comprehensible form is to integrate each spectral function separately over missing energy and momentum, and present the two projections. The integration over missing momentum should be done with a spherical Jacobian as described in Section 5.5. Figure 6.5 shows an examples of both the two dimensional data, and the projected data for one data point.

Figures 6.6 and 6.7 exhibit our resulting spectral functions for carbon at all values of Q^2 . The data are plotted with the same results extracted from our Monte Carlo output as a means of comparison with theory. Recall from Section 4.2 that inputs to the model were generated by fitting IPSM calculations to existing data. Our results agree in their overall shape with the input models.

In missing energy, we see four interesting features in these spectral functions: the sharp cutoff at the Fermi energy, two peaks related to the nuclear shells, and the high missing energy tail. Agreement on the Fermi energy is essentially guaranteed by the deradiation procedure,² and we can draw no conclusions from

²The deradiation factor, C , is generated entirely from Monte Carlo results, which are (by construction) zero above the Fermi energy.

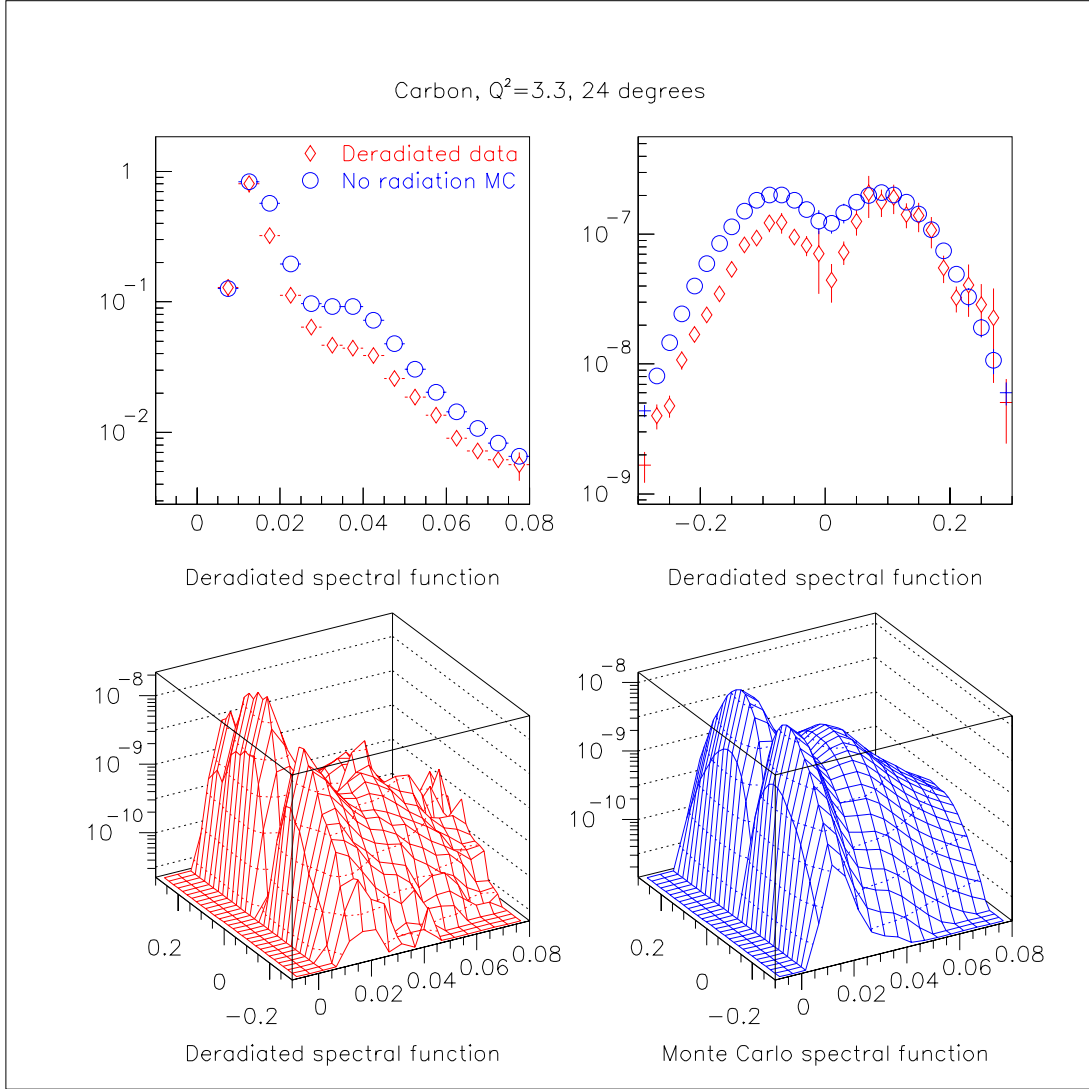


FIG. 6.5: An example deradiated spectral function. The data is shown with both wire-frame and projected views. This sample is presented with fewer and larger bins than used in the analysis for clarity. The diamond markers, and the lower-left wire-frame represent the deradiated spectral function of our data. The circles and the lower-right wire-frame represent a spectral function derived from the simulation with radiative effects disabled. The error bars shown in the projected graphs are purely statistical.

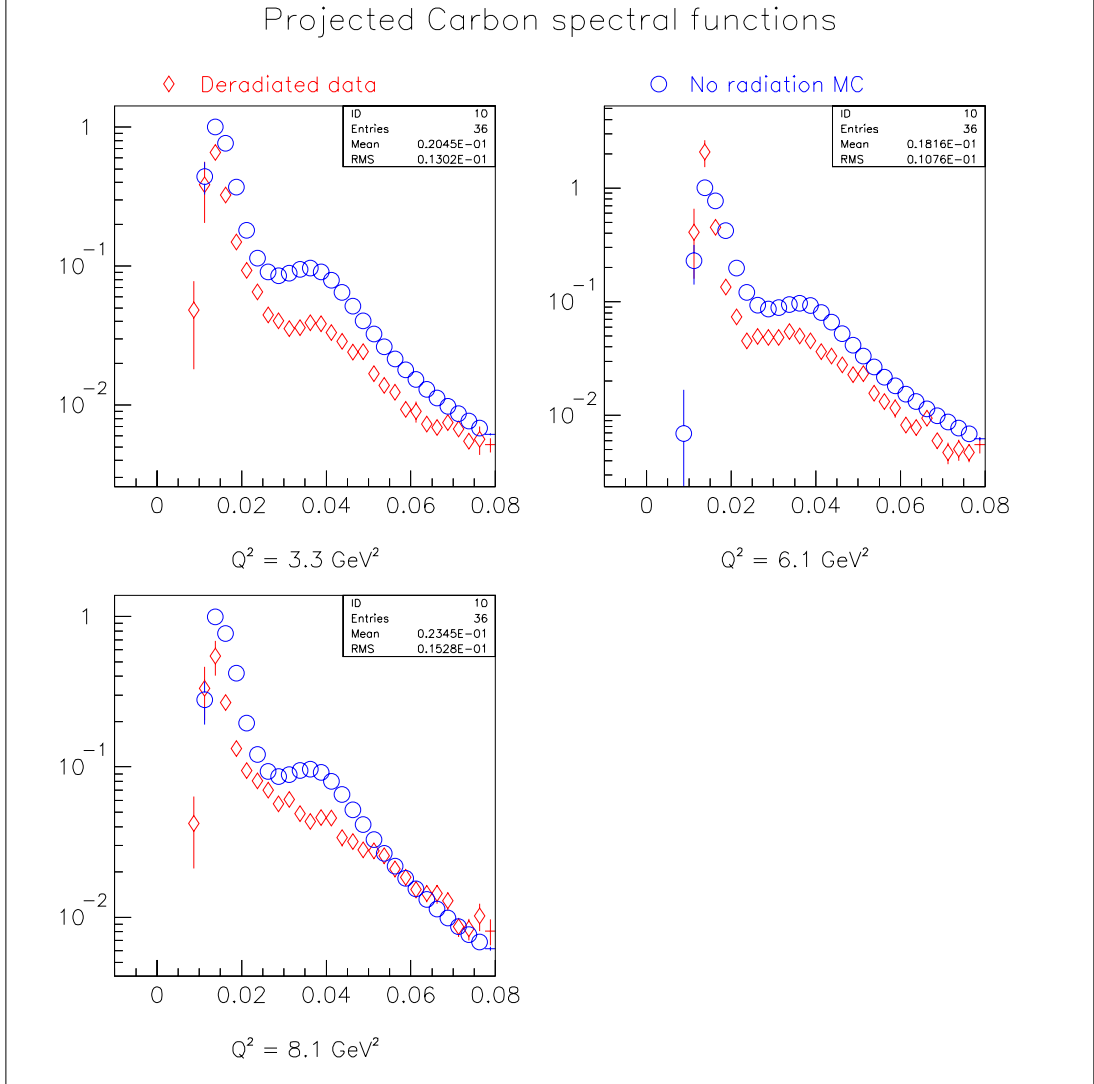


FIG. 6.6: Deradiated carbon spectral function versus missing energy. The Monte Carlo data (circles) are displayed with their natural normalization, so the nuclear opacity is evident to the eye.

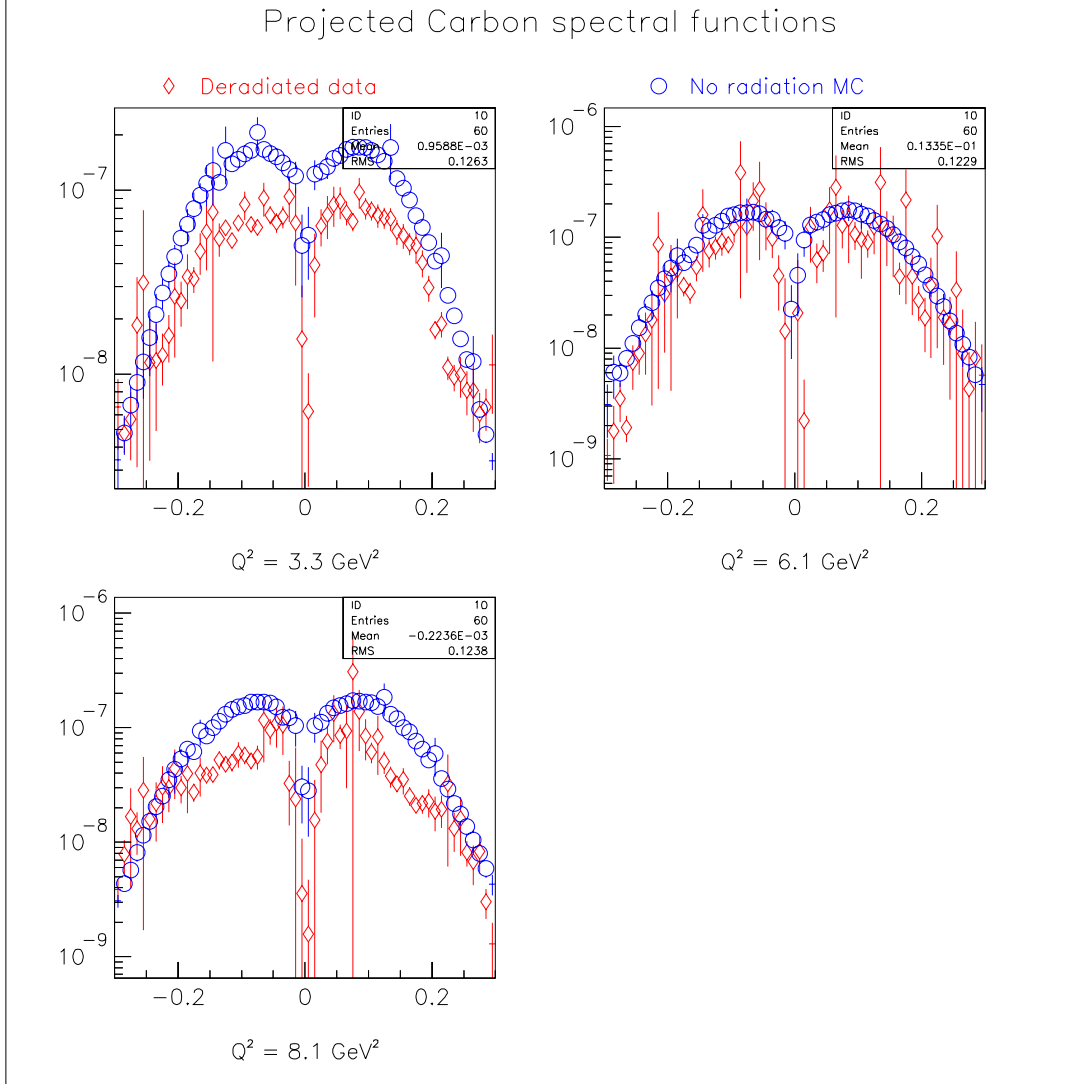


FIG. 6.7: Deradiated carbon spectral function versus missing momentum. The Monte Carlo data (circles) are displayed with their natural normalization, so the nuclear opacity is evident to the eye.

it. At our lower Q^2 values, we have material agreement with the model for both nuclear shells and the high missing energy tail.

At the highest Q^2 values, we still see a good p-shell, but the s-shell can not be cleanly discerned above the background, and our high missing energy tail is more pronounced than in the theory.

Viewed against missing momentum the principle features of the spectral function are bilateral symmetry, the non-zero central value, and the visible peak around ± 100 MeV. The symmetry is a consequence of the resolution of the scalar missing energy into positive and negative values as described in Section 1.3. Our input spectral functions are completely symmetric by construction—a feature not necessarily present in the data. Indeed an asymmetry was noted in e91-013 [3]. This is the same asymmetry exhibited in Fig. 6.1. A very small asymmetry is visible in our lowest Q^2 data only.

The peak at ± 100 MeV corresponds to the nuclear p-shell, which has a minimum at $p_m = 0$, but the s-shell has its maximum at the same value, and fills the central dip, though the integrating Jacobian causes the center-most bins to have very small values. Again, our data are in good agreement with the model at our lower Q^2 values, but we observe some structural differences in the highest Q^2 data.

Figures 6.8 and 6.9 exhibit our resulting spectral functions for iron at all values of Q^2 . The data are plotted with the same results extracted from our Monte Carlo output as a means of comparison with theory. Recall from Section 4.2 that inputs to the model were generated by fitting IPSM calculations to existing data. Our results agree in their overall shape with the input models.

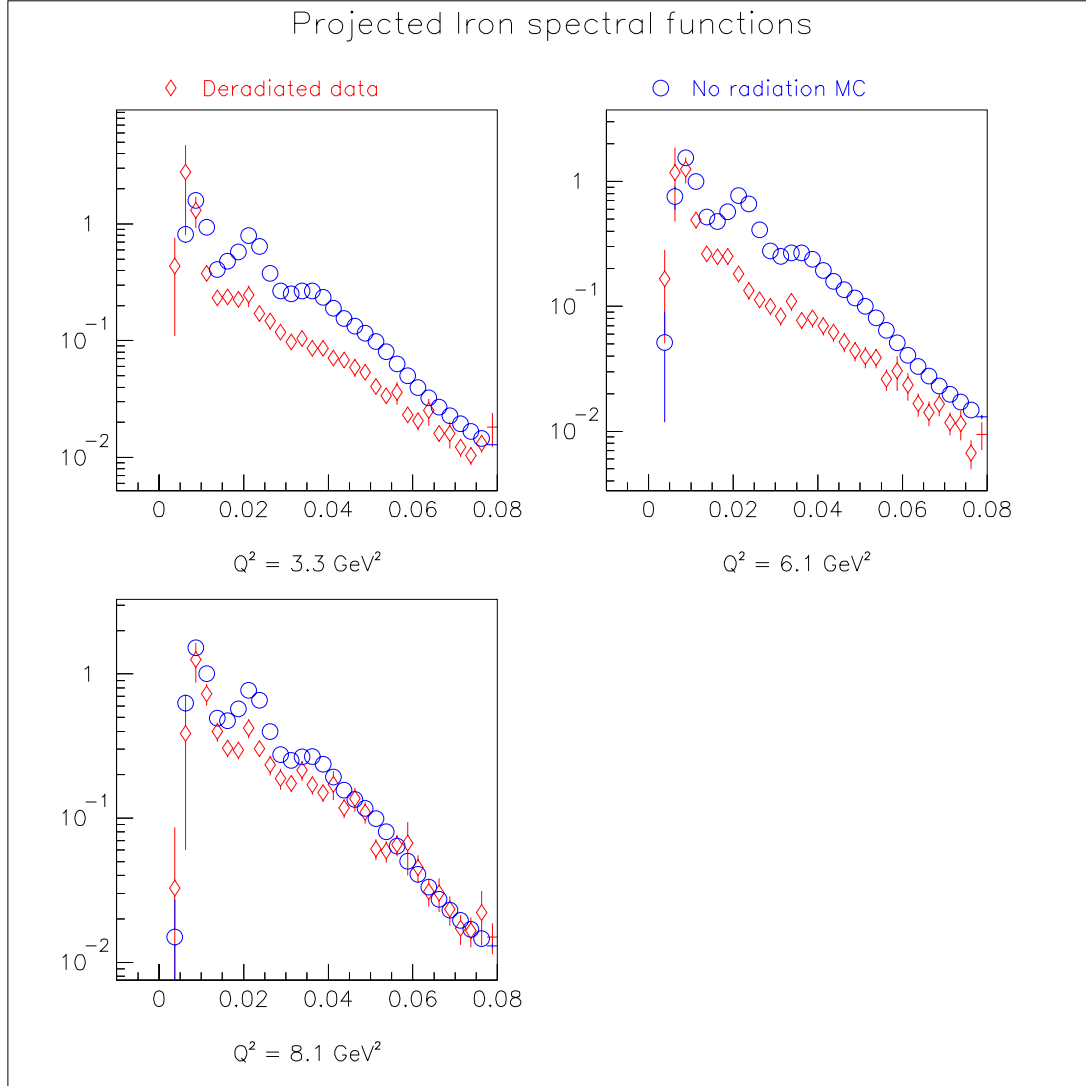


FIG. 6.8: Deradiated iron spectral function versus missing energy. The Monte Carlo data (circles) are displayed with their natural normalization, so the nuclear opacity is evident to the eye.

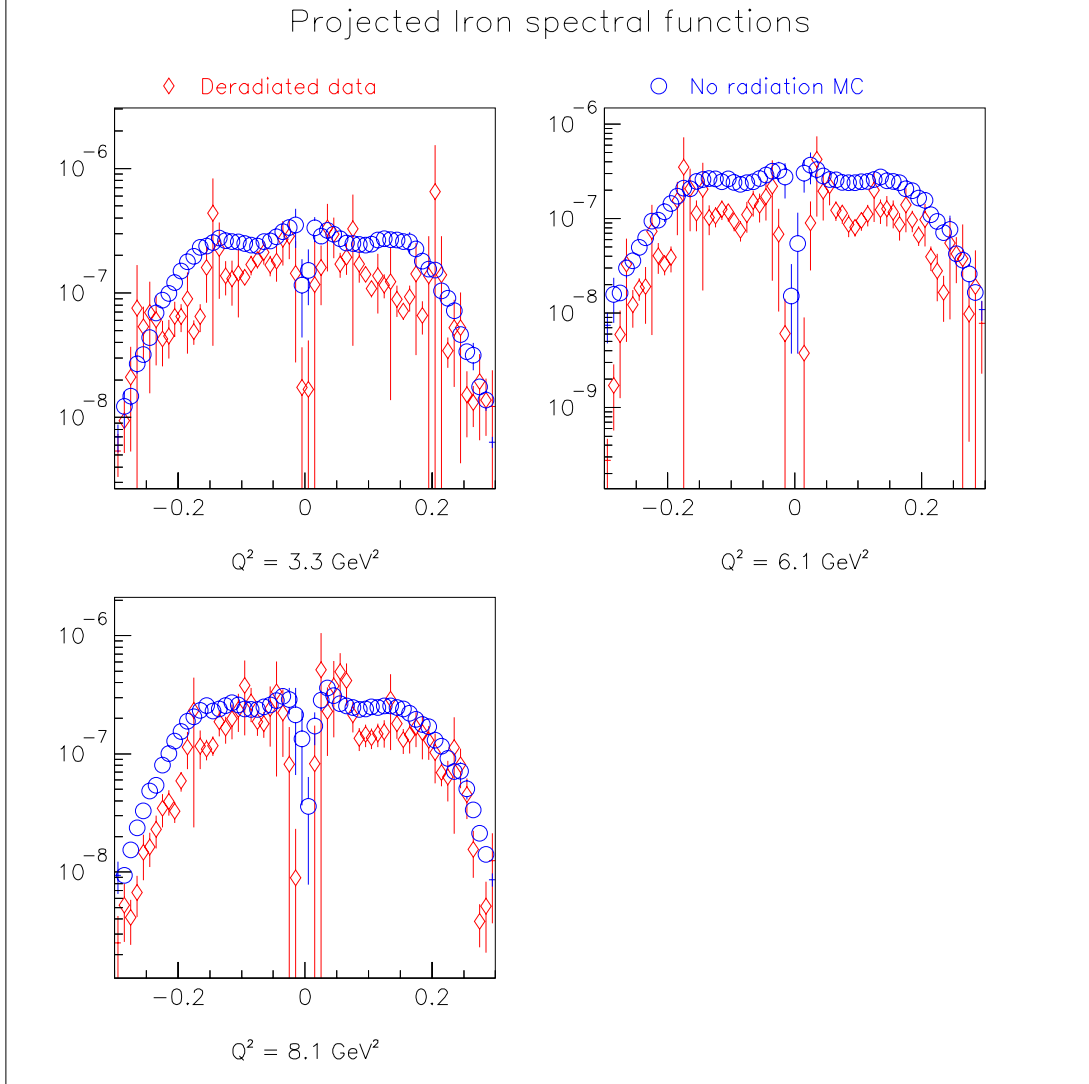


FIG. 6.9: Deradiated iron spectral function versus missing momentum. The Monte Carlo data (circles) are displayed with their natural normalization, so the nuclear opacity is evident to the eye.

The spectral function of iron is more complicated, and less well defined than that of carbon. Indeed it wasn't possible to fit all the shells individually when the model spectral functions were constructed [14]. Still, we have passable agreement in shape with the model.

6.3 Future Work and Conclusions

Our central physics conclusion is that we see no evidence for the onset of color transparency up to $Q^2 = 8.1 \text{ GeV}^2$. In fact this does not come as much of a surprise: between the initial proposal to pursue this measurement, and the beginning of our beam time, theoretical progress had made it seem less likely that we would be able to observe any effect. It has become clear that several processes can complicate the transparency signal for squared momentum transfer values between 1 and 10 GeV^2 [18, 81], and the onset of color transparency effects is now predicted to occur slowly rather than suddenly, first obtaining measurable magnitude around $Q^2 \approx 20 \text{ GeV}^2$ for carbon [11, 17, 18, 19].

We should emphasize that if QCD is a gauge theory, a transition from nucleonic degrees of freedom to partonic degrees of freedom, and the consequent reduction in final state interactions is guaranteed with increasing Q^2 [11]. Early quantitative work on color transparency focused mostly on DWIA and Glauber calculations with a variety of physically meaningful models of the \mathbf{q} and time dependence of the FSIs [83, 84]. These models admit a wide range of predictions for the onset of color transparency, including very precocious onsets. Methods developed in the early and mid 1990s, especially those based on diffractive scattering methods, began to allow successful prediction of color transparency behavior in meson production reactions [11, 18]. Those same theoretical methods predict a

slow onset in proton knock-out systems becoming accessible somewhat above our highest Q^2 [11, 18, 81].

There is still work that can be done with *this* data. In particular, our procedure requires a model spectral function as an input, and returns a spectral function as the output. An iterative procedure should be able to generate self-consistent spectral functions [3]: that is, one which if used as the input to our procedure results in an fully equivalent output.

Theoretical work to better understand other physics that affect the measured nuclear transparency in quasielastic electron scattering would be valuable in seeking to observe a possible slow onset of color transparency effects. Currently this could be achieved only with high quality data over a very wide range in Q^2 because other nuclear physics effects (such as the correlation correction, and the off-shell nucleon cross-section) are only known to a few percent [78].

Further studies of color transparency in quasielastic electron scattering are possible. Indeed, a higher Q^2 measurement in search of color transparency effects is one of the arguments in favor of the proposed 12 GeV upgrade to the CEBAF accelerator [85]. An upgraded Hall C could pursue this measurement to Q^2 values of 18 GeV² or more.

APPENDICES

APPENDIX A

SOLID TARGET THICKNESS

We measured the areal density of our solid targets, and estimated the associated uncertainties. With standards available on site we can determine the average areal density, ρt , to about .15%. If the target is uniform (i.e., no voids, or thickness or density variations) then this will be the density sampled by the rastered beam spot (called ρt_{spot}). We made an attempt to measure the real thickness variations present in the targets, and to assign a meaningful additional error to ρt_{spot} ¹

A.1 Equipment Used

List of the equipment used as primary standards:

- Ohaus Analytical Standard Balance AS60, located in Dave Mack's office.
- Mitutoyo Toolmaker's Microscope with digital encoder, located in Survey and Alignment Group's office.

¹This document modified from the 1997 document on the same subject by D. Mack and J. Volmer [86].

List of the equipment used as secondary standards:

- Ohaus Metric Mass set, 1 mg to 50 g, located in Dave Mack’s office.
- Mitutoyo digital calipers, “Absolute Digimatic” model. Borrowed from the Detector Meisters in EEL 126.
- Micrometer Caliper, L.S. Starrett Co. Borrowed from the Detector Meister in EEL 126.

The equipment is easy to use. To make mass measurements with the analytic balance, turn the scale on, wait, zero the scale with the door closed, then open the door to put your sample on the scale, then close the door. Closing the door keeps out air currents and makes the level reproducible. Re-zero if you have to move the scale since small changes in level will occur. Long- and short-term reproducibility of ± 1 mg (random error only!) is routine.

Reproducibility in determining a target length with the Toolmaker’s microscope is at the few micron level. Resolution of the hand-held Mitutoyo calipers is 10 microns and reproducibility is also of this order. Accuracy is about 20 microns according to the vendor’s literature.

A.2 Areal Densities

We chose to determine the average density, ρt , of the targets by measuring the target mass, and the projected area in the beam direction. We then calculate $\rho t = \text{mass}/\text{area}$. Assuming a uniform target, this method is sufficiently accurate for the present measurement. This technique should yield an error an order of magnitude smaller than if we had measured t directly and used a standard value for the density to determine ρt .

A.2.1 Area

Though the targets are nominally rectangles, this is not true at the required precision: the diagonals of the targets measured for e94-139 differed by as much as 2%—a rough measure of the deviation from rectangularity.² The area of an arbitrary quadrilateral ABCD may be found by this simple prescription:

1. Measure the x - y position of each of the four corners. Zero the microscope at the lower-left corner, and measured around the perimeter in a counter-clockwise direction, finishing at the starting point to ascertain the reproducibility of the measurement.
2. Calculate the length of all four sides AB, BC, CD, and DA, as well as one of the diagonals—say AC.
3. The area of an arbitrary triangle with side u , v , and w can be found by the Method of Heron.

$$\text{Area} = \sqrt{s(s-u)(s-v)(s-w)}$$

where s is the semi-perimeter: $s = \frac{1}{2}(u + v + w)$.

The two triangles together give the area of the whole quadrilateral.

The position measurements for the e94-139 targets can be found in Table A.1.

The edges of the iron targets as could be seen to be beveled under the microscope.

The width of the bevel was several times the precession on the instrument. If the

²Some of the corners of the iron targets deviated visibly from square under the magnification provided by the microscope, however the “missing” area total at most a few times 10^4mm^2 on any target, and can be neglected.

TABLE A.1: Positions of the corners of each target. The area measurement is independent of orientation, so no special attempt was made to get the targets square on the table. Measurement began with the lower-left corner, and proceed counter-clockwise, returning to the start to assess the reproducibility of the measurements. All measurements in mm with a uncertainty of $\pm.01\text{mm}$ in both directions.

Target	axis	lower-left (origin)	lower-right	upper-right	upper-left	lower-left
thin Fe	x	0.0	37.784	38.304	0.459	-0.009
	y	0.0	-0.963	18.051	19.029	0.018
thick Fe	x	0.0	37.938	38.242	0.309	-0.001
	y	0.0	-0.775	18.221	18.836	-0.026
C	x	0.0	38.096	38.261	0.177	0.007
	y	0.0	-0.329	18.724	19.042	-0.013

bevel is uniform, treating the center of the slope as the “edge” will return the correct average density. This is what was done.

A.2.2 Mass

Measuring the mass of the targets on the analytic balance was a straightforward exercise. We also took some calibration data on a standard weight set. See Section A.4

A.2.3 Results

The areal densities, masses, and thickness (in radiation lengths) of the targets are shown in Table A.2. All targets were evidently cut to a nominal 1.5 in by .75 in, and their areas span a range of roughly only 1%. This suggests

TABLE A.2: Measured areal densities of solid targets. Final relative errors on the average ρt are .15%. There is an additional error of ρt_{spot} which must be added in quadrature to account for local variations in target thickness.

Target	Mass (<i>g</i>)	Area (<i>cm</i>)	ρt (<i>g/cm</i> ²)	λ (%)
thin Fe	2.5844	7.1955	0.3592	1.8%
thick Fe	6.0052	7.1805	0.8363	0.5%
C	9.0374	7.2566	1.2454	0.6%

TABLE A.3: Comparison of measured solid target densities with standard values. Standard values taken from the Particle Physics Booklet [87]. The trend towards low densities seen previously [86] and attributed to over-measurement of the thickness is not present.

Target	Mass (<i>g</i>)	Area (<i>cm</i>)	Thickness (<i>cm</i>)	ρ (<i>g/cm</i> ³)	ρ (PPB [87])	Error (%)
thin Fe	2.5844	7.1955	0.0447	8.04	7.87	+2
thick Fe	6.0052	7.1805	0.1036	8.07	7.87	+3
C	9.0374	7.2566	0.5672	2.19	2.265	-3

there are no major screw-ups in our area measurements. A further cross-check is possible by measuring the thickness, calculating the density, and comparing this to the standard value. The thickness measurements were made with a vernier micrometer borrowed from Dave Mack. This results are found in Table A.3.

Our calculated densities are similar to those given for C and Fe in the Particle Physics Booklet [87]. We expected the jaws of the micrometer to rest on surface imperfections and bias the thickness measurement to larger values, but this effect is not manifestly present.

A.3 Error Analysis

Our estimate for the absolute accuracy of the weight measurements is .1%. (See Section A.4) This is a systematic error in the sense that the target will be consistently high or low forever. The random error (i.e., reproducibility) is on the order of .005% and we ignore it henceforth.

Our estimate for the absolute accuracy of the length measurements is conservatively taken to be .1%. (See Section A.4) The random error (i.e., reproducibility) in measuring a length was of order .01% and we ignore it henceforth. We further conservatively assume that the errors are correlated in calculation of the area.

The overall error for the average ρt is then calculated as follows:

$$\rho t = mass/area$$

$$\frac{\Delta(\rho t)}{\rho t} = \sqrt{(\Delta mass/mass)^2 + (\Delta area/area)^2}$$

$$\Delta mass/mass = .001$$

$$\Delta area/area = .001$$

so finally,

$$\frac{\Delta(\rho t)}{\rho t} = .0015.$$

An additional error must be added in quadrature to take into account the presence of non-uniformities in thickness. (See Section A.4)

A.4 Systematic Studies

General systematic concerns include the accuracy of the instruments, the difference between the average density of the target, and the sampled density. Another concern is the contribution to the target weight due to volatiles, such as water, adsorbed on the surface. Dave Mack studied this possibility in his 1997 write-up [86], and concluded that it was small enough to be ignored.

A.4.1 Accuracy of Instruments

We first checked the accuracy of the standard balance using a set of weights. The results are found in Table A.4. Reproducibility of the measurements is characterized by the scale's readings -0.2 mg after the both sequences

TABLE A.4: Comparison of nominal weight values with measurements by the analytical balance. The agreement in the range 1-10 grams is most relevant for our targets.

nominal value (g)	measurement (g)	Relative Error %
.200(a)	0.2003	+0.15
.200(b)	0.1995	-0.25
.500	0.4988	-0.26
1.000	1.0011	+0.11
2.000(a)	2.00015	+0.0075
2.000(b)	2.0023	+0.115
5.000	5.0036	+0.072
10.000	10.0119	+0.119
20.000(a)	19.9975	-0.0125
20.000(b)	19.9970	-0.015
Average		0.0036
Std. Dev.		0.140

of measurements (the standard weights, and the targets) despite being zeroed at the start of each sequence.

We can get a crude idea of the absolute accuracy of the scale measurements by measuring standard weights. In the mass range of the targets we were given, 1-10 grams, a good estimate for the absolute accuracy appears to be .1%. Since two standard weights of the same nominal mass differed by .1% the scale might be more accurate than the weights themselves. Note that the analytical balance and the weight set both came from the same vendor, Ohaus, which is not the ideal way to do such a cross-check.

A crude estimate for the absolute error of the length measurements was obtained by re-measuring the thick Fe target with a hand-held Mitutoyo digital

TABLE A.5: Point-to-point thickness variation of solid targets. Summary of eleven micrometer measurements of the target thicknesses. Average and standard deviations are shown. Instrument error on the averages is 0.017 mm. The relative error provides a crude approximations of the sampling uncertainty that should be applied to ρt_{spot}

Target	Thickness (mm)	Relative Error
Thin Fe	0.4447 ± 0.0078	1.7%
Thick Fe	1.0356 ± 0.0049	0.5%
C	5.672 ± 0.035	0.6%

micrometer. (Again, having the primary and secondary standards come from the same vendor is not the ideal way to do things.) The measurements agreed at the .05% level. We have conservatively assigned an error of .1% to the length measurements.

A.4.2 Point-to-point Variation

The beam spot will sample a disk-like area of the target with an inner diameter of approximately 0.5mm, and outer diameter approximately 1.0mm. Although we are able to determine the average ρt of the 1.5 in by .75 in targets to much better than 1%, it would be nice to confirm that the areal density at the beam spot, ρt_{spot} , was known to the same or better accuracy.

Using a hand-held micrometer, we can see reproducible variations in thickness at the .1 mil level (i.e., .0001 inch or 2.54 microns). The targets were sampled at 11 points (roughly equally spaced over the whole area of the targets). The results of these measurements are summarized in Table A.5.

The thick C target showed very little variation, with the highest and lowest points differing by only .1 mil (.25%). The thick Fe target showed a systematic change in thickness from one end to another, the variation being about $\pm .1$ mil ($\pm .25\%$). For both thick targets the average value of ρt in Table A.2 should accurately reflect ρt_{spot} . However, since we are only able to check nonuniformity at the .1 mil level, we conservatively assume an additional error of .25% for ρt_{spot} for the thick targets.

APPENDIX B

TOOL CHAINS AND CORRECT PROCEDURE

The analysis of e94-139 data relies on a fairly extensive chain of computer programs, and requires extensive human (i.e. hopefully intelligent) intervention to get from here to there. Section 2.7 surveys the data acquisition electronics, and alludes to the CODA software which turns the signals into a raw data file; Chapter 3 discusses the the Replay analyzer which reduces the raw data to individual events and their associated physics quantities; Chapter 4 talks about the simulation. All of these programs are part of the standard Hall C package, and are well tested and fairly reliable. At least, their bugs and limitations are understood.

Chapter 5 sees the development of a mathematical framework for the further analysis of real data and Monte Carlo results in the form of bin-by-bin calculations to extract and deradiate the spectral function. The actual work is accomplished by a considerable pile of custom code written in four languages.

Approximately four. Various tools are written in awk, sh, KUIP (the HBOOK and PAW scripting language), and Fortran. Most of the Fortran is stand alone code that relies heavily on the HBOOK libraries, but a few routines

are intended to be invoked by a kumac (a KUIP script), and run in the COMIS Fortran interpreter that is part of CERNLIB. Additionally, some of the stand alone Fortran programs parse custom input files¹ which are mostly generated programmatically by awk scripts.

All of these complicated doings, by all of this custom code *should* leave the alert reader with some question about the correctness of the code. Indeed early version of the tool chain had several fatal errors, and substantial portions of the work were redone from the ground up on two occasions.

B.1 Where the Information Is

The raw information about what data was taken under what conditions comes from the run-info events in the log file headers, and from the Hall C Online Log book. The DAQ software automatically enters each run in the log book as it is started, including a summary of the kinematic measurements that go into the run-info event, and an arbitrary text set by the operator—usually containing some identifying information. Additionally, the run operators log any unusual events or observations, and a shift summary is entered three times a day.

When, as occasionally happens, there is some doubt that the information in the log book is correct, the run can be analyzed using the presumptive information, and checked for consistency. If any doubt remains, the run is discarded.

The data is collected into two hand maintained databases: a tab delimited text file called `master_list.txt` in which runs are assigned membership in kinematically homogeneous groups which can be analyzed together, and the Replay kinematics file (see Section 3.1.3).

¹These are not scripting languages, but they do induce considerable decision making in the program.

Post-processing of the Replay output (in the form of the `gen<run#>.txt` files produces a file called `CT_summery.txt` [*sic*] which provides valuable guidance in assembling the master list.

B.2 Tools

The number of distinct tools is harder to nail down. The actual work described in Chapter 5 is accomplished by two Fortran codes (one to extract and deradiate the spectral functions, and one to multiple kinematics, and extract transparencies), but at least three utility shell scripts are available to help with the copious bookkeeping, and two of these are simply friendly front ends to powerful awk scripts which parse the master list file to collect information. Further, some utility scripts developed for the on-line monitoring of the experiment have been retained to aid in sorting and grouping the data runs. One of the bookkeeping scripts provides a postscript output file for manual sanity checking, and two kumacs are available to check the results of the Fortran based-analysis.

B.2.1 Doing the Work

The actual work of extracting, deradiating, and combining the spectral functions is accomplished by two closely related Fortran programs: `GUDRad` and `GUSP`² They share a considerable library of routines for bin-wise manipulation of two dimensional arrays of data with associated error estimates, and for converting that data to and from `HBOOK` storage formats.³

²The names are derived from “Grand Unified Deradiation” and “Grand Unified Sum-Project” respectively. The Grand Unified appellation arises because these are the results of scrapping a confused mishmash of `KUIP`, `shell`, `awk`, and `COMIS` code that grew piece-wise during early testing, and replacing it with a consistent, unified approach.

³`HBOOK` stores and manipulates two dimensional histograms (and particularly their error estimates) in a way that is inconsistent with our analysis needs, but we still wanted to be able to take advantage of `PAW`’s plotting capabilities.

GUDRad writes an HBOOK file containing the various bin-wise yield and spectral function results. GUSP writes two files. The first is an HBOOK file containing the properly summed (deradiated) spectral functions for the data, and the radiation-off Monte Carlo run (and possibly a crude estimate of the theory file values), and projections in both directions of these results. The other is a plain text file containing information about the integrated yields and spectral strength of the real data and the Monte Carlo runs.

B.2.2 Bookkeeping and Consistency

A central feature of the analysis methodology is the group (or “chain”⁴) assignments maintained in the master list. Many runs—especially at high Q^2 —have very few physics events, making them difficult to work with because there is no statistically meaningful structure to the data. So many runs at (nearly) identical kinematics are treated together. The master list file exists to map run number onto the group(s) they belong to. Chains are named by their target (c, d, h, fe, fex, and dummy for carbon, deuterium, hydrogen, the two iron targets, and the dummy respectively), their Q^2 (3, 6, or 8), and an arbitrary sting (in practice “good” followed by a number to differentiate different running periods).

Some of the more important tools for handling the bookkeeping and keeping the analysis internally consistent are:

`mkfiles.sh` A front end for `chain_inp.gawk`.

`chain_inp.gawk` An awk script which parses the master list, and for each qualifying run parses the scaler file generated by Replay to build up a picture

⁴From the PAW structure for combining several ntuples together. Early versions of the analysis software ran in KUIP and COMIS, and used this feature.

of the kinematics, and total charge on target associated with that chain. If the kinematics are sufficiently consistent, it then writes the SIMC input files needed to generated the radiation on and off runs matching that chain.

mkgudr.sh A front end for **chain_gudr.gawk**. Before invoking the awk script, it runs **apoffset.kumac** to find the missing energy offset needed to get consistent deradiation.

chain_gudr.gawk Works similarly to **chain_inp.gawk**, but also reads the SIMC history files, and if everything (the chain kinematics, and the SIMC kinematics) is consistent, writes an input file for **GUDRad** taking into account real and simulated charge, yield correction, and dummy subtraction.

apoffset.kumac Attempts to fit a heuristic function to E_m spectrum of the data and Monte Carlo results and deduce any missing energy offset between the two. Writes a postscript file summarizing the results for consistency checking.

mkgusp.sh Writes an input file for **GUSP**.

None of this code is separately documented, but is it all well commented, and the shell scripts have non-trivial usage messages built-in.

B.2.3 Procedure

An outline of the actual analysis procedure:

1. Check the **master_list.txt** file. We want to have a consistent description text, on good data files. Use the Hall C log and the info in the **CT_summery.txt** [*sic*] to find how to group the runs.

2. (a) Run `mkfiles.sh` on the chain descriptors. If it barfs on angles, energies, etc. check the log, summary files, and kinematics files. You may need to break the group into pieces, or reanalyze some runs with the correct kinematics settings. In marginal cases, you can use the `-t` flag to set tolerances higher than the default, but this is not recommended.
- (b) Run `simc` on (all) the `rad` and `norad` input files produced in step 2a.
3. (a) Run `mkgudr.sh` on the chain/SIMC-output pair(s). This should work unless you increased the tolerances in step 2a, in which case this may be necessary again. You should use the auto-em-offset option of the script⁵ by default. Check the `*_em_offset.ps` files to see that a reasonable fit was obtained before proceeding. In some cases, it may be necessary to set the em-offset by hand.
- (b) Run `GUdRad` on the `.gudr` file(s). Try the `check_gudr.kumac` to look for unexpected behavior.
4. (a) Whether or not you are doing multiple kinematics settings at one Q^2 , use `mkgusp.sh` to write a `.gusp` file to pull together and project the data, extract the transparency, etc.
- (b) Run `GUSP` on the `.gusp` file. Try the `check_gusp.kumac` to get output, and look for problems.
- (c) If the low E_m edge of the spectral function extends too far, it is possible that you need to break the chains into finer groups. Return to step 1 using the existing `simc` output and `apoffset.kumac` to help you find the breaks.

⁵A slow process as it performs a 5 or more parameter fit to the E_m spectrum of the ntuple...

- (d) GUSP also writes a series of `.tran` files, summarizing the results of the spectral function extraction, and transparency measurements.
- (e) The code already corrects for proton absorption, cryo-target density dependence, tracking efficiency, trigger efficiency, dead times, trigger prescales, and the MC spectroscopic-factor/correlation-correction. Apply by hand any other corrections you need to make.

B.3 Tests

The most fundamental—but least reliable—test of a tool chain is “Does it give reasonable results?” The answer in this case seems to be a qualified yes. We are able to partially reproduce the transparency number generated by Ken Garrow, and the spectral functions obtained have roughly the same shape as those reported in the literature. Further, as shown in Fig. B.1, extracting the spectral function from radiation disabled Monte Carlo data generates a shape similar to that found by parsing the theory file directly, and deradiating the spectral function extracted from a radiation enabled run generates results virtually identical to the raw spectral function derived from the radiation disabled run.

Ideally, all of the software would be accompanied by an exhaustive test suite intended to prove its consistency. In fact, test code has been written only when the documentation for the supporting libraries seemed unclear or contradictory, or when obvious problems arose.

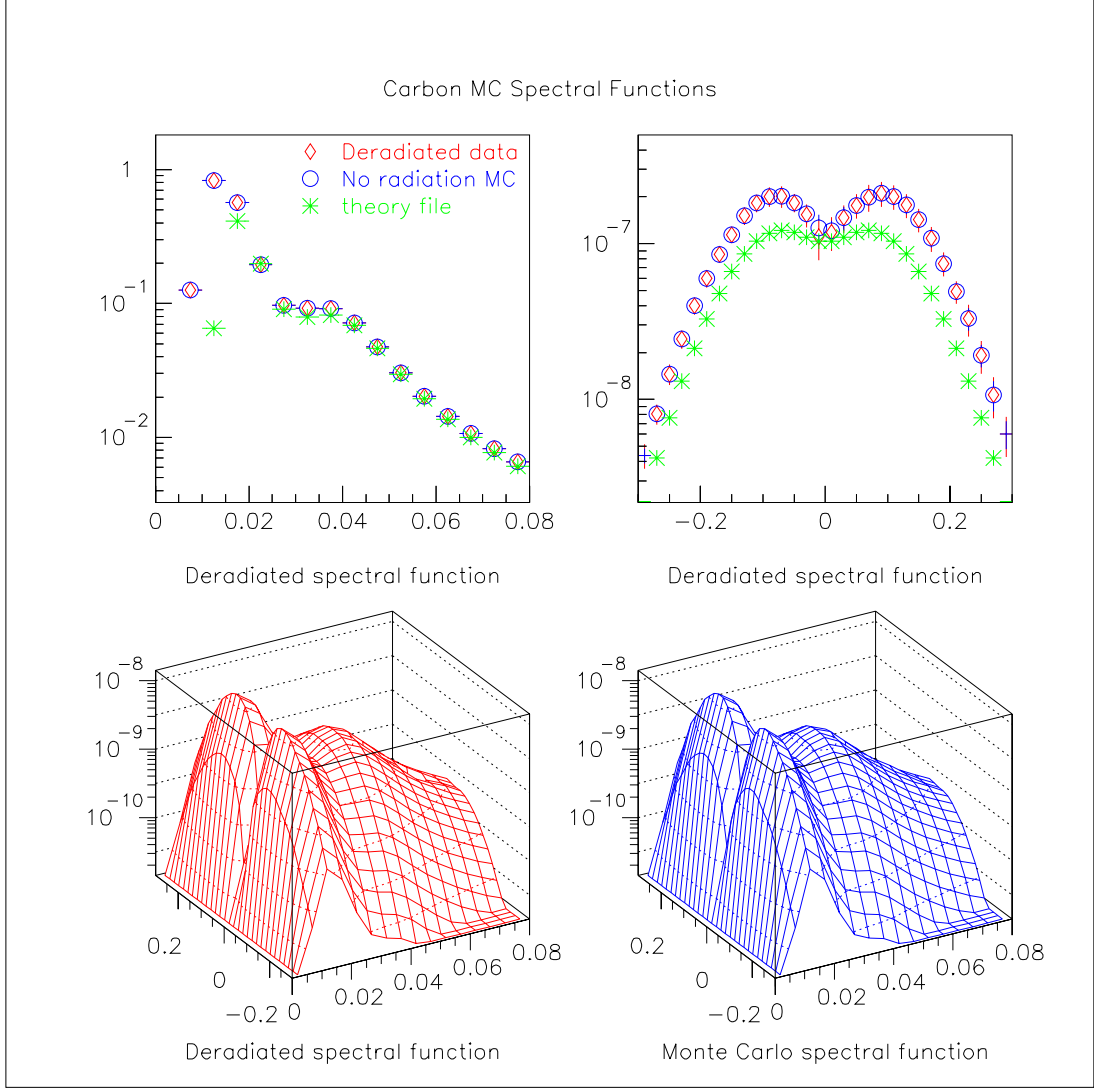


FIG. B.1: A comparison of the deradiated spectral function arising from Monte Carlo output with radiation enabled, with the (raw) spectral function extracted from Monte Carlo output with radiation disabled. Also shown is a crude integration of the spectral function as expressed in the theory file. Both Monte Carlo runs simulated our carbon data at $Q^2 = 3.3 \text{ GeV}^2$, with a HMS angle of 24.8 degrees.

BIBLIOGRAPHY

- [1] R. Ent, N. Makins, R. Milner, et al. Measurment of the Nuclear Dependence and Momentum Transfer Dependence of Quasielastic ($e, e'p$) Scattering at Large Momentum Transfer. CEBAF Proposal, 1991.
- [2] J. F. J. van den Brand, H. J. Bulten, et al. Measurment of the Nuclear Dependence and Momentum Transfer Dependence of Quasielastic ($e, e'p$) Scattering at Large Momentum Transfer. CEBAF Proposal update and extention, 1994.
- [3] Dipangkar Dutta. *The ($e, e'p$) Reaction Mechanism in the Quasi-Elastic Region*. PhD thesis, Northwestern University, Evanston, Illinois, 1999. JLAB e91-013.
- [4] Derek van Westrum. *Qausielastic ($e, e'p$) Reactions and Proton Propagation Through Nuclei*. PhD thesis, University of Colorado, 1998. JLAB e91-013.
- [5] A. H. Mueller. . In *Proceedings of the Seventeenth Recontre de Moriond Conference on Elementary Particle Physics*, 1982.
- [6] S. J. Brodsky. . In *Proceedings of the Thirteenth International Symposium on Multiparticle Dynamics*, 1982.
- [7] John Dirk Walecka. *Theoretical Nuclear and Subnuclear Physics*. Oxford University Press, 1995.
- [8] R. J. Glauber. High-energy collision theory. In W. E. Brittin and D.G. Dunhan, editors, *Lectures in Theoretical Physics*. Interscience, 1959.
- [9] Henk P. Blok. Electron scattering. Lecture at HUGS, May 1988.
- [10] D. Mack, 2000. Private communication.
- [11] N. N. Nikoleav. Colour transparency: a novel test of qcd in nuclear interactions. *Surveys High Energ. Phys.*, 7:1, 1994.

- [12] O. Benhar et al. Color transparency and correlation effects in quasielastic electron-nucleus scattering at high momentum transfer. *Phys. Rev. Lett.*, 69:881, 1992.
- [13] Jochen Volmer. *The Pion Charge Form Factor via Pion Electroproduction on the Proton*. PhD thesis, Vrije Universiteit te Amsterdam, Coesfeld, Duitsland, 2000. JLAB e93-021.
- [14] Naomi C. R. Makins. *Measurement of the Nuclear Dependence and Momentum Transfer Dependence of Quasielastic $(e, e'p)$ Scattering at Large Momentum Transfer*. PhD thesis, Massachusetts Institute of Technology, 1994. SLAC NE18.
- [15] Thomas G. O'Neill. *Search for Color Transparency in $A(e, e'p)$ at High Momentum Transfer*. PhD thesis, California Institute of Technology, 1994. SLAC NE18.
- [16] N.C.R. Makins et al. *Phys. Rev. Lett.*, 722:1986, 1994.
- [17] L. L. Frankfurt, M. I. Strikman, and M. B. Zhalov. Sum rule description of color transparency. *Phys. Rev.*, C46:2547, 1992.
- [18] J. Nemchik, N. N. Nikolaev, and B. G. Zakharov. Color transparency after the NE18 and E665 experiments: Outlook and perspectives at CEBAF. arXiv:nucl-th/94060005 v1, June 1994. LANL Preprint.
- [19] L. L. Frankfurt, M. I. Strikman, and M. B. Zhalov. Color transparency effects for hole excitations in $a(e, e'p)$ reactions. *Nucl. Phys.*, A515:599, 1990.
- [20] Salvatore Frullani and Jean Mourgey. Single-particle properties of nuclei through $(e, e'p)$ reactions. *Adv. Nucl. Phys.*, 14:1–285, 1984.
- [21] L. Lapikas, G. van der Steenhoven, et al. Transparency of ^{12}C for protons. *Phys. Rev. C*, 61, 2000.
- [22] A.S. Carroll et al. Nuclear transparency to large-angle pp elastic scattering. *Phys. Rev. Lett.*, 61:1698, 1988.
- [23] T. G. O'Neill et al. A -dependence of nuclear transparency in quasielastic $A(e, e'p)$ at high Q^2 . *Phys. Lett.*, B351:87, 1995.
- [24] M. R. Adams et al. Measurement of nuclear transparencies from exclusive ρ^0 meson production in muon-nucleus scattering at 470 gev. *Phys. Rev. Lett.*, 75:1525–1529, 1995.

- [25] D. Abbott et al. Quasifree $(e, e'p)$ reactions and proton propagation in nuclei. *Phys. Rev. Lett.*, 80:5072, 1998.
- [26] Hermes Collaboration. Observation of a coherence length effect in exclusive ρ^0 electroproduction. *Phys. Rev. Lett.*, 82:3025, 1999.
- [27] G. Garino et al. Proton propagation in nuclei studied in the $(e, e'p)$ reaction. *Phys. Rev. C*, 45:780, 1992.
- [28] E. M. Aitala, S. Amato, et al. Observation of color-transparency in diffractive dissociation of pions. *Phys. Rev. Lett.*, 86:4773–4777, 2001.
- [29] N. N. Nikoleav et al. Theoretical interpretation of the NE18 experiment on nuclear transparency in $a(e, e'p)$ scattering. *Phys. Rev. C*, 50:R1296, 1994.
- [30] L. L. Frankfurt et al. In N. Isgur and P. Stoler, editors, *Workshop on 'CEBAF at Higher Energies'*, page 499, 1994.
- [31] T. de Forest Jr. Nucleon emission in electron scattering. *Annals of Phys.*, 45:365–403, 1967.
- [32] Peter Bosted. Empirical fit to the nucleon electromagnetic form factors. *Phys. Rev. C*, 51:409, 1995.
- [33] S. Boffi, C. Giusti, and F. D. Pacati. Structure function in nucleon emission by polarized electrons. *Nucl. Phys.*, A435:697, 1985.
- [34] T. de Forest Jr. Off-shell electron-nucleon cross sections. *Nucl. Phys.*, A392:232, 1983.
- [35] S. Pollock, H. W. L. Naus, and J. H. Koch. Electron-nucleon cross section in $(e, e'p)$ reactions. *Phys. Rev. C*, 53:2304, 1996.
- [36] N. N. Nikoleav, J. Speth, and B. G. Zakharov. Glauber theory of final-state interaction in $(e, e'p)$ scattering. *J.Exp.Theor.Phys.*, 82:1046–1065, 1996.
- [37] O. Benhar, S. Fantoni, N. N. Nikolaev, and other. On the missing momentum dependence of the color transparency effects in $(e, e'p)$ scattering. 2001.
- [38] Gefforey Krafft. How the linac beam position monitors “work”. CEBAF TN-93-004, 1993.
- [39] Paul Gueye. Status of the actual Beam Position Monitors in the Hall C Beamline. Hall C Documentation, 1995.

- [40] C. Yan et. al. Superharp—A wire scanner with absolute position readout for beam energy measurement at CEBAF. *Nucl. Instrum. Meth. A*, 365:261–267, 1995.
- [41] Chris Armstrong. Beam Current Measurement in Hall C. Hall C Documentation, 1996.
- [42] Dave Mack. Current Monitoring in Hall C. Hall C Documentation, 1997.
- [43] John Arrington. *Inclusive Electron Scattering From Nuclei at $X > 1$ and High Q^2* . PhD thesis, California Institute of Technology, Pasadena, California, 1998. JLAB e89-008.
- [44] Dave Mack. BCM temperature cycling negligible. Hall C Electronic Logbook Entry #14212, 1999.
http://hallcweb.jlab.org/hclog/9907_archive/990713123253.html.
- [45] David J. Gaskell. *Logitudinal Electroproduction of Charged Pions from Hydrogen, Deuterium, and Helium-3*. PhD thesis, Oregon State University, 2001. JLAB e91-003.
- [46] Jochen Volmer. The HMS quadrupoles in the HMS-100 tune. Hall C Documentation, 1997.
- [47] W. J. Cummings. SOS Handbook. Hall C Documentation.
- [48] Christopher S. Armstrong. *Electroproduction of the $S_{11}(1535)$ Resonance at High Momentum Transfer*. PhD thesis, The College of William & Mary in Virginia, 1998. JLAB e94-014.
- [49] trigger_jan99.ps. Hall C documentation, July 1999. CUE filesystem
[//u/group/hallc/documents/trigger/diagrams/trigger_jan99.ps](#).
- [50] Stephen A. Wood. Running data aquisition. Hall C Documentation, April 1997.
- [51] ts_jan99.ps. Hall C documentation, July 1999. CUE filesystem
[//u/group/hallc/documents/trigger/diagrams/ts_jan99.ps](#).
- [52] CEBAF. *CODA CEBAF On-line Data Aquisition User's Manual*, 1.4 edition, January 1995. CEBAF Documentation.
- [53] Stephan A. Lewis. Overview of the experimental physics and industrial control system: EPICS. Technical report, Lawrence Berkeley National Laboratory, 2000.

- [54] CERN, CERN Geneva, Switzerland. *PAW Physics Analysis Workstation An Introductory Tutorial*.
- [55] CERN, CERN Geneva, Switzerland. *HBOOK Refence Manual*, 4.24 edition.
- [56] D. F. Geesaman and Steve Wood. Hall C Anlysis Software vade mecum. Hall C Documentation (version 1.3), 1994.
- [57] Steven A. Wood. *The CEBAF Test Package: A Symbolic and Dynamic Test, Histogram and Parameter Package for On- and Off-line Particle Physics Data Analysis*. Physics Division, CEBAF, January 1995.
- [58] Ken Garrow. Private communication, 2000.
- [59] Henk Blok. Private communication, 1999.
- [60] Jochen Volmer and Henk Block. Usage of heapcheck. Hall C Documentation, March 1999.
- [61] Derek van Westrum. Measurement of Tracking Errors in the Regular and “4 of 6” Tracking Algorithms. Hall C Documentation, November 1996.
- [62] Dave Gaskell. Tracking Efficiencies in the SOS for E91003. Hall C Doumentation, 1998 June.
- [63] John Arrington. (long) note on tracking efficiency. Hall C Ellectronic Logbook Entry #17026, 1999.
http://hallcweb.jlab.org/hclog/9907_archive/990831120948.html.
- [64] W. R. Leo. *Techniques for Nuclear and Particle Physics Experiments*. Springer-Verlag, 1994.
- [65] Maria Ioana Niculescu. *Inclusive Resonance Electroproduction Data From Hydrogen and Deuterium and Studies of Quark-Hadron Duality*. PhD thesis, Hampton University, May 1999.
- [66] Derek van Westrum. Measurement and Estimation of Proton Absorbtion in the Hall C Spectrometers. Hall C Documentation, 1997.
- [67] Particle Data Group. *Particle Phyics Data Book*. 1999.
- [68] Dipangkar Dutta. Radiative Corrections—The SIMC Way. Hall C Documentation.
- [69] John Arrington. A-B-SIMC. Hall C Documentation.

- [70] K. Holinde and R. Machleidt. Obep and eikonal form factor. *Nuc. Phys. A*, page 479, 1976.
- [71] L. Lapikás. Quasi-elastic electron scattering off nuclei. *Nuc. Phys. A*, 553:297, 1993.
- [72] R. Ent, B. W. Filippone, N. C. R. Makns, R. G. Millner, T. G. O'Neill, and D. A. Wasson. Radiative corrections for $(e, e'p)$ reactions at gev energies. *Phys. Rev. C*, 64:054610, 2001.
- [73] Luke W. Mo and Yung-Su Tsai. Radiative corrections to elastic and inelastic e p and mu p scattering. *Rev. Mod. Phys.*, 41:205–235, 1969.
- [74] D. R. Yennie, S. C. Frautschi, and H. Suura. The infrared divergence phenomena and high-energy processes. *Ann. Phys.*, 13:379–452, 1961.
- [75] Richard A. Early. Numerical solution of the electron diffusion equation. *Nucl. Instrum. Meth.*, 109:93–100, 1973.
- [76] William R. Gibbs. *Computation in Modern Physics*. World Scientific, 1994.
- [77] Yanhe Jin, H.P. Blok, and L. Lapikás. $e - p$ off-shell cross section in quasielastic $(e, e'p)$ reactions. *Phys. Rev. C*, 48:R964, 1993.
- [78] Ken Garrow, David McKee, et al. Nuclear transparency from quasielastic $a(e, e'p)$ reactions up to $q^2 = 8.1$ (gev/c)². *Phys. Rev. C*, 2002.
- [79] P. Jain and J.P. Ralston. Systematic analysis method for color transparency experiments. *Phys. Rev. D*, 48:1104, 1993.
- [80] H. Gao, V.R. Pandharipande, S. C. Pieper, et al. Nuclear transparency to intermediate-energy nucleons from $(e, e'p)$ reactions. *Phys. Rev. C*, 45:791, 1992.
- [81] L. L. Frankfurt, M. I. Strikman, and M. B. Zhalov. Pitfalls in looking for color transparency at intermediate energies. *Phys. Rev.*, C50:2189, 1994.
- [82] P. Jain and J.P. Ralston. Perturbative color transparency in electroproduction experiments. *Phys. Rev. D*, 62:113009, 2000.
- [83] B. K. Jennings and G. A. Miller. Energy dependence of color transparency. *Phys. Rev. D*, 44:692, 1991.
- [84] Glennys R. Farrar, Huan Liu, Leonid L. Frankfurt, and Mark I. Strikman. Transparency in nuclear quasiexclusive processes with large momentum transfer. *Phys. Rev. Lett.*, 61(6):686, August 1988.

- [85] The science driving the 12 GeV upgrade of CEBAF. Whitepaper, January 2001.
- [86] Dave J. Mack and J. Volmer. Solid Target Measurement for Hall C, Spring 1997. Hall C Documentation, 1997.
- [87] Particle Data Group. *Particle Physics Booklet*. Springer, 1998.

INDEX

- absorption
 - proton, **72**, 72–86
- background
 - proton absorption, 76
- BCM, *see* beam current monitor
- beam current monitor, 33
- beam position monitor, 32
- Born approximation, 9, 19
- BPM, *see* beam position monitor
- CEBAF Test Package, *see* CTP
- coordinate system, 58
- correlation correction, 104
- Coulomb correction, 9, **102**
- cross-section
 - off-shell, 22, 102
- CTP, 61, 89
- DAQ, *see* data acquisition
- data acquisition, **56**, 48–56
- dead time, **67**, 74
- deradiation, **118**, 116–122
- distorted wave impulse
 - approximation, *see* DWIA
- DWIA, 9, 22–25
- energy loss, 60, 104, 116
- Glauber approximation, 9, 26–28
- high momentum spectrometer, *see* HMS
- HMS, 10, **41**
- independent particle shell model, 90
- interaction
 - final state, 2
 - final state, 7, 9, 20
 - initial state, 2, 20
- IPSM, *see* independent particle shell model
- kinematics file, **61**
- luminosity scan, **71**
- missing energy, 13
- missing momentum, 13
- Monte Carlo, *see* SIMC
- multiple scattering, 116
- multiple scattering, 64, 72, 82, 104
- one photon exchange, 110
- OPE, *see* one photon exchange
- optical potential, 90
- particle identification, 70
- PID, *see* particle identification
- plane wave impulse approximation,
 - see* PWIA
- prescale, **55**, 74
 - pions, 55
- proper time, 6
- PWIA, 9, 19–22, 93
- radiative corrections, 88
- radiative corrections, 93–101
- raster
 - fast, 34
- reaction plane, 13
- Replay, 11, **57**
- scattering plane, 11

short orbit spectrometer, *see* SOS

SIMC, 11, **87**, 87–105

SOS, 10, **46**

spectral function, 22, **22**, 89

 distorted, 25

 effective, 25

 extraction of, 114

 model, 90–92

spectroscopic factor, 92

superharp, 33

theory file, 89, 92–93

transparency

 color, 4, 15–16

 extraction of, 106

 nuclear, 7, **15**, 14–15